LIQUID METAL BASED HIGH TEMPERATURE

CONCENTRATED SOLAR POWER: COST CONSIDERATIONS

A Thesis
Presented to
The Academic Faculty

by

Gregory Casimir Wilk

In Partial Fulfillment
of the Requirements for the Degree
Master of Science Mechanical Engineering from the
George W. Woodruff School of Mechanical Engineering

Georgia Institute of Technology
May 2016

LIQUID METAL BASED HIGH TEMPERATURE

CONCENTRATED SOLAR POWER: COST CONSIDERATIONS

Approved by:

Dr. Asegun Henry, Advisor
School of Mechanical Engineering
Georgia Institute of Technology

Dr. Shannon Yee
School of Materials Science and Engineering
Georgia Institute of Technology

Dr. Samuel Graham
School of Mechanical Engineering
Georgia Institute of Technology

Date Approved: 11/12/15

ACKNOWLEDGEMENTS

I thank my mother and father for their continued support throughout my college education. Their example of strong work ethic gave me the confidence to complete this thesis. Secondly, I want to thank my advisor, Dr. Asegun Henry, for all that he's done in this process. His mentorship regarding heat transfer analysis allowed me to complete this power plant model. Further, his diligent editing improved my writing skills and led to a professional product.

I would also like to thank other faculty at Georgia Tech who contributed to my thesis work. Dr. Diane England taught me how to construct molten metal experimental loops and the refractory materials available for experimentation and design. Dr. Sandhage and Dr. Yunshu performed many material tests and analyses that supported the final design. Dr. Yee provided valuable comments and advice that helped develop the economic analysis and guide my defense.

I want to thank my colleague and good friend Freddy DeAngelis for extensively editing my thesis. His help with COMSOL modeling and heat transfer analysis helped complete this work. Also, I thank all my friends I have made in graduate school for making the last two years a fantastic experience.

Finally, I would like to thank the ARPA-E agency for the financial support of project DE-AR0000339, through which this work was made possible.

TABLE OF CONTENTS

ACKNOWLEDGEMENTS III

LIST OF FIGURES IX

GLOSSARY (SYMBOLS OR ABBREVIATIONS) XIII

SUMMARY XIX

CHAPTER 1: INTRODUCTION 1

Plant Configuration 3

Concentrated Solar Power History 4

LM-CSP Experimental Set-up 10

CHAPTER 2: TECHNO-ECONOMIC ANALYSIS METHODOLOGY 13

CSP Plant Levelized Cost of Electricity 13

Cost Estimation Methodology 14

LS- CSP Plant Configuration 16

LM-CSP Plant Configuration 18

Overall Capital Costs 20

Cost Report Structure 22

CHAPTER 3: SOLAR ENERGY COLLECTION 23

Section Overview 23

Heliostat Field Discussion 24

CHAPTER 4: SOLAR RECEIVER 26

Section Overview 26

Tower 27

Receiver 30

Internal Receiver Design 32
Secondary Concentrators 36
Receiver Insulation 38
Receiver Nitrogen Containment 40
Receiver Construction Costs 42
Receiver Total Costs 43
Receiver Pressure Losses 43
CHAPTER 5: THERMAL ENERGY STORAGE (TES) 47
Section Overview 47
Thermal Storage Fluid 48
2-Phase Energy Storage 51
TES Tanks 53
TES Pipes/Support Pumps 60
Nitrogen Containment Steel Conduit 61
Conclusion 62
CHAPTER 6: HEAT EXCHANGERS 63
Shell and Tube Heat Exchanger Design 66
Shell and Tube Heat Exchanger Results 72
Shell and Tube Heat Exchanger Conclusions 73
Liquid Droplet Heat Exchanger (LDHX) 75
LDHX Heat Transfer Analysis 76
LDHX Parasitic Losses 82
LDHX Results 83

CHAPTER 7: POWER CYCLE.....85

Power Cycle Heat Exchangers.....87

LM pump 88

Parasitic losses 89

Major Pumping Losses 90

CHAPTER 8: TEA CONCLUSION 93

TEA Conclusion 97

CHAPTER 9: LM RECEIVER LOOP EXPERIMENTAL DESIGN.....100

Pipe Materials for Sn(l).....105

Pipe Connections 111

Reaction Bonds.....112

Mechanical Sealing.....123

LM Valves 125

Graphite 90° Elbow Minor Losses 131

CHAPTER 10: CONCLUSION.....139

REFERENCES.....143

LIST OF TABLES

Table 1: LCOE for plants entering service 2020 [1] 2

Table 2: LS-CSP plant capital costs (2011) 22

Table 3: Receiver subsystem cost comparison 27

Table 4: 540 MW_t internal optical cavity receiver graphite costs 36

Table 5: Receiver component costs 43

Table 6: Receiver pressure losses 44

Table 7: Sn(l) vs. salt(l) transport properties [43, 44] 45

Table 8: Thermal energy subsystem 48

Table 9: Thermal storage fluid cost comparison 50

Table 10: Al-Si melt storage phases 53

Table 11: Castable cement samples in Al-Si melt 55

Table 12: Westmoreland ALII castable cement properties 56

Table 13: Heat exchanger power and fluids 66

Table 14: Shell and tube heat EX configuration variables for Kern Method 69

Table 15: Shell and tube heat exchanger material properties[47, 79] 72

Table 16: Thermal results for heat exchanger 73

Table 17: Shell and tube heat exchanger pipe cost 73

Table 18: LDHX Results 83

Table 19: LDHX Costs 84

Table 20: Power block cost comparison 89

Table 21: Major head loss 91

Table 22: Parasitic loss and plant output 92

Table 23: Overnight capital cost plant comparison 94

Table 24: LCOE comparison of different energy sources 97

Table 25: Technical challenges with LM-CSP 101

Table 26: Weight loss measurements of graphite tubes in Sn(l) 108

Table 27: Part identifier 127

Table 28: K values for drain trials 136

LIST OF FIGURES

Fig. 1: LS-CSP plant schematic 4

Fig. 2: SEGS parabolic trough plant (NOAA) 5

Fig. 3: Decline of PV prices. Ivanpah price plotted in red 7

Fig. 4: Crescent dunes LS-CSP plant (Solar Reserve) 8

Fig. 5: Schematic of graphite receiver test loop. 11

Fig. 6: Receiver inlet contained within inert containment box 11

Fig. 7: LS-CSP plant 17

Fig. 8: LM-CSP plant configuration 18

Fig. 9: An example tower constructed for the Crescent Dunes CSP plant in Nevada 28

Fig. 10: LCOE vs. number of pipes 29

Fig. 11: External receiver 31

Fig. 12: Cross section of cavity receiver. Focused incoming sunlight is represented by the yellow triangle. Re-radiating light is the red arrows. Aperture insulation is tan. The graphite receiver is gray. 32

Fig. 13: Internal receiver with nitrogen containment 33

Fig. 14: Top-down view of the solar receiver showing cavity receiver locations. The large black circle represents the receiver perimeter, while the red dots represent all 16 cavity receivers through which Sn flowed while traveling along a single path. The Sn pipe path started at the center of the receiver base, flowed vertically (out of page) to appropriate height, flowed around a full perimeter of the receiver, then flowed back to the center of the receiver. 34

Fig. 15: (Left Side) Monolithic small scale receiver module. (Right Side) CAD drawing of a full scale cavity pipe receiver module. Light is emitted into the receiver at the top of the Fig. 35

Fig. 16: Secondary concentrator 37

Fig. 17: Top down review of receiver insulating ring. In reality, the insulation in front of the receiver modules would have been cut out to let light through. For cost modeling, the insulation was modeled as a cylindrical shell with the dimensions shown and 18 meters tall 39

Fig. 18: Thermal storage fluids under research are plotted over the proposed temperature range at which they would be used. Fluids are organized vertically from least expensive to most expensive. Example power cycles and their efficiencies are shown as a vertical line for the cycle peak temperature input as a reference [43, 50, 70, 71] 49

Fig. 19: Al-Si phase diagram. The alloy chosen for TES is shown as the vertical red line, 30 atom % Si. Latent heat storage occured in the temperature range 577°C to 822°C [73] 52

Fig. 20: Al-Si(l) storage tank options 54

Fig. 21: Castable cement cup cross sections exposed to Al(l) at 1200°C for 120 hours. Left is WAM ALII, right is standard castable cement, WAM 45 SC. The ALII with <0.4% silica experienced no degradation. The 45 SC with 48% silica was penetrated. [75] 56

Fig. 22: Tank cross sections with different wall thickness. Top row is tank without cracks. Bottom row is if the wall cracks and 0.25% of wall volume is penetrated by Al(l). 60

Fig. 23: Steel conduit nitrogen containment 62

Fig. 24: Heat exchanger diagram for charging TES tanks 64

Fig. 25: Heat exchanger diagram for dis-charging TES tanks 65

Fig. 26: Cross sectional front and side view of shell and tube heat exchanger. 69

Fig. 27: Heat Exchanger Pipe 71

Fig. 28: LDHX configuration 75

Fig. 29: Hole effective area 82

Fig. 30: Power Cycle Diagram 86

Fig. 31: Sn flow parasitic loss 90

Fig. 32: Experimental laboratory graphite internal receiver. Keyboard in background for size reference. 102

Fig. 33: Solar simulator 103

Fig. 34: Solar receiver experimental loop 104

Fig. 35: LM receiver test loop inside steel nitrogen containment 105

Fig. 36: Two originally identical stainless steel gears. The right gear was corroded by Sn(l) after < 24 hrs of operation. One steel gear was treated with a ceramic coating, while the other was not, which led to a major difference in corrosion. 106

Fig. 37: Graphite pipes used in experimental loops. Pipe on the right had OD: 0.5" and ID: 0.3125". Pipe on the left had OD: 0.875" and ID: 0.5" 107

Fig. 38: SE images of the epoxy-graphite interface at the bottom of the one-end-closed graphite tube 109

Fig. 39: Sn filled section of glass-lined stainless steel tubing 110

Fig. 40: TiN coated stainless steel fittings. Left most elbow was uncoated. 111

Fig. 41: Aremco Ceramabond 669 112

Fig. 42: Cotronics 931 graphite cement. 2 component mixture consisted of binder and powder 113

Fig. 43: Cotronics 931 cement. Left picture is unmixed, right picture is thoroughly mixed. 114

Fig. 44: Graphite cement application 115

Fig. 45: Graphite 2 component cement bond. Excess cement squeezed from joint is smoothed into a beveled surface 116

Fig. 46: Sn plug is inserted into tube. Cement is then applied on outer surface and the part to which the tube is being cemented. The tube is then inserted in to be cured. 117

Fig. 47: Cement face joint leaking water. The CAD model for the part shown on the left is shown on the right for reference. 119

Fig. 48: Pick and cement procedure for leaking part. 120

Fig. 49: Example of more reliable geometry for forming a successful cement bond 121

Fig. 50: Example of a cemented joint that is inaccessible to repacking. The CAD representation of the two cemented geometries is shown in the bottom image 122

Fig. 51: Graphite ferrule joint 124

Fig. 52: All graphite compression joint. Picture on left shows completed graphite union joint above completed stainless steel joint for size comparison. The picture on the right shows the coarse threads in a graphite union joint. 125

Fig. 53: Fujikin ball valve assembly exploded view 126

Fig. 54: Graphite rope packing that replaced PTFE and teflon seals 128

Fig. 55: Valve and actuator holder 129

Fig. 56: Top down view of ball valve. Graphite sheet was placed between alumina ball and housing to stem tin flow 129

Fig. 57: Graphite plug valve. Image on the right is a cross section view. 130

Fig. 58: Graphite elbow cross section 132

Fig. 59: Elbow minor loss experiment 132

Fig. 60: Sn elbow minor loss test pour procedure 134

Fig. 61: Elbow drain curve data 135

GLOSSARY (SYMBOLS OR ABBREVIATIONS)

A	Cost of Solar Energy Collection ($)
	Area (m^2)
B	Cost of Solar Receiver ($/$kW_t$)
Bi	Biot Number
C	Cost of Thermal Storage ($/$kWh_t$)
	Concentration Ratio
C_D	Drag Coefficient
C_t	Tower Cost ($)
	Heat Capacity Rate (W/K)
	Fluid Storage Cost ($/$kWh_t$)
C_p	Heat Capacity (J/kg-K)
C_r	Heat Capacity Rate Ratio
C_h	Column Height (m)
D	Diameter (m)
D_e	Effective Flow Diameter (m)
	Cost of Power Cycle ($/kW)
E	Plant Electrical Output (kW)
	Total Energy Stored (Joules)
E_D	Energy per Drop (Joules)
I_t	Investment Expenditures in Year t ($)
M_t	Operations and Maintenance in Year t ($)
F_t	Fuel Expenditure in Year t ($)
F	Solar Multiple

	Fixed Tower Cost ($)
f	Friction Factor
G_s	Mass Flow Rate per Area (kg/m^2-s)
E_t	Electricity Generation in Year t (kWh$_e$)
L	length (m)
r	Discount Rate
	radius (m)
n	Life of the System (years)
v	flow speed (m/s)
K	Direct Equipment Costs ($)
	Minor Pressure Loss Coefficient
K_1	Contingency Costs ($)
K_2	Indirect Costs ($)
K_{tot}	Total Overnight Installed Costs ($)
K_F	Total Cost of Heliostat Field ($/kW)
K_F	Total Cost of Heliostat Field ($/kW)
K_s	Thermal Energy Storage Capital Cost ($/kW$_e$)
L_B	Baffle Spacing (m)
L_s	Pipe/shell length (m)
g	Gravitational Constant (=9.81 m/s^2 at sea level at the equator)
h	Convective Heat Transfer Coefficient (W/m^2-K) height (m)
	Pressure Head Loss (m)
h_f	Latent Heat of Fusion (J/kg)
k	Thermal Conductivity (W/m-K)
M	Number of Receiver Modules

	Material Cost ($/kg)
	Mass of Storage Medium (kg)
m	Mass (kg)
$\dot{m}$	Mass Flow rate (kg/s)
NTU	Number of Transfer Units
Nu	Nusselt Number
N_B	Number of Baffles
U	Conductance (W/m^2K)
P	Packing Factor
P	Pressure (Pa)
P_t	Tube Pitch (mm)
P_H	Energy Rate per Hole (W)
Q	Heat Rate (W)
Q_D	Energy Rate Per Drop (Watts)
q_r	Heat loss through cylindrical wall (W)
q''	Heat Flux (W/m^2)
q''_{rad}	Radiative Heat Flux (W/m^2)
	Radius (m)
R_c	Receiver Nitrogen Containment Cost ($)
Re	Reynold's Number
S_s	Cross Flow Shell Area (m^2)
T	Temperature (K or °C)
t	Time (s)
t_b	Baffle Thickness (mm)

T_c	Cold Temperature (°C)
t_D	Time Between Drops (s)
T_h	Hot Temperature (°C)
T_m	Melting Temperature (°C)
V_B	Base Tank Volume (m^3)
V_R	Volume of the Receiver (m^3)
v_t	Terminal Velocity (m/s)
W	Work (J)
x	Fraction of Equipment Costs
y	Fraction of Contingency Costs
	Number of Hours of Storage
γ	Surface Energy (J/m^2)
ε	heat exchanger effectiveness
η_e	Efficiency
θ	Angle (rad)
μ	Viscosity (kg/m-s)
v	Velocity in *y*-direction (m/s)
ρ	Density (kg/m^3)
σ	Stefan-Boltzmann Constant (=$5.67x10^{-8}$ W/m^2-K^4)

LIST OF ABBREVIATIONS

Al	Aluminum
C	Carbon
CSP	Concentrated Solar Power
CTE	Coefficient of Thermal Expansion
DOE	Department of Energy
EIA	Energy Information Agency
He	Helium
HEX	Heat Exchanger
HTF	Heat Transfer Fluid
ID	Inner Diameter
kWh	Kilowatt Hour
kWh_e	Kilowatt Hour Electric
kWh_t	Kilowatt Hour Thermal
l	liquid
LCOE	Levelized Cost of Energy
LDHX	Liquid Droplet Heat Exchanger
LM	Liquid Metal
LM-CSP	Liquid Metal Concentrated Solar Power
LS	Liquid Salt
LS-CSP	Liquid Salt Concentrated Solar Power
N_2	Di-Atomic Nitrogen Gas
NREL	National Renewable Energy Laboratory
OD	Outer Diameter

O&M	Operation and Maintenance
PV	Photovoltaics
s	solid
SAM	System Advisor Model
S-CO_2	Supercritical Carbon Di-oxide
Si	Silicon
SiC	Silicon Carbide
Sn	Tin
TES	Thermal Energy Storage
TEA	Techno Economic Analysis
U	Heat Flux (W/m^2)
W	Tungsten
Zr	Zirconium

SUMMARY

Solar energy is an advantageous energy source because it's plentiful, free, and has zero net chemical footprint. The problem with solar energy is that it's dilute (1000 W/m^2) and intermittent, since it is inherently dependent on the weather. Therefore, an expensive sunlight collection and energy buffering/storage infrastructure is required for solar energy to meet demand at the utility scale. Concentrated solar power with liquid salt (LS-CSP) thermal energy storage (TES), is a commercially proven technology that delivers dispatchable electricity to the grid; however, it currently costs about twice as much as fossil fuel generation, which is a barrier to its wide spread adoption.

Current CSP plants operate at 565°C and utilize a steam Rankine power cycle with ~ 35-40% thermal to electrical conversion efficiency. One pathway to lower the levelized cost is to increase the operating temperature above 1,200°C enabling usage of a combined power cycle with an efficiency as high as 60%. Molten nitrate salts degrade at ~600°C, therefore a different heat transfer fluid is required for higher temperatures. Liquid metals (LM) can reach the high temperatures required for combined power cycles. However, LMs oxidize in air and corrode conventional structural materials such as steel. Switching from LS-CSP to LM-CSP necessitates replacing steel pipes, pumps, heat exchangers, and tanks with alternative materials, such as ceramics and encasing the subsystems in an inert atmosphere. Finally, a different receiver design that limits thermal radiation losses is necessary for efficient high temperature operation. The power cycle efficiency gains from higher temperature operation must outweigh the additional infrastructural costs of using LM in CSP for the approach to be feasible, but it is unclear if there is a net gain. This thesis addresses this question by presenting a LM-CSP plant

design and estimating its costs subject to many mechanical, chemical and materials criteria that would make the plant construction feasible.

Chapter 1 reviews the history of solar thermal technology and the motivation for further research and cost reduction. In chapter 2, the overall design of the LM-CSP plant is presented alongside a LS-CSP plant with published costs. The LM-CSP plant was modeled with the same thermal input as the LS-CSP plant to make direct cost comparisons and simplify the cost modeling of components that would not change in a hypothetical LM-CSP plant design. Chapters 3 through 7 present the component designs and costs for each of the four subsystems, namely the heliostat field, receiver, TES, and power cycle. Each subsystem was then compared against LS-CSP plant components to quantify the cost increase. Chapter 7 also includes the parasitic losses calculated for the LM-CSP plant and they were significantly lower than a LS-CSP plant, due to the higher thermal conductivity of LM as compared to LS or any other non-electrically conductive fluid. Chapter 8 presents all subsystem costs combined and the estimated levelized cost of electricity for a LM-CSP plant which was ~ 9 ¢/kWh and was a 30% cost reduction from the current state of the art LS-CSP.

Chapter 9 presents experimental work done building liquid tin (Sn(l)) pump loops. First, the experimental design to test a 1,350°C optical cavity receiver is described and the associated challenges for a successful test run, some of which were addressed with previous experiments. The solutions discussed in this thesis include Sn compatible ceramic pipes, graphite reaction bonds, graphite mechanical seals, LM valves, and minor flow losses in graphite elbows. The ultimate conclusion of the thesis is that there is strong economic incentive to pursue LM-CSP and further research should be conducted to solve

the remaining technical challenges, which all appear surmountable from the preliminary experimental studies.

CHAPTER 1: INTRODUCTION

Global climate change and energy demand has set new standards for electricity generation. Future generation technologies must deliver electricity on demand while limiting their environmental impact. Renewable sources like wind and solar photovoltaics (PV) meet the second criterion by providing electricity without emitting greenhouse gases. In some regions, wind and PV approach cost parity with traditional sources like coal and natural gas [1]. The approximate levelized costs of electricity (LCOE) for wind and PV are 7.4 ¢/kWh and 12.5 ¢/kWh respectively, which is cheaper than advanced coal with carbon capture and storage at 14.4 ¢/kWh (Table 1) [1]. LCOE is a cost metric that compares different generation technologies by summing all lifecycle costs (capital expenditures, fuel expenditures, operation, investments) and normalizing them against the electricity generated.

LCOE does not take into account when an energy source can deliver electricity to the grid. The issue of whether or not a resource can be dispatched by a utility and provide electricity at any time, is known as dispatchability. Wind and solar electricity conversion are weather dependent and cannot be controlled to match demand. Wind and solar are therefore inherently non-dispatchable because of their intermittent supply. Furthermore, their capacity factors (e.g., the proportion of operation at peak capacity) are less than half that of fossil fuel generation. When renewables make up a larger percentage of a utility's generation portfolio, dispatchability and capacity factor have real economic costs for the utility not taken into account with LCOE estimates [2, 3]. In order for renewable energy to transition from a minor grid supplement to an adequate fossil fuel replacement, cost effective energy storage is required.

Table 1: LCOE for plants entering service 2020 [1]

	LCOE (2013 ¢/kWh)	Capacity Factor, %	Dispatchable
Conventional Coal	9.5	85	Yes
Advanced Coal with CCS	14.4	85	Yes
Conventional Natural Gas Combined Cycle	7.5	87	Yes
Conventional Combustion Turbine	14.2	30	Yes
Wind	7.4	36	No
Solar PV	12.5	25	No
Solar Thermal, no storage	24.0	20	No

Current grid level energy storage relies primarily on pumped hydroelectric (hydro) and electrochemical battery technologies [3, 4]. Pumped hydro is inexpensive yet geographically limited [4], and works by pumping water uphill when there is a surplus of generated electricity. During peak demand, water is drained from the raised reservoir through hydroelectric turbines to match the supply with increased demand [5]. Pumped hydro requires natural streams and hills to be cost effective, limiting its use to current hydroelectric dam installations.

Batteries are not geographically limited and typically have roundtrip efficiencies above 70% [6, 7]. They can also quickly shift from charging to discharging within seconds, and are easily scalable. However, their costs are high ($150 to $600/kWh$_e$), and there is a tradeoff between their lifetime and discharge rate [6, 8, 9]. Thermal energy storage (TES) is a cost effective alternative to battery storage with an estimated cost of ~$60/kWh$_e$ for molten salt TES [10]. At large scales, it has a round trip thermal efficiency >99%, long life, and unlike electrical batteries, the amount of energy stored is decoupled from the rate of discharge [11].

TES works by heating a medium and storing it in an insulated tank until power is required. When electricity is needed, the heat is transferred from the heated medium to a power cycle. At large scales, where the surface area to volume ratio decreases, TES is efficient because thermal losses scale with the surface area while the amount of energy stored scales with the volume [11].

TES conceptually makes the most sense when the energy input is heat, rather than electricity, as is the case for an electrical battery. While joule heating from electricity is nearly 100% efficient, converting thermal energy back to electricity is thermodynamically limited by the second law and therefore it is a function of the peak TES temperature. Using today's best power cycles, the maximum thermal to electric conversion is ~60% and would require extremely high storage temperatures (>1200°C) [12-14]. Therefore, the most economically advantageous and efficient embodiment of TES is to pair it with concentrated solar power (CSP), where mirrors concentrate sunlight onto a receiver which heats the TES medium [15]. CSP already requires a thermal energy conversion step and the fuel (sunlight) that provides the thermal energy is, in a sense, free. CSP plants with TES can operate more like coal and natural gas plants, delivering dispatchable electricity to the grid with a capacity factor in excess of 40% [10].

Plant Configuration

A CSP tower plant with TES is composed of four subsystems: a heliostat field, a receiver, TES, and a power block (Fig. 1) [10, 14]. The heliostat field typically consists of many mirrors, typically 1,000-100,000 that cover an area on the order of a square mile, which concentrates sunlight onto a central tower. The heliostat field is the most expensive part of the plant, accounting for ~25-40% of the capital cost [10]. The concentrated

sunlight incident on the receiver is then absorbed and the energy is transferred as heat to the heat transfer fluid (HTF), which can be LS for TES or it can be used to directly generate steam [16, 17]. Current solar receivers are approximately 15 m in diameter and consist of cylindrical banks of parallel tubes (i.e., nickel alloy pipes) [17, 18]. The metal pipes are painted black to maximize absorption of the solar radiation, which heats LS flowing through the piping network. After the LS is heated, it is pumped down the tower to an insulated tank. The first tank stores LS at the peak storage temperature (565°C for LS-CSP plant) until electricity is required [10, 17]. When electricity is needed, the storage fluid is pumped from the hot tank through a heat exchanger to a cold storage tank. The heat exchanger transfers heat from the storage fluid to a power cycle working fluid, which is steam for LS-CSP plants. Once steam is generated, the remainder of the power block is nearly identical to that of other coal or nuclear plants. It consists of a pump to pressurize water, a boiler to heat it, and a turbine to generate work.

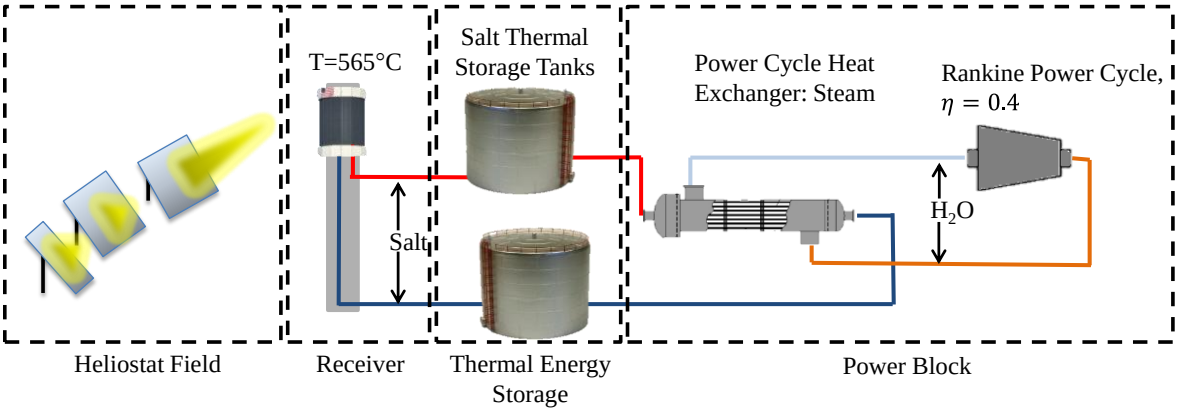

Fig. 1: LS-CSP plant schematic

Concentrated Solar Power History

Interest in concentrated solar power began in the late 1970's when spikes in oil prices prompted DOE labs to explore fossil fuel alternatives for energy production [19].

In 1976, engineers at Sandia National Labs constructed the National Solar Thermal Test Facility, which used water as a heat transfer medium to run a steam Rankine cycle and charge an oil + sand TES system [20]. This system, called Solar I, proved the concept of CSP with TES, operating from 1982 to 1986; however, its thermal storage system suffered from large inefficiencies. Elsewhere in the Mojave Desert, the Solar Electric Generating System (SEGS), was built in 1984. SEGS used parabolic trough technology where long troughs of mirrors with a parabolic cross-section concentrated sunlight onto a central oil tube running lengthwise along the mirror's focal line (Fig. 2).

Fig. 2: SEGS parabolic trough plant (NOAA)

In these plants, hot oil is heated to ~390°C and transfers heat to a steam Rankine power cycle with ~ 37.5% efficiency. The hot oil can be used for TES to provide power after peak sunlight hours. Parabolic trough technology is scalable and commercially proven, with 354 MW of installed capacity at the Mojave Desert site representing the second largest solar thermal installation (after Ivanpah Solar Power facility). However, solar trough plant's operating temperature is limited by the mirror geometry to 80X

concentration, heating oil to ~400°C [21]. Power tower designs achieve concentration ratios from 300 to 1,000 and can heat LS to 565°C. With the advantages of power tower's known, in the 1990's, solar I was converted to solar II by switching to LS as a heat transfer fluid and storage medium [20]. Solar II demonstrated the key advantages of LS-CSP, namely dispatchability and higher efficiency. It delivered electricity to the grid for 153 straight hours. Over one 30 day period, solar II produced 1,633 MW-hr, exceeding its monthly goal of 1500 MW-hr [20].

For 20 years, solar thermal energy was favored over photovoltaic systems because of the historically high cost of PV, as compared to CSP's mirror based infrastructure, which made CSP competitive with PV, even for direct power generation without TES [22, 23]. However, in 2010, PV cells saw a dramatic decrease in costs, largely due to major manufacturing scaling in China [24]. Since 2010, current solar thermal technology has not been able to compete with PV cells without storage.

Ivanpah, the largest solar thermal plant to date at 377 MW has no energy storage, and it is more expensive than PV (Fig. 3) [25]. When the plant was funded and contracted in 2009, its LCOE forecast was still cost competitive with PV. However, when construction finished in 2014, the plant capital cost was $5.40/W, which was higher than the cost of PV at that time $4/W [26, 27].

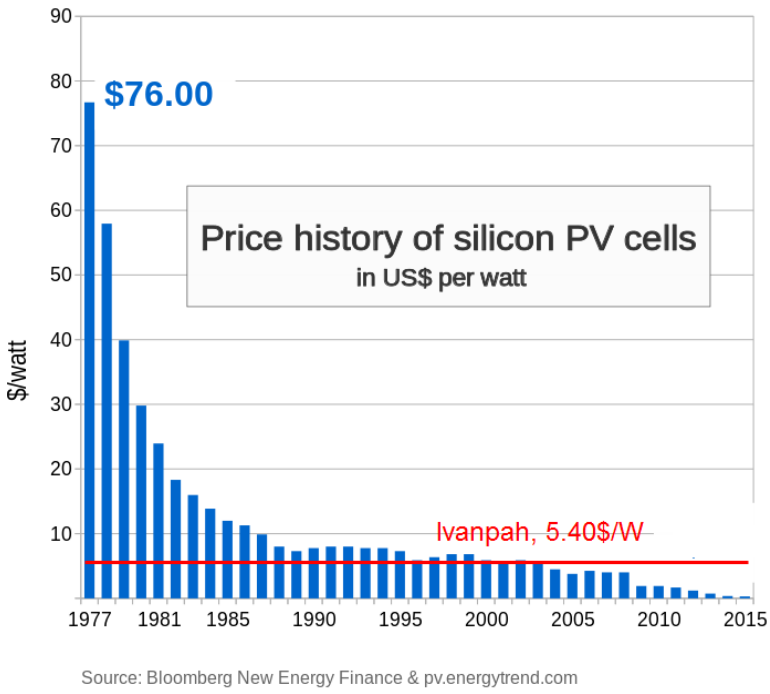

Fig. 3: Decline of PV prices. Ivanpah price plotted in red

This identifies an inherent disadvantage of CSP, namely the fact that large capital intensive projects, with long multi-year construction times are required. At such long time scales there is significant volatility associated with the costs of components, availability of suppliers and the strength and viability of competitors. However, where CSP plants have an advantage is in their ability to integrate TES for dispatchability. Electrochemical batteries are the primary commercial storage option for PV and wind, but the capital cost varies between ~\$120/kWh$_e$ for traditional lead acid batteries and ~600 \$/kWh$_e$ for new lithium ion batteries [9]. When one compares these costs to the cost of LS TES which is ~\$62.5/kWh$_e$ [10], then the cost advantages of TES become clear. Another disadvantage for battery storage is that the power output is a function of storage capacity and has a cost between \$300-1,200/W [6, 8]. For LS TES, electricity is produced by pumping LS through a steam generator powering a Rankine cycle.

Therefore, power production is decoupled from storage capacity and is priced according to the heat engine cost, $1.14/W for a Rankine power cycle [28].

There are two currently active commercial LS-CSP plants with TES, namely the Crescent Dunes plant in Nevada and the Gemasolar plant in Spain. Gemasolar is a 20 MW plant featuring 14 hours of storage and Crescent Dunes is a 100 MW plant with 10 hours of TES [29, 30].

Fig. 4: Crescent dunes LS-CSP plant (Solar Reserve)

Both plants provide dispatchable electricity without greenhouse gas emissions; the problem is that they are still too costly. While costs vary, power tower CSP plants have an LCOE of ~13.5-15 ¢/kWh$_e$, compared to ~7 ¢/kWh$_e$ for fossil fuel technology (see Table 1) [10, 29]. One promising way to reduce the costs of CSP plants is to increase plant efficiency. If a greater proportion of the solar energy collected can be converted to electricity without an accompanying increase in the cost of the plant, then the LCOE will decrease. The largest energy conversion loss occurs in the power cycle which converts thermal energy to electricity. Power cycles are thermodynamically limited by the working fluid inlet temperature with current LS-CSP plants utilizing a Rankine steam cycle with a

peak temperature of 565°C and an efficiency as high as 41%. However, the most efficient commercial heat engine has an efficiency of ~60% [12] and combines two power cycles: a natural gas Brayton cycle with peak temperature >1200°C, which then rejects heat to power a steam Rankine cycle at 550°C [13, 31]. Thus, in order for concentrated solar to power a more efficient combined cycle, higher operating temperatures are necessary. However, current nitrate liquid salts, 60% $NaNO_3$ and 40% KNO_3, degrade at ~600°C, where they would reduce to form nitrites and the stainless steel that holds them would experience a considerable decrease in corrosion resistance, due to chromium diffusing to the grain boundaries above 565°C [32-35]. Therefore, a new heat transfer fluid and storage medium is required for higher temperatures and more efficient cycles.

Higher temperature heat transfer fluids is an area of ongoing research and research groups are considering fluids ranging from fluoride salts, molten glass, sand particles, and LMs as possible high temperature alternatives to nitrate salts [36-40]. Storage fluids vary in cost, and many require special containment materials. This thesis focuses on LMs aluminum (Al) and Sn inside a ceramic containment infrastructure to reach ~1,400°C, whereby heat is converted to electricity via combined cycle. Some LMs are advantageous due to their low vapor pressure at high temperatures, low viscosity, and high thermal conductivity compared to liquid glasses and fluoride salts. Their primary benefit is storing high temperature heat to utilize a more efficient combined cycle heat engine. Increasing the TES temperature from 565°C to 1,380°C could increase power cycle efficiency from 40% to 60% - potentially a 50% increase in electricity generated while using essentially the same heliostat field.

There are, however, technical challenges associated with constructing a LM-CSP plant. Ceramic pipes, joints, pumps, and tanks need to be used instead of metal structures since LMs will generally corrode steels very quickly [39, 41]. Furthermore, the system needs to be maintained in an inert atmosphere so that the LM or in some cases the ceramics do not oxidize. Finally, the receiver needs to be redesigned to limit severe re-radiation losses from the higher receiver temperature. In order to determine if switching to LM-CSP decreases costs, the components for a LM-CSP plant were designed and cost estimated normalizing all costs with respect to the greater electric output. The LM-CSP plant was not optimized, but rather designed conservatively to more assuredly determine if LM-CSP could reduce costs compared to LS-CSP. The designed plant cost was 30 % cheaper and a significant step toward cost parity with fossil fuel electricity generation.

LM-CSP Experimental Set-up

With the economic potential established, extensive experimental testing of the proposed LM-CSP concept is necessary before constructing a prototype power plant becomes warranted. A scaled down LM pump loop with a miniature receiver was built to test the concept, which consisted of a LM pump to flow Sn(l) through graphite pipes. The Sn(l) entered a cavity receiver designed to limit re-radiation losses and was heated by concentrated light from a solar simulator. The simulator was a set of lamps that simulated the solar intensity of a heliostat field on a smaller scale. The LM was then cooled via a heat sink and the whole loop was contained within a 4’ x 4’ sealed steel box that was pumped with nitrogen to remove all oxygen from the experiment.

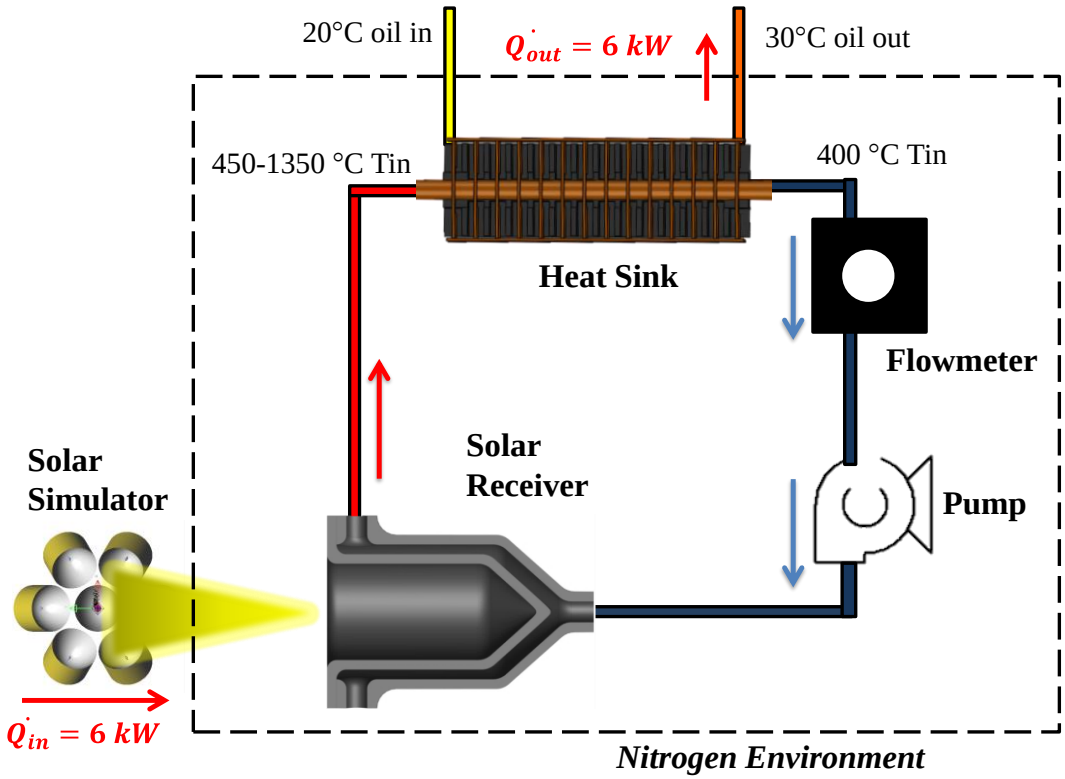

Fig. 5: Schematic of graphite receiver test loop.

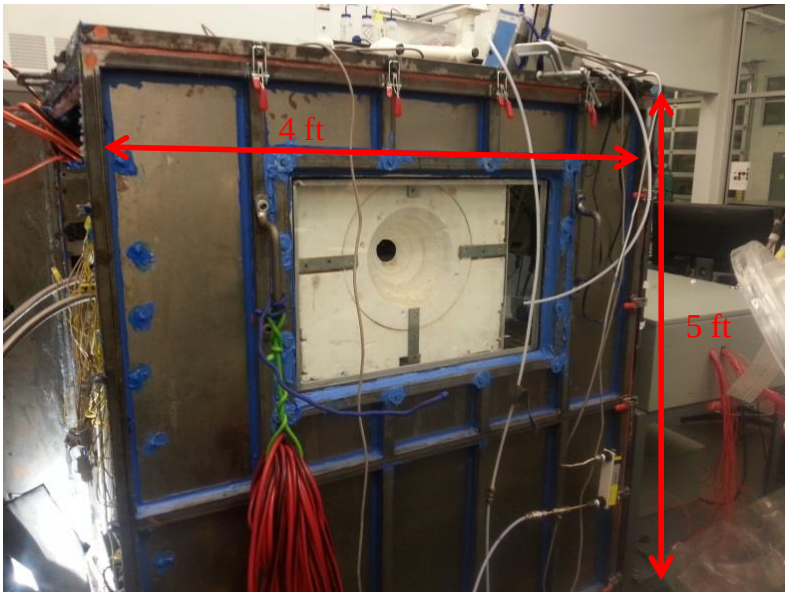

Fig. 6: Receiver inlet contained within inert containment box

Experiments characterizing receiver efficiency were ongoing at the publication of this thesis and the lessons learned from these experiments are discussed in Chapter 12. From Sn(l) circulation experiments at 400°C, the compatibility of Sn(l) was experimentally verified with two different pipe materials. Techniques for joining graphite via reaction bonding were largely improved and mechanical sealing methods were proven. Furthermore, graphite joint minor (frictional) loss experiments and ceramic ball valve experiments led to engineering solutions that could be applied at larger scale and make LM-CSP a technical reality.

CHAPTER 2: TECHNO-ECONOMIC ANALYSIS METHODOLOGY

CSP Plant Levelized Cost of Electricity

The LCOE for a 100 MW CSP power tower plant with 10 hours of TES is ~ 13.5-21¢/kWh. To be cost competitive with traditional energy sources like natural gas and coal, this cost must drop to 6-7¢/kW-hr [10, 42] and reaching or exceeding this goal requires significant research and cost reductions in each of the four CSP subsystems, (the solar field, the solar receiver, TES, and the power block).

The LCOE for a power plant can be calculated according to the following Eq.:

$$LCOE = \frac{\sum_{t=1}^{n} \frac{I_t + M_t + F_t}{(1+r)^t}}{\sum_{t=1}^{n} \frac{E_t}{(1+r)^t}} \quad (1)$$

where I_t is the investment expenditures in the year t, M_t is operations and maintenance expenditures in the year t, F_t is the fuel expenditures in the year t, E_t is the electricity generation in the year t, r is the discount rate, and n is the life of the system. In CSP plants, one of the most effective ways to lower LCOE is to reduce investment expenditures, I_t, because for CSP, the fuel is free and the maintenance costs are low (1-2% of initial investment) [10]. Therefore, investment expenditures dominate the LCOE and most investment expenditures occur before or during construction. The investment expenditure to build the plant, I_1, is given its own variable, K, and is defined as the overnight capital cost [1].

In order to lower the LCOE of CSP, the overnight capital cost, K, needs to be decreased and since the capital cost is normalized by electricity production, given in $/kW$_e$, K can be lowered by reducing the construction costs, increasing the plant output,

or both. Increasing output can be accomplished by improving the thermal to electric efficiency of the power cycle, possibly from 40% to 60%, which requires raising the operating temperature from 565°C to ~1,400°C. Achieving higher temperatures in a CSP plant presents many challenges, the first of which is identifying a heat transfer fluid (HTF) that is stable at 1,400°C and melts at sufficiently low temperature that it will not freeze during daily transients. Liquid nitrate salt is currently used in CSP plants, but it degrades at temperatures above 600°C [43]. A promising alternative to LS is a LM such as Sn. Sn melts at 232°C, and even at 1,400°C, it remains liquid with a vapor pressure less than 10^{-4} atm [44]. However, traditional steel based components, such as pumps, piping, and storage vessels, cannot be used with Sn(l) due to the high temperatures involved and the accelerated corrosion that would occur [45, 46]. Refractory ceramics and graphite, however, can be used to design a CSP plant that employs Sn(l) as a HTF. The potential advantages of Sn(l) include access to higher temperatures, and the possibility of using a significantly more efficient power cycle. The potential disadvantages include higher material costs, higher assembly costs, and higher initial capital costs due to a more complex or expensive system design (e.g. the receiver).

Cost Estimation Methodology

The goal of the techno economic analysis was to estimate the LCOE of a LM-CSP and compare it against the LCOE of LS-CSP plant on equal footing. The LCOE for a natural gas plant is also presented for comparison using a similar system size and capacity factor. The capital costs for a CSP plant was broken up into four sub-systems: a solar field, a solar receiver, TES, and a power block. The primary reference used for LS-CSP plant costs was Sandia's "Power Tower Technology Roadmap and Cost Reduction

Plan" [10]. This report detailed the costs of a LS-CSP plant optimized using NREL's System Advisor Model (SAM). The modeled plant had a gross output of 115 MW_e, with a net output of 100 MW_e (after parasitic losses) and 9 hours of energy storage. The hypothetical LM-CSP plant had the same heliostat field (1.04×10^6 m^2), receiver output (540 MW_t), storage capacity (9 hours), and thermal input to power cycle (280 MW_t) as Sandia's modeled LS-CSP plant, but used a 60% efficient combined cycle with 168 MW_e gross output instead of 115 MW_e. All plant capital costs were normalized against this higher electric power output, which, for example, significantly reduced the LCOE of the heliostat field despite its identical capital cost to the LS-CSP plant.

For cost modeling the proposed LM-CSP plant, the heat exchangers, receiver, storage fluid, TES tanks, and piping were significantly different. Furthermore, additional systems such as inert containment and secondary concentrators were necessary to build a LM-CSP plant. Using heat transfer and thermodynamic relations, the geometries for these components were modeled for the plant configuration discussed above. Material cost factors were then applied to estimate costs. Cost assumptions and questions were discussed with industry advisors from eSolar, SolarReserve, Saint Gobain, and Westmoreland Advanced Materials to determine other possible costs unaccounted for in initial modeling. When uncertainty in the design or particular cost factor was encountered in the LM-CSP plant, the more expensive and conservative option was used. For example, controls, instrumentation, spare parts, and pumps were costs outlined for the LS-CSP plant that were difficult to estimate for a LM-CSP plant using heat transfer and thermodynamic relations. Instead, a 2X cost factor was applied, which was typically the difference in volumetric material cost between stainless steel, used primarily in LS-CSP,

and silicon carbide (SiC), a refractory ceramic for LM containment [47]. While this was a coarse estimation strategy, these costs did not represent a large proportion (<5%) of CSP subsystem costs and in reality, would likely be similar to a LS-CSP plant.

Construction costs for the LM-CSP plant were estimated from the published cost numbers for the LS-CSP plant and discussions with industry advisors. The largest construction cost, the heliostat field, was the same for both plants since both plant designs used the same heliostat field. Receiver construction costs were taken from Solar Reserve estimates and TES construction costs were scaled to the LM TES design using published scaling relations [10, 29]. The power cycle construction costs were already included in the published estimates for combined cycles [48].

LS- CSP Plant Configuration

To make direct comparisons between LS-CSP and metal CSP plants, a single size plant was modeled. The heliostat field size and thus thermal input was identical between both plants. The plant size was based off of Sandia's power tower roadmap which published cost numbers for LS-CSP tower subsystems [10]. The theoretical LS-CSP plant had 115 MW_e gross electric output with 9 hours of TES, with a Rankine cycle efficiency of 41%, and therefore required a thermal input of 280 MW_t from the TES [49]. With 9 hours of TES, the plant featured an external receiver that produced 540 MW_t during peak sunlight hours. The solar receiver was sized larger than the power cycle input so a portion of the collected peak sunlight could be diverted to the TES while still running the plant at peak power output. In addition to Sandia reported cost numbers, this size plant was modeled in NREL's System Advisory Model to obtain additional parameters and costs not present in the report [35]. This size plant design was similar to Solar Reserve's

Crescent Dunes solar energy project which had 110 MW_e output and 10 hours of direct LS TES [36].

The LS-CSP plant consisted of the four previously mentioned subsystems: a solar field, a solar receiver, TES, and a power block. The solar field consisted of mounted mirrors with 2-axis tracking systems termed heliostats, which focused sunlight onto a central receiver that sat atop a tower. This external receiver was heated by sunlight and cooled by circulating LS through it. The hot LS could be stored in storage tanks or used immediately to produce electricity by exchanging heat with water to create steam to drive a Rankine power cycle (Fig. 7).

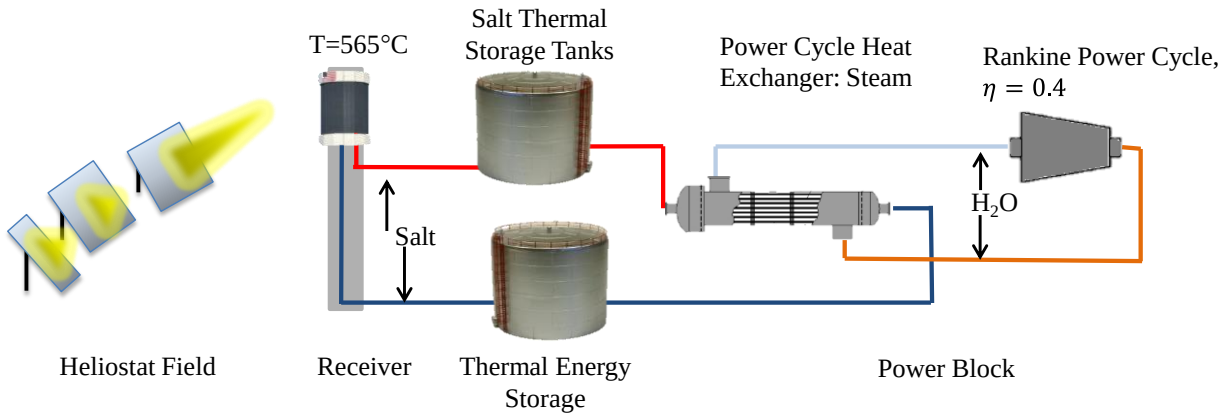

Fig. 7: LS-CSP plant

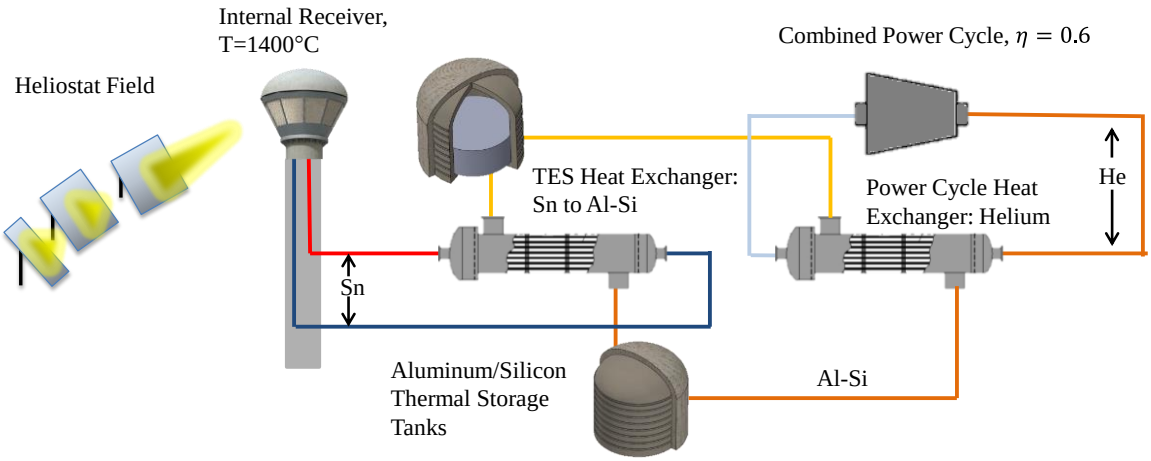

Fig. 8: LM-CSP plant configuration

LM-CSP Plant Configuration

The LM-CSP plant proposed in this TEA had the same four subsystems as a traditional LS-CSP plant albeit with significant modifications (Fig. 8). The heliostat field for the LM-CSP plant design had the same total area as the LS-CSP plant. However, the LM-CSP plant required higher concentration ratios to achieve higher temperatures. Secondary concentrators surrounded the receiver to increase concentration from 1,000 suns to > 5,000 suns.

The most significant difference between the two plant designs was that the heat transfer fluid in the receiver was not used as the thermal storage medium. Sn was too expensive to be used as a thermal storage medium, even when purchased in large quantities as 98% pure scrap (often referred to as "block Sn"). Block Sn was $8.40/kg and the material cost was normalized to the thermal energy stored by dividing by the temperature dependent specific heat integrated over the temperature cycle [50]. Cycling Sn from 290°C to 1,400°C, resulted in a cost of $120/kWh$_t$. This cost, without any additional supporting components, was already as high as lead acid electrochemical

batteries and therefore was deemed too expensive to provide CSP with an economic advantage. Al-Si alloys with 30 atom percent (%at) Si ($Al_{0.7}Si_{0.3}$) had a cost of ~$1.70/kg and was much more energy dense due to the heat of fusion that occurred during solidification 577-822°C [51]. Cycling Al-Si from a solid at 290°C to a liquid at 1,350°C, had a cost of $3.50/$kWh_t$, which was an order of magnitude cheaper than Sn(l) [50]. This then raised the question of why one should use Sn at all, and the reason is that Al would react with graphite to form Al3C4, faster than a protective SiC layer. This then necessitated a separate, smaller Sn circulation loop to transfer heat from the receiver to the Al-Si storage medium. The receiver required a refractory material with a high thermal conductivity for high efficiency [52]. Graphite, aluminum nitride (AlN), (SiC) and beryllium oxide (BeO) were some of the only known refractories that should be compatible with Sn, but also have sufficiently high thermal conductivity > 30 W/m-K at 1,350ºC [53-55] to yield a highly efficient receiver. BeO, however, was carcinogenic and therefore had associated safety concerns [56]. AlN was inert with respect to Al(l) but had a cost three times as much as graphite pipe of similar dimensions, based on price quotes from two suppliers [Precision Ceramics, Graphitestore.com]. Furthermore, although AlN was potentially attractive from a cost perspective at large volumes, given the low cost of the constituent elements, there was currently no supplier of large AlN tubes, which would be needed for a MW level receiver. SiC was also inert with respect to Al-Si alloys with sufficiently high Si contents, and comparable in cost to graphite; however, it suffered from thermal cycle fatigue, which was especially severe in the receiver [47]. Given these constraints, graphite was the chosen refractory containment material and a separate Sn(l) receiver circulation loop with a silicon carbide heat exchanger would serve as the

interface between Sn and Al-Si in the TES subsystem. Here the idea was that the Al-Si portion of the system contained the majority of the thermal mass and therefore it did not experience the drastic 10 min extreme transients that the receiver would experience due to cloud cover etc. (see Fig. 8).

To take advantage of high temperatures, a Brayton cycle gas turbine was run from 1,350°C to 850°C where waste heat from the turbine was then transferred to a supercritical CO_2 (SCO_2) cycle which extracted the remaining heat (Fig. 30). This configuration was similar to current combined cycle power plants which used natural gas Brayton engines from 1,400°C to 700°C and then a Rankine bottoming cycle from 565°C to 30°C [13]. In natural gas Brayton cycles, heat is added via combustion of the air -gas mixture, while in a CSP plant, combustion would not be necessary, since all of the heat would be added via a heat exchanger to pass heat from Sn(l) to an inert gas working fluid that drives the Brayton cycle turbine.

With high operating temperatures (1,400°C) and LM, material compatibility and oxidation were important concerns [39]. To mitigate against oxidation, LM components would be contained in an inert (i.e. N_2) environment to avoid oxidation of critical components, namely the receiver and TES. An inert containment system would then surround the LM containing pipes as well as the various subsystems.

Overall Capital Costs

By inspection of Eq. (3), the overnight capital cost, K_{tot}, and the overall efficiency were expected to be the primary differences between the LS-CSP and LM-CSP systems. Overnight capital cost was the construction cost for a plant, which is typically normalized

by the plant's peak electricity output so that it can be compared directly to other forms of generation. The total overnight installed cost was given by,

$$K_{tot} = K + K_1 + K_2 \tag{2}$$

where K was the direct equipment costs, K_1 was contingency, and K_2 was indirect costs [57]. The direct equipment costs, K, was calculated as follows:

$$K = \frac{A}{E} + \left(\frac{B}{\eta_E}\right) \times F + \left(\frac{C}{\eta_E}\right) \times t + D \tag{3}$$

In Eq. 3, there were four terms, each in units \$/kW_e for the four subsystems. A was the cost of solar energy collection in \$ and E was the plant electrical output in kW. A included site preparation and the material cost of the solar collection field (mirror, supports, drives, installation etc.) B was the cost of the solar receiver in the case of a power tower configuration, given in \$/kW_t. Here, the subscript 't' denoted that the output power was thermal, not electrical. Thermal power was converted to electrical power via the power cycle, which had efficiency η_e. F was the solar multiple, which described how much greater the maximum allowable power input was for the receiver than the power cycle. A solar multiple greater than unity meant more energy was captured and stored during the day than would be used while the sun is out, which allowed the remaining stored energy to be used after daylight hours. C was the cost of thermal storage (\$/kWh_t), t was the number of hours of storage, and D was the cost of the power cycle (\$/kW), which was expressed in terms of the electrical output power. The contingency costs K_1 and indirect costs K_2 was calculated as follows:

$$K_1 = x \times K \tag{4}$$

$$K_2 = y \times (K + K_1) \tag{5}$$

where x and y were fractions of the equipment plus contingency costs used to determine the contingency and indirect costs respectively. The 2012 Sunshot Vision Study, published by the DOE, modeled contingency and indirect costs as x=0.1 and y=0.17 [1]. The total overnight installed cost for the LS-CSP plant was given by Sandia's power tower roadmap [10].

Table 2: LS-CSP plant capital costs (2011)

	LS-CSP ($/kW$_e$)
Solar Energy Collection Cost	1,879.4
Solar Receiver Cost	562.7
Thermal Storage Cost	535.3
D, Cost of Power Cycle	1,274.0
K1, Contingency	425.1
K2, Contingency	795.0
Ktot, total overnight installed cost	5,471.5

Cost Report Structure

Each subsystem from Table 2 was fully described for the LM-CSP plant in the subsequent chapters, where the overall cost breakdown of the components that made up each subsection were presented first, followed by detailed design and material selection. Parasitic losses for the LM-CSP plant were presented as well and the final section in the report estimated the operation and maintenance (O&M) costs and combined them with modeled overnight capital costs to calculate the LM-CSP plant LCOE. This LCOE was then compared against those of LS-CSP and natural gas.

CHAPTER 3: SOLAR ENERGY COLLECTION

Section Overview

The solar energy collection price was based on the cost of the heliostat field including mirrors, supports, tracking systems, installation, and site preparation. The total cost of the heliostat field, K_f, was normalized to \$/kW$_e$ by using the following cost formula:

$$K_f = \left(\frac{A}{E}\right) \tag{6}$$

where A was the cost of the solar energy collection and E was the net electricity generation of the plant.

To determine the heliostat field total cost, a 100 MW$_e$ LS-CSP power tower plant utilized a 540 MW$_t$ receiver and 9 hours of energy storage located in Tonopah, Nevada was modeled using SAM [49]. This was the same size plant used in the Sandia Power Tower Technology roadmap, which allowed for direct comparison between the studies [10]. Based on the receiver thermal output, solar multiple, and insolation at Tonopah, SAM recommended 1.042 million m^2 of mirrored area priced at \$180/m^2 for a total solar energy collection cost, A, of \$188M or \$1,879/kW$_e$ [35].

The LM-CSP plant was modeled using the same heliostat field as the LS-CSP design so A remained the same as the LS-CSP plant. It was also assumed that the sunlight to thermal conversion efficiency remained the same between both plants so their thermal input to the turbines was identical: 280 MW$_t$. Although the LM-CSP plant used a different type of receiver, this assumption was based on the design goal for the high temperature LM receiver, which was 90% conversion of incident light to thermal energy

and was the same conversion efficiency used in SAM's external receiver [58, 59]. Furthermore, modeling efforts showed that such a high efficiency was attainable with incident fluxes on the order of 1,000 kW/m2 into secondary concentrators that increased the flux to 5,000 kW/m2 as it entered the cavity [52].

Heliostat Field Discussion

As compared to LS-CSP, the difference between the power cycle efficiencies made the heliostat field significantly cheaper on a per kW_e basis in a LM-CSP plant. Although both LS-CSP and LM-CSP plants were modeled with the same heliostat design, the power cycle efficiency, η_E, was 0.41 for the LS-CSP plant and 0.6 for the LM-CSP plant. Factoring in parasitic losses for the LS-CSP and LM-CSP, the net efficiency was 0.36 and 0.58 respectively. The LM-CSP plant therefore produced more electricity using the same size heliostat field as a LS-CSP plant, resulting in a normalized solar energy collection cost of \$1,159/kW_e, which was 38% cheaper than the LS-CSP normalized solar energy collection cost of \$1,879/kW_e. Considering that the heliostat field alone was the single most expensive component of the system, the LCOE would be decreased by 13% in the case of the LM-CSP plant, just due to the reduction in power output normalized heliostat field costs [10], if all other variables remained the same.

Further optimization in the LM-CSP plant design has potential to further reduce field size costs. The LM-CSP plant heliostat field modeled in this TEA was not optimized for an internal receiver design with a peak LM temperature of 1,400°C. Instead, the necessary concentration increase was included in the receiver sub-system by adding secondary concentrators. In reality, the heliostat field and receiver costs were coupled and there was an optimum configuration to minimize total plant costs. More

expensive tracking and smaller mirrors could have achieved greater concentration ratios than the 1,000 kW/m2 (1,000 suns) typically obtained in state of the art plants today. Higher concentration by the field would in turn have decreased the size of the receiver and the requirements of the secondary concentrators. Since the receiver and secondary concentrators would have been made from expensive materials (machined graphite and polished optical components), minimizing its size at the expense of solar field costs could have reduced overall costs beyond this current estimation. On the other hand, a coupled system analysis might have led to the opposite conclusion; it may have turned out that it was cheaper to use less expensive controls in the field, decreasing the concentration achieved by the heliostats, while relying on more of the concentration that could have been achieved with the secondary concentrators. Further optical analysis and evaluating the respective tradeoffs is needed to determine the optimal system configuration for minimizing total LCOE. However, such an analysis was beyond the scope of the current investigation. Therefore, for the remainder of the ensuing analysis, it was assumed that the heliostat cost was the same and that the field supplied the necessary optical concentration to reach 90% efficiency at 1,400°C, once supplemented by secondary concentration.

CHAPTER 4: SOLAR RECEIVER

Section Overview

The solar receiver cost (K_R) included the cost of the receiver, secondary concentrators, tower, cold salt/metal pumps, inert atmosphere containment for the receiver, controls/instrumentation, and spare parts. The total cost of the receiver, K_R, was expressed in units of \$/kW using the following cost formula:

$$K_R = \left(\frac{B}{\eta_E} \right) \times F \tag{7}$$

The receiver was sized to produce more thermal power at peak sunlight hours than the power cycle could handle. This oversizing allowed energy to be stored while continually running the power plant at peak capacity during peak sunlight. Therefore, receiver costs were normalized by the maximum thermal power output (540 MW_t) of the receiver, B (\$/kW_t). The solar multiple, F, indicates how large the thermal output of the receiver was compared to the thermal input of the power cycle by dividing the receiver peak thermal output by the power cycle thermal input. A larger solar multiple translated to more hours of energy storage. For the plants modeled in this paper, F= 1.94 which translated to 9 hours of storage given the solar resource, Tonopah Nevada [60]. Costs were converted to \$/kW_e by dividing by the power cycle efficiency, η_E.

Switching to a LM receiver required changes in materials and geometry, as well as adding two components: inert containment and secondary concentrators. Controls/instrumentation and spare parts were a small proportion of receiver costs – approximately 1% – so the LM-CSP plant values were set equal to 2X the LS-CSP plant values given from Sandia's Power Tower Roadmap [10]. Here, the 2X estimate was the

difference between stainless steel and mullite, the common structural ceramic for LM-CSP. For the LS-CSP plant estimates, the receiver and tower costs were obtained from the SAM, while the cold pump, controls/instrumentation, and spare parts were taken from the Sandia Power Tower Roadmap [10]. Table 3 shows the cost breakdown between the two plant designs.

Table 3: Receiver subsystem cost comparison

	LS-CSP			LM-CSP		
	Total (M$)	$/kWt	$/kWe	Total (M$)	$/kWt	$/kWe
Receiver	30.0	55.6	300.6	63.1	116.9	390.0
Tower	22.4	41.5	224.4	25.0	46.2	154.3
Cold Salt Pumps	2.8	5.2	28.3	5.6	10.4	34.9
Inert Atmosphere Receiver	0.0	0.0	0.0	1.2	2.2	7.4
Controls and Instruments	0.5	0.9	4.7	0.9	1.7	5.8
Spare Parts	0.5	0.9	4.7	0.9	1.7	5.8
Total Capital Cost	56.2	104.0	562.7	99.5	179.2	598.1

Tower

The tower for CSP plants supported the receiver at the required height (Fig. 9) which was mainly a function of the heliostat field size. A taller tower reduced cosine losses from the reflected sunlight but increased receiver costs. SAM optimized the tower height for a prescribed heliostat field and since the heliostat field size was identical between both plants, the tower was the same height between both plants. However, the LM-CSP tower used ceramic pipes, which were an added cost compared to the stainless steel pipes in a LS-CSP tower.

Fig. 9: An example tower constructed for the Crescent Dunes CSP plant in Nevada

The LS-CSP power plant modeled in SAM had a tower cost of $22M, which was normalized to receiver thermal output as $40/kW$_t$. This tower cost included the construction work, and the cost of both the concrete column and the stainless steel piping. The LM-CSP plant used the same tower dimensions and foundation, but different pipes, which were made of mullite. Mullite was selected for the pipes because it was chemically compatible with Sn(l) and less expensive than graphite.

The tower pipe cost for the LM-CSP was determined from an online vendor of mullite pipes. Using a few larger diameter pipes minimized the frictional head loss for Sn going up and down the tower as well as the required pipe material. The largest diameter mullite pipe available had an outer diameter of 104 mm and was $780/meter [61]. By comparison, 316L stainless steel pipe with an OD of 104 mm used for the same purpose in LS-CSP plants was $321/meter [62]. The mullite pipe was approximately 2.5X the cost of stainless steel pipe.

To estimate the mullite piping cost in the tower, the total length of pipe was determined. To estimate pipe length, first the number of pipes in parallel was calculated based on frictional head loss. The number of pipes used in a cluster was used to determine its effect on the LCOE (Fig. 10). The pipe surfaces were assumed to be smooth and the Sn viscosity at 290°C (0.97 cP) was used going up the tower [44], which was a more conservative estimate, since the viscosity decreased at higher temperatures. Head loss coming down the tower was neglected, because the Sn portion of the circulation loop was modeled as an open loop whereby gravity drives the flow down the tower.

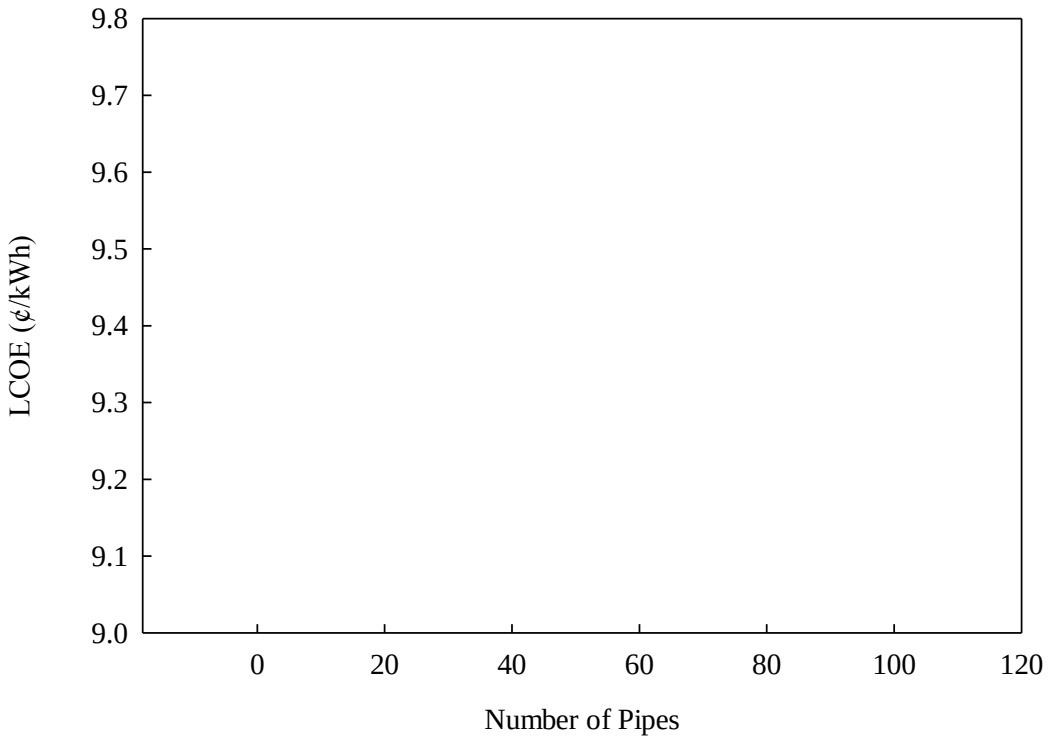

Fig. 10: LCOE vs. number of pipes

If only one pipe was used, the Sn velocity was high, which contributed to a large pressure loss and high parasitic loss that increased the LCOE. Adding more pipes increased capital

costs, but reduced the parasitic losses, which decreased the LCOE until more than 10 parallel pipes were used. Using 10 pipes optimally balanced parasitic pumping cost vs capital cost, and gave a tower height of 180m, which required 3,600m of pipe. With a cost of $780/m, the mullite pipe had a cost of $2.8M or $5/kWh$_t$. The tower cost given by SAM already included stainless steel pipe; however, the construction costs vs. piping costs were not delineated in SAM. Therefore, to obtain a more conservative cost estimate, the price of the mullite pipes was simply added to the SAM tower costs. Given that the mullite pipe was about 2.5X the cost of the stainless steel pipe and that the piping was a relatively small portion of tower cost, this assumption did not have a strong effect on the final conclusions. As a result, for the LM-CSP plant, the tower was estimated to cost $25.0M or $154/kW$_e$. For the LS-CSP plant, the tower had a cost of $22.4M or $224/kW$_e$.

Receiver

On top of the tower sat the solar receiver which converted concentrated sunlight to sensible heat in the HTF. Current LS receivers are external receivers, where metal pipes are arranged vertically in a 15 m diameter cylinder. Concentrated sunlight illuminates the outside of the pipes, and the LS flowing inside is heated to 565°C.

Fig. 11: External receiver

The cost estimation for the external LS receiver was verified based on discussion with representatives from SolarReserve. The Crescent Dunes site featured 10 hours of TES and 100 MW_e output, which was almost the same performance for the modeled LS-CSP plant, which had only 9 hours of storage. The estimated receiver cost of $74-92/kWt was close to the estimates from Sandia's report ($71-86/$kW_t$) [10], which for an external receiver, coupled with 9 hours of TES. For the LM receiver cost estimates, the initial design cost was not estimated. Therefore, for accurate cost comparison, the design cost of the LS receiver (estimated at $20M) was subtracted from the LS receiver cost ($50M) and gave a receiver cost of $55/$kW_t$, which was ultimately used in the LS-CSP plant cost model.

Internal Receiver Design

The receiver temperatures for the LM-CSP plant were much higher than the LS-CSP plant (e.g., 1,400°C vs. 565°C). Re-radiation losses scaled with the receiver temperature to the fourth power; therefore, a different receiver geometry was necessary to limit re-radiation losses. Experiments using the internal optical cavity receiver design depicted in Fig. 12 were ongoing during publication of this TEA. Light passed through a cone of insulation at the front of a graphite cavity. This cavity was surrounded by Sn(l) and heated the Sn while limiting re-radiation to the environment.

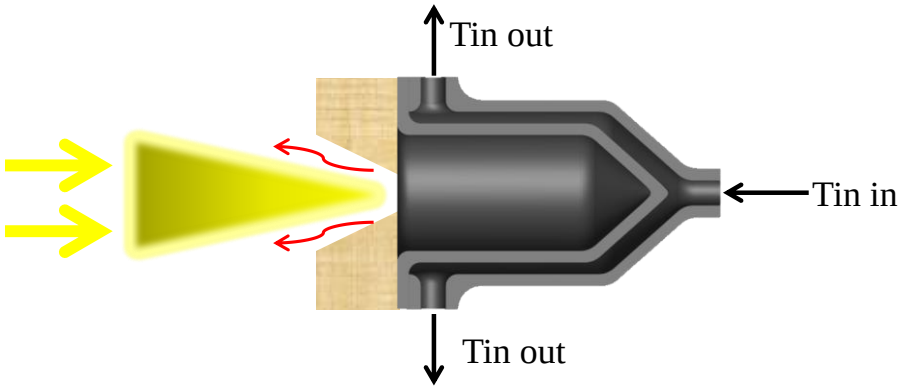

Fig. 12: Cross section of cavity receiver. Focused incoming sunlight is represented by the yellow triangle. Re-radiating light is the red arrows. Aperture insulation is tan. The graphite receiver is gray.

For a full scale receiver, one concept was to tessellate many of these cavity modules around a cylindrical surface. Secondary concentrators in front of each module then concentrate the heliostat field light from 1,000 suns to 5,000 suns, which enabled high receiver temperatures (Fig. 13).

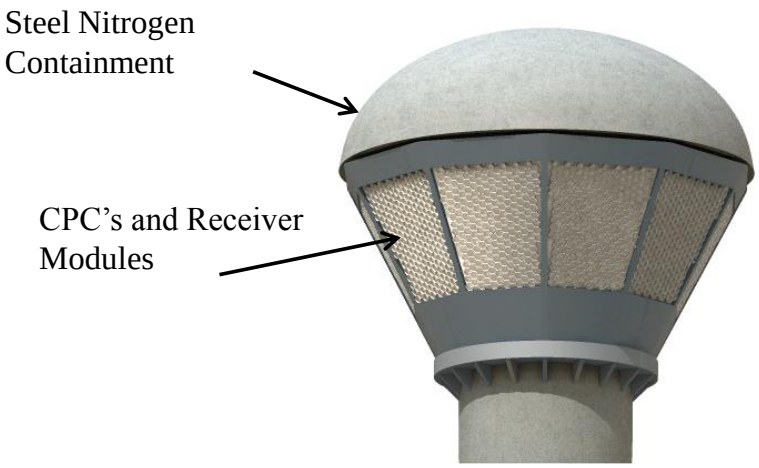

Fig. 13: Internal receiver with nitrogen containment

For the LM-CSP cost model, the internal receiver was composed of 4,147 cavity receivers (Fig. 13), which were arranged in 128 columns of 36 receivers each. The number of receiver modules, *M*, was determined based on the heliostat field, receiver module size, and the surface area of the LS-CSP plant external receiver:

$$M = \frac{\pi \times D_{rec} \times H_{rec} \times P}{\pi \times r_{\mathrm{mod}}^2} \tag{8}$$

D_{rec} was the diameter of the external receiver (15 m), H_{rec} was the height of the external receiver (18 m), r_{mod} was the radius of the receiver module (0.25 m), and *P* was the packing factor for circles (0.9). It took 4,147 receiver modules to cover the surface area exposed to the heliostat field.

As a nominal design choice, the Sn flowing into the receiver was split into 260 separate streams, each of which passed through a total of 16 cavity receivers spaced evenly around the entire perimeter of the large receiver. The Sn flow was split into parallel paths to limit the flow speed and thus the corresponding head loss through the receiver. However, 16 receivers were placed in series so that one receiver module did not

experience the full temperature range of the Sn (290°C to 1400°C) thus limiting thermal stresses.

Another reason for flowing a single stream of Sn through several receiver modules was to account for differences in solar intensity on different sides of the tower. For example, when the sun rose in the morning, the western side of the receiver experienced higher solar flux due to the difference in cosine losses between the western and eastern mirror fields. Combining 16 modules to one Sn stream that spanned the full receiver perimeter averaged out temperature differences on opposing receiver sides (Fig. 14).

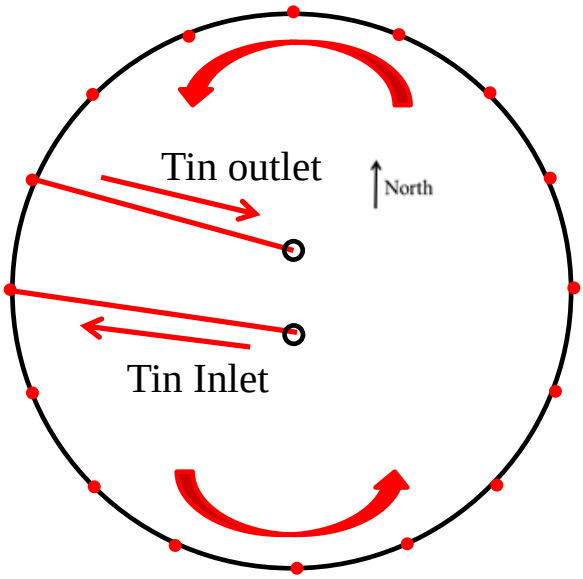

Fig. 14: Top-down view of the solar receiver showing cavity receiver locations. The large black circle represents the receiver perimeter, while the red dots represent all 16 cavity receivers through which Sn flowed while traveling along a single path. The Sn pipe path started at the center of the receiver base, flowed vertically (out of page) to appropriate height, flowed around a full perimeter of the receiver, then flowed back to the center of the receiver.

These 260 paths required ~21,750 m of graphite pipe to feed Sn to the receiver modules. The length of one path was calculated by adding the distance from receiver center and to the perimeter and back (16 m) with the circumference to connect all 16 modules (50 m) for a path length of 66 m. Some streams were at different heights than

others because the receiver was 18 m tall so the average stream height, 9 m, was added twice to each stream path. Multiplying the connecting pipe required for one stream (84 m) by the total number of streams (260) gave 21,750 m of connecting graphite pipe. In this model, each receiver was a hexagonal prism, composed of 70 graphite tubes, each 0.8 m long (Fig. 15).

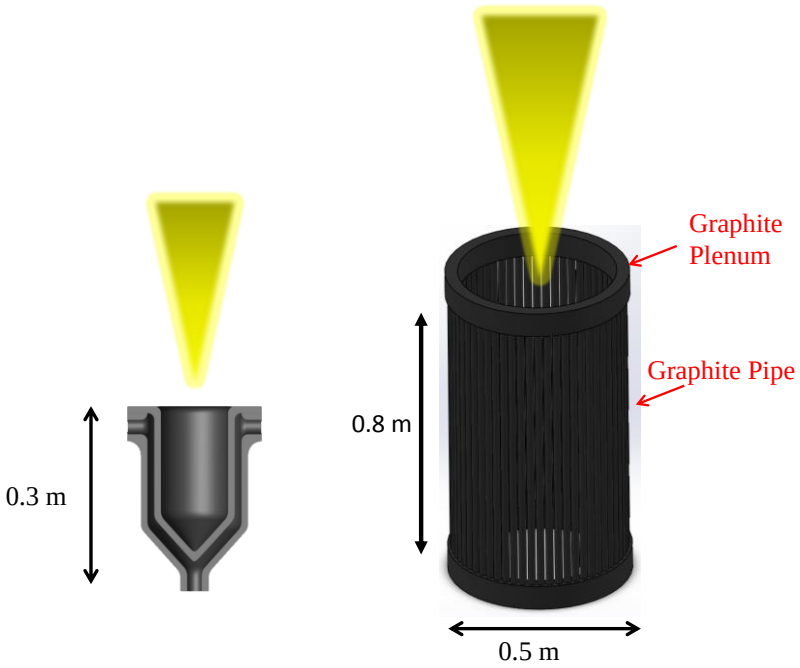

Fig. 15: (Left Side) Monolithic small scale receiver module. (Right Side) CAD drawing of a full scale cavity pipe receiver module. Light is emitted into the receiver at the top of the Fig.

This geometry approximated the custom monolithic graphite receiver used in small scale experiments by building a similar, larger geometry from commercial graphite tubes. The graphite tubes had a 1 cm inner diameter and 2 cm outer diameter. In order to fill the circumference of the 0.5 m diameter module, 71, 2 cm diameter tubes were required. Insulation was used to fill any space between pipes, which prevented light from escaping

the receiver. Each receiver module required a total of 56.8 m of graphite pipe and with 4,147 modules, the total length of piping needed was 235,550 m, or 0.43 m/kW_t.

The graphite receiver cost was subdivided into several components: the piping network connecting receiver modules, the graphite piping in each receiver module, and the plenums in each receiver. The graphite pipe used for the connecting pipes and receiver modules was uniform with a 2 cm outer diameter (OD), a 1 cm inner diameter (ID) and 1 m length that had a cost of $111, or 0.02 ¢/$kW_t$. One custom graphite plenum ring for each module end was $2,400, or 44 ¢/$kW_t$, which was based on quotes obtained by vendors [Ohio Carbon, Graphtec], as tabulated in Table 4.

Table 4: 540 MW_t internal optical cavity receiver graphite costs

Receiver Graphite Component	Dimensions	Normalized Cost, 540 MW Receiver ($/kWt)
Graphite Pipe	2 cm OD, 1 cm ID, 1 m length	0.0002
Graphtek Plenum	Ring, 20"	0.004
Connecting Pipes	21,751 m	4.4
Receiver Module Pipes	23,550 m	48.3
Receiver Module Plenums	8,294	18.5
Total		71.3

Secondary Concentrators

The secondary concentrator was modeled as a hexagonal prism, where the hexagon through which light entering from the heliostat field was five times greater than the area of the hexagon through which light exited into the receiver. Thus, if light were to enter the concentrator at a concentration of 1 MW/m^2 (1,000 suns), it would exit the concentrator at the target concentration of 5 MW/m^2 (5,000 suns). The diameter of the entrance to the CPC was calculated as a 0.5 m diameter (module diameter) hexagon

because hexagons tessellate around the circumferential area of the receiver forming a lattice without gaps, thus concentrating all incident light into the receiver modules. Hexagons, also offer a closer approximation to a circle, as opposed to other geometries, such as rectangular geometries, which could also form a lattice without gaps. The length of the concentrator was dependent on the maximum acceptance angle, which was the maximum angle at which light could enter without being lost [63]. Knowing the concentration ratio, C, the maximum acceptance angle, θ was calculated using:

$$C = \frac{1}{\sin^2(\theta)} \tag{9}$$

With C=5, θ was 26.6° and the size of each trapezoidal mirror that made up the hexagonal concentrator was 0.11 x 0.25 x 0.3 meters.

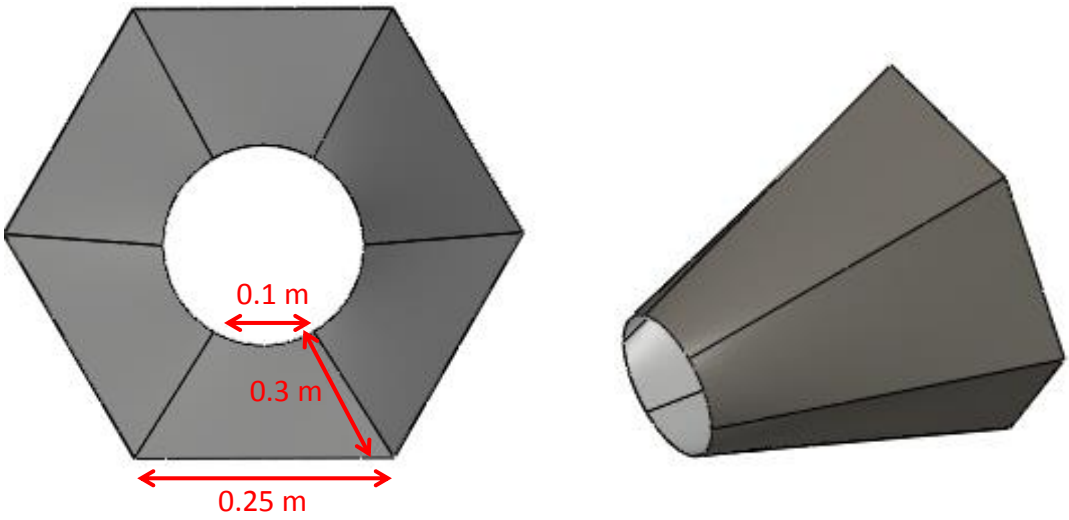

Fig. 16: Secondary concentrator

An upper bounding estimate for the secondary concentrator was taken from the heliostat mirror cost: \$180/m^2, which included much more than just the cost of the mirrors. Each individual mirror was 0.06 m^2 and there were 6 mirrors in each concentrator with 4,147 concentrators in the receiver giving a total mirrored area of 1,456

m^2. Multiplying by the mirror cost per m^2, the cost of the secondary concentrators was \$262,000 or \$0.5/kWh_t, which was 0.6% of the total receiver cost. Since this cost was not dominant in the receiver cost, the secondary concentrators were likely to be purely performance driven, as each imperfect reflection reduced the heat that can be captured. The mirror cost estimate, \$180/m^2 was already conservative, because that price included heliostat foundations, structures, and tracking motors that were not relevant for a secondary concentrator. The actual heliostat mirrors were likely closer to \$20/m^2 with a reflectivity of approximately 90% [64]. Using higher quality optics for higher reflectivity would improve efficiency, but was not likely to drive the receiver costs higher. Even if the finish on the CPC mirrors resulted in a cost an order of magnitude higher than the heliostat mirrors, i.e. ~\$1,000/m^2, the secondary concentrators would have been only ~3% of the receiver cost.

Receiver Insulation

Insulation needed to be packed around the receiver modules and graphite pipes to prevent heat leakages. The insulation was modeled as a cylindrical ring that surrounded and encompassed all the receiver modules.

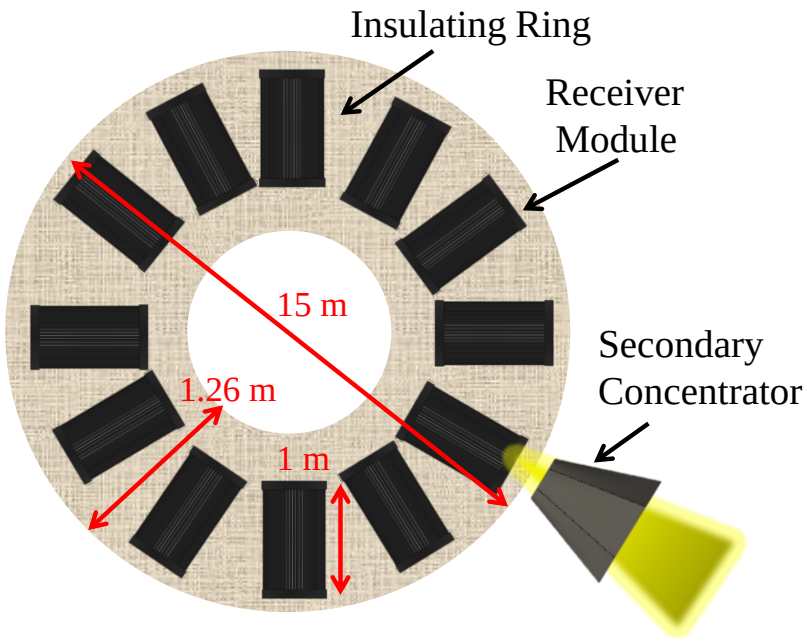

Fig. 17: Top down review of receiver insulating ring. In reality, the insulation in front of the receiver modules would have been cut out to let light through. For cost modeling, the insulation was modeled as a cylindrical shell with the dimensions shown and 18 meters tall

In order to estimate the volume of insulation necessary, the thickness required was calculated by determining how heat is conducted throughout the receiver. For the nominal design, there were 4,147 receiver modules and the receiver peak output was 540 MW_t. Thus, each receiver module output ~130 kW of heat. From numerical heat transfer calculations performed using COMSOL on a cavity receiver module, achieving 90% overall efficiency required that the modules leak $\leq$ 5% of their energy, or 6 kW, via conduction through insulation [52]. The heat loss rate, Q_{loss} =6 kW, was then input into the steady state heat Eq. for a cylindrical shell to calculate the required insulation thickness, r_i (Eq. 10).

$$Q_{loss} = \frac{2\pi Lk(T_{rec} - T_{env})}{\ln(r_i / r_o)} \tag{10}$$

where k was thermal conductivity, L was cylinder length, T_{rec} was receiver temperature, T_{env} was environment temperature, r_i was inner radius and r_o was outer radius. The insulation used in the estimate was Zircar Alumina Mat with a maximum use temperature of 1,650°C and thermal conductivity equal to k= 0.3 W/m-K at 1,400°C [65]. Each receiver module was approximated as a cylinder with 0.25m radius, r_o, and 1 m length, L which had a resultant insulation thickness of 0.13 m. In reality, the insulation thermal conductivity was even lower at lower temperatures, but as a conservative estimate, it was taken as the peak value at the peak temperature: 1,400C.

For a full scale receiver, the insulation would have been packed in between receiver modules and 0.1 m in front and behind the modules, effectively forming a shell around the receiver. To calculate the total volume of insulation required, the volume of a cylindrical ring 0.13 m wider than the receiver modules was calculated. This ring had an outer diameter of 15 m, a height of 18 m, and a thickness of 1.26 m (Fig. 17). This gave an insulated ring around the modules a volume of 550 m^3. At \$7,958/m^3, the insulation added \$4.3M or \$7.96/kWh_t to the receiver cost.

Receiver Nitrogen Containment

The receiver was primarily made of carbon and had Sn(l) flowing through it; therefore, the receiver needed to be kept in a nitrogen environment to protect against oxidation. Because modeling the nitrogen containment seals was beyond the scope of the model, the estimated cost of the nitrogen containment was modeled as a steel tank surrounding the graphite receiver modules (Fig. 13). The steel containment had large windows cut out containing a dense array of secondary concentrators to further concentrate the sunlight. The nitrogen containment vessel cost was estimated using the

formula for pricing a steel tank to contain LS, which was developed in the NREL study [66]. The study asked industry professionals to establish the base cost for CSP TES components. One of these TES components was a mild carbon steel tank used to hold LS at 290°C. The tank was modeled to hold enough LS for 6 hours of energy storage for a 280MW_t power block cycled between 565°C and 290°C and was approximated by a cylinder 22 m in diameter and 22 m tall that was \$2.18M or \$4.04/kWh_t. The rationale for comparing the steel tank and receiver nitrogen containment was that both are steel tanks designed to prevent fluid penetration. Furthermore, the receiver nitrogen containment tank was heavily insulated from the receiver and was therefore expected to operate at temperatures below 290°C where mild carbon steel could be safely used.

To estimate the price of the N_2 containment tank for the receiver, the LS storage tank price was scaled down to the receiver size. The receiver had a cylindrical footprint 16 m in diameter by 18 m high. The price of the tank scaled with the volume raised to a scaling factor. In the chemical processing industry, for cylindrical storage tanks this factor was 0.7 [66]:

$$R_c = \frac{Base\ Cost}{\left(V_B / V_R\right)^{0.7}} \tag{11}$$

where R_c was the cost of the receiver nitrogen containment tank, V_B was the base tank volume, and V_R was the volume of the receiver. Using this formula, the cost of the receiver nitrogen containment was \$1.25M or \$2.2/kWh_t**.** This cost was added to the receiver cost and had no direct cost comparison with the LS-CSP plant because LS receivers did not require nitrogen containment.

Receiver Construction Costs

Construction costs for the internal receiver design were estimated based on construction costs for the external LS receiver. Based assumptions were validated by discussions with Solar Reserve LLC representatives, and the receiver cost was estimated at \$30M or \$55/kW_t including construction costs, but excluding the initial design costs. The proportion of costs due to construction were not given but could be conservatively estimated by subtracting the cost of high nickel content alloy pipe from the receiver, which is the most prominent material cost. High nickel content alloys were typically 4X's as expensive as stainless steel [66] and from one vendor [MSC direct], a 0.5" OD stainless steel pipe had a cost of \$12/foot and applying the nickel alloy 4X cost factor put the receiver pipe price at \$48/foot. To cover the cylindrical surface of the external receiver with vertical, 0.5" pipe required 233,000 feet of pipe for a total of 11.2 M\$. Subtracting pipe cost from the receiver cost gave the construction cost, \$18.7M or \$34/kW_t. In reality, the external receiver construction cost was likely lower than estimated because of additional materials costs like headers, internal structure, and insulation. More research into construction costs is necessary for the graphite internal optical cavity receiver design, but for this nominal design, \$34/kW_t was used.

Receiver Total Costs

The costs of the different internal receiver components are given in Table 5:

Table 5: Receiver component costs

Receiver Component	Cost M$	Normalized Thermal Cost ($/kW$_t$)	Normalized Electric Cost ($/kW$_e$)
Graphite pipes and plenums	38.5	137	237
Insulation	4.3	8.0	26.7
Secondary Concentrator	0.3	0.6	1.9
Nitrogen Containment	1.2	2.2	7.5
Construction	18.7	67	117
Total	63.1	116	390

For comparison, the LS receiver had a cost of \$30M or \$55.5/kW$_t$. On a cost basis, the internal cavity receiver design was 110% more expensive. On a \$/kW$_e$ basis, the LM receiver was 31% more expensive than the LS receiver.

Receiver Pressure Losses

Pumping Sn(l) through all the connecting tubes and module tubes required a driving pressure. Pressure loss in the receiver tubes was calculated according to the following formula:

$$\Delta p = \frac{f \times L \times v^2}{2 \times g \times D} \tag{12}$$

where f was the graphite friction factor, L was the pipe length, V was the flow speed, g was the gravitational constant, and D was the inner diameter of the pipe [67].

For the nominal design, the friction factor for graphite pipes was 0.006 [68]. The pressure loss through the connecting pipes and module pipes were computed separately

since the flow speed differed. The flow through the 71 separate receiver pipes (Fig. 12) was in parallel, which reduced the pressure losses in the receiver.

Table 6: Receiver pressure losses

	Connecting Pipes	Receiver Module Pipes
Total Pipe Length (m)	21,751	235,550
Pipe Diameter, D (m)	0.01	0.01
Pipe Volumetric Flow rate V (cm3/s)	600	8.55
Flow Speed (m/s)	4.79	0.06
Δp (Pa)	12,041	25

The total pressure loss in the receiver was almost negligible at 12 kPa. The primary reason for the low pressure loss was the fact that the flow could be split into many parallel paths, minimizing the LM velocity. Extremely low flow rates were possible with Sn(l) because the high thermal conductivity (30 W/m-K), achieved a high convection coefficient even in the limit of laminar flow [44]. This property of LM was important to recognize, since it led to considerable cost savings as a result of a significantly lowered parasitic loss as compared to LS-CSP. To compare the differences in flow speed, take for example a 1 cm inner diameter pipe exposed to a 1 MW/m^2 solar heat flux (1,000X concentration from heliostat field). The maximum receiver wall temperature is a tradeoff between the required HTF flowrate to achieve the required convective heat transfer coefficient, and the receiver's re-radiation back to the environment. For this example, the temperature difference between the HTF and pipe wall is ~50°C, which requires a convective coefficient of 20,000 W/m^{2}K for the solar flux 1 MW/m^2. Laminar flow through a pipe with uniform heat flux has a constant Nusselt number of 4.364 [69]. Since Sn(l) has a thermal conductivity k = 30 W/mK, a 1 cm pipe yields a convective coefficient of 26,184 W/mK, which is sufficient to achieve a

50°C temperature difference between the fluid and pipe. By contrast, for a non-electrically conductive liquid, such as LS, high speed turbulent flow would be required to reach sufficiently high heat flows, due to its lower thermal conductivity (Table 7).

Table 7: Sn(l) vs. salt(l) transport properties [43, 44]

	Density (kg/m3)	Viscosity (cP)	Thermal Conductivity (W/m-K)	Specific Heat (J/kg-K)
Salt(l)	6,750	0.97	0.5	240
Sn(l)	1,899	3.26	30	1,495

Turbulent flow through the circular tube sections is determined using the Dittus-Boelter correlation:

$$Nu_D = \frac{hD}{k} = 0.023\left(\frac{\rho VD}{\mu}\right)^{0.8}\left(\frac{C_p\mu}{k}\right)^{0.4} \quad (13)$$

where ρ is density, V is fluid velocity, D is pipe diameter, μ is viscosity, C_p is specific heat, and k is thermal conductivity [69]. Using the Dittus Boelter correlation, assuming a convective coefficient of 20,000 W/m-K in a 1 cm pipe is required, yields a 10 m/s velocity for LS flow, but only a laminar Sn(l) flow speed of 1 m/s achieves the same convective coefficient. Since pressure loss in a pipe scales with fluid velocity squared, in this example, the LS flow experiences a 100X higher pressure drop as compared to the LM flow [67]. This advantage of LM over non-electrically conductive fluids is quantified in terms of cost later, where the pressure drop is converted to a parasitic electric loss in the Parasitic Loss section of chapter 7.

In summary, the most significant cost of the solar receiver sub system was the internal optical cavity receiver which comprised 48% of the total sub system cost. The solar receiver's expense comes largely from the 4,147 graphite modules required to cover

the area projected from the heliostat field. If the heliostat field is modified to achieve a higher concentration ratio, then the surface area of the receiver could be reduced requiring less receiver modules.

CHAPTER 5: THERMAL ENERGY STORAGE (TES)

Section Overview

The LM-CSP plant TES subsystem cost was normalized by the peak power output from the plant, K_s ($/kW$_e$), using the following expression:

$$K_s = \left(\frac{C}{\eta_E} \right) \times t \tag{14}$$

where C was the cost of the TES components in $/kWh$_t$, normalized to the thermal energy stored for the CSP plant (2,520 MWh), η_E was the power cycle efficiency, and t was the hours of storage. The LM-CSP subsystem consisted of 7 components, namely: tanks, storage media, the TES heat exchanger, inert atmosphere containment, inert atmosphere pipe conduits, piping/ support pumps, and controls/instrumentation. The design and cost estimation of each component is described in the forthcoming sections. The cost for LM controls/instrumentation and spare parts were taken as 2X's the cost of LS components for the same reason as in the receiver subsystem. The overall cost comparison for TES subsystem is shown in Table 8.

Table 8: Thermal energy subsystem

Thermal Energy Subsystem								
	LS-CSP				LM-CSP			
	Total M$	$/kWh$_t$	$/kWh$_e$	$/kW$_e$	Total (M$)	$/kWh$_t$	$/kWh$_e$	$/kW$_e$
Tanks	16.9	6.7	18.8	169.2	5.9	2.3	4.0	36.2
Fluid Media	30.2	12.0	33.7	303.0	8.8	3.5	6.1	54.5
Storage Fluid Heat Exchanger	0.0	0.0	0.0	0.0	6.8	2.7	4.7	42.3
Receiver Loop Fluid	0.0	0.0	0	0	2.7	1.1	1.9	16.7
Inert Atmosphere Conduits	0.0	0.0	0.0	0.0	0.1	0.0	0.1	0.7
Piping and Small Support Pumps	2.5	1.0	2.8	25.3	6.3	2.5	4.3	38.9
Controls and instrumentation	1.3	0.5	1.4	12.6	2.5	1.0	1.7	15.6
Spare Parts	2.5	1.0	2.8	25.3	5.0	2.0	3.5	31.2
Total Capital Cost	53.4	21.2	59.5	535.3	38.2	15.2	26.2	236.1

Thermal Storage Fluid

An optimal TES medium was both inexpensive and safe. Additional requirements were high energy density, low viscosity, high thermal conductivity, a high operating temperature range where it could be used, and chemical inertness with respect to its containment material. Different storage media could be directly compared by calculating their cost per unit of electrical energy stored, C_s, by using Eq. 15 below:

$$C_s = \frac{M}{\left(\int_{T_{cold}}^{T_{hot}} C_p(T)\, dT \right) \eta} \tag{15}$$

where M was the mass normalized material cost, $C_p(T)$ was the temperature dependent specific heat, and η was the maximum power cycle efficiency available for a given storage medium. The specific heat for each material was integrated from the storage low temperature, T_{cold} to the storage hot temperature, T_{hot} , as Fig. 18 shows the different fluids that were considered.

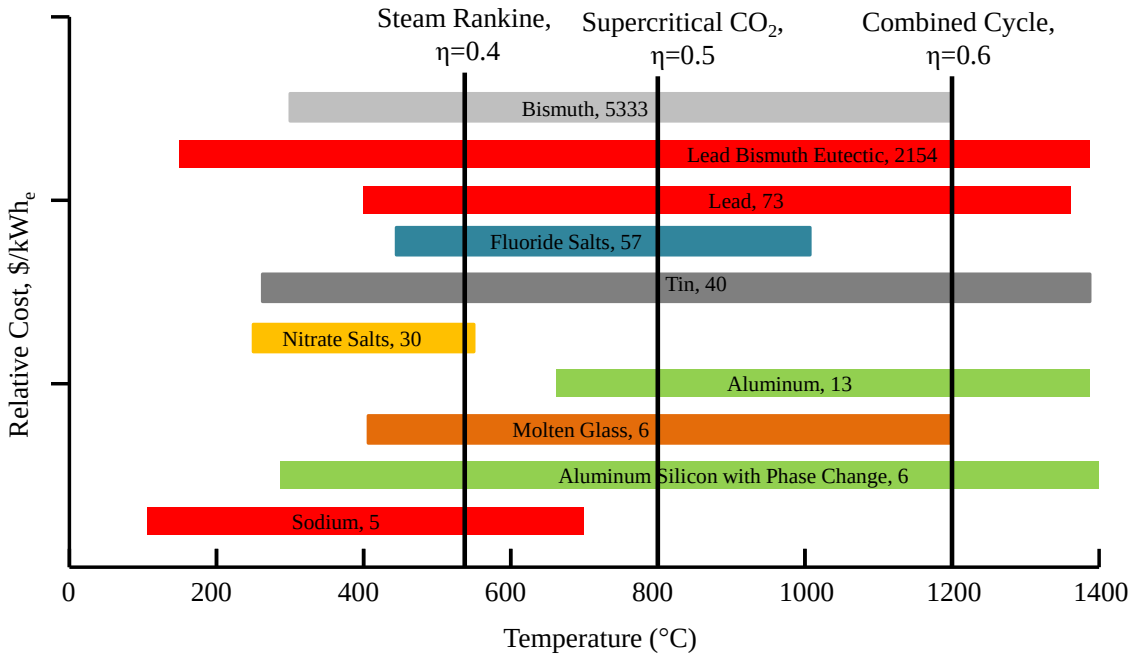

Fig. 18: Thermal storage fluids under research are plotted over the proposed temperature range at which they would be used. Fluids are organized vertically from least expensive to most expensive. Example power cycles and their efficiencies are shown as a vertical line for the cycle peak temperature input as a reference [43, 50, 70, 71]

Liquid glass was eliminated due to the lack of commercial products and their high viscosity, which inhibited pumping [71]. Liquid sodium, while inexpensive, was highly reactive with air and violently reactive with water and was eliminated for safety considerations [72]. Al(l) was an optimum storage fluid due to its low cost and high temperature (>1,400°C) stability. Al's(l) storage temperature range was further improved by devising a system that extracted heat from freezing the Al(l) and storing it as solid. The storage fluid cost formula was adjusted for a frozen medium by adding the latent heat of fusion to the denominator, h_f:

$$C_s = \frac{M}{\left(\int_{T_{cold}}^{T_{hot}} C_p(T)\,dT + h_f \right) \eta} \tag{16}$$

Adding 30 at% Si to the melt significantly increased the liquid's heat of fusion, which led to even lower storage costs. However, it raised the melt's liquidus point from 660°C to 822°C which required a more complex heat exchanger system to handle two phases [73]. Silicon's heat of fusion was anomalously large at 1.81 MJ/kg, which was 3 times that of water [73].

Table 9 compares the fluid properties used to calculate storage medium costs for LS, Al(l), and Al-Si with solidification. The costs and temperature range for all three fluids are plotted in Fig. 18 and switching to Al-Si(l) reduced storage fluid costs by 6X over current nitrate salts. The fluid storage cost on a thermal basis, C_t ($/kWh$_t$), was added to Eq. 14 and tabulated for the TES subsystem in Table 8.

Table 9: Thermal storage fluid cost comparison

Property	Nitrate Salt(l)	Al(l)	70% Al- 30% Si
M ($/kg)	1.23[66]	1.69[41]	1.95[73]
T_m (°C)	220 [43]	660	822
T_{cold} (°C)	290	690	290
T_{hot} (°C)	565	1380	1380
Average C_p (kJ/kg-K)	1.5	1.2	1.1
h_f (kJ/kg)	0 (does not freeze)	0 (does not freeze)	821
$\int_{T_{cold}}^{T_{hot}} C_p(T)\,dT + h_f$ (kJ/kg)	411	798	1975
C_t ($/kWh$_t$)	12	7.89	3.53
H	0.4	0.6	0.6
C_s ($/kWh$_e$)	30.10	13.13	5.89

In addition to being a cheaper alternative than Al(l), Al-Si(l) was compatible with SiC and ALII castable cement, which were the proposed refractories for the TES subsystem. Therefore, the rest of the TES economic analysis was performed considering an Al-Si(l) melt.

Al-Si(l) reacted with graphite and could not be used in the receiver so the cost of a separate closed loop of Sn(l) was calculated. The empty volume of the receiver pipes was 32 m^3 and the empty volume of the tower pipes was 14 m^3. Sn was \$8.4/kg and had density 6750 kg/m^3 resulting in a volumetric cost of \$57,000/m^3 [50]. Multiplying the volumetric cost by the requisite volume of 47 m^3, the cost of Sn was approximately \$2.7M, or \$1.1/kWh_t.

Using a separate fluid, Sn, for the receiver loop was an additional cost not present in a LS-CSP plant, and although expensive, the total receiver and TES fluid cost for LM-CSP was still less expensive than LS-CSP. Combining Al-Si(l) costs with Sn(l) costs and normalizing them to electrical energy stored gave \$7.9/kWh_e, which was 1/3 the normalized cost of LS.

2-Phase Energy Storage

By using the Al-Si alloy from 1380°C to 250°C, thermal energy was stored in three phases: 1) sensible heat storage in the solid melt (250-577ºC), 2) latent heat storage during phase transition (577-822 ºC), 3) sensible heat storage in the liquid melt (822-1380 ºC). Assuming a 30 at% Al-Si alloy was used, it was an off-eutectic alloy point and therefore, latent storage occurred over the liquidus temperature range from 822°C to 577°C (Fig. 19).

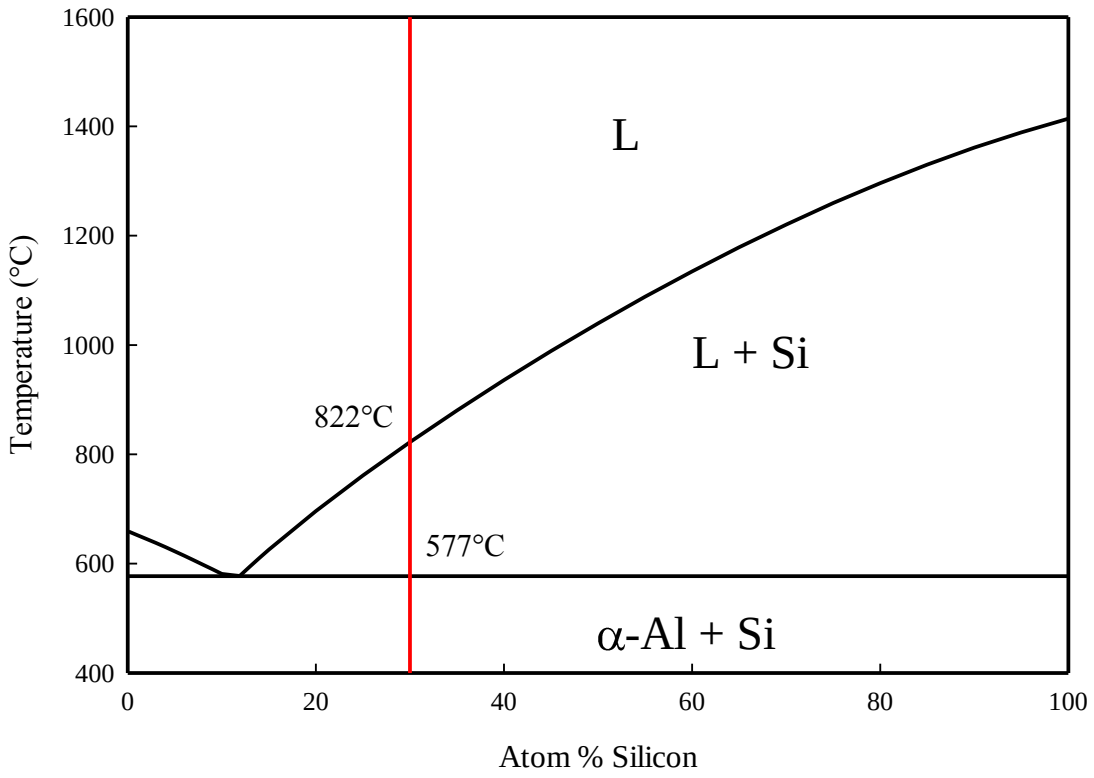

Fig. 19: Al-Si phase diagram. The alloy chosen for TES is shown as the vertical red line, 30 atom % Si. Latent heat storage occurred in the temperature range 577°C to 822°C [73]

Table 10 shows a tabulated list of each storage phase and its contribution to overall thermal energy stored. For simplicity, all latent heat was assumed to be extracted at the liquidus temperature, 822°C while in reality, solid Si precipitated out of the melt starting at 822°C, decreasing the remaining liquid's Si concentration as its temperature decreased to the eutectic temperature, 577°C, when the remaining alloy homogenously solidified altogether. Sensible solid storage was modeled from the liquidus curve, 822°C to the lower bound temperature, 290°C. This simplification was justified in the overall systems analysis because a single heat exchanger handled the entire solid and two-phase melt regime. Only the difference in states for the heat exchanger was required with the inlet a fully solid state at 250°C and outlet a fully liquid state at 822°C. If further exergetic

analysis is to be conducted with the Al-Si melt, then the latent energy stored needs to be expressed as a function of temperature, which was beyond this analysis.

Table 10: Al-Si melt storage phases

	Low Temperature (ºC)	High Temperature (ºC)	% Energy Stored
Sensible Solid Storage	290	822.3	30.2
Latent Storage	822.3	822.3	40.7
Sensible Liquid Storage	822.3	1380	27.8

The fraction of energy stored for sensible phases was calculated as follows:

$$F = \frac{C_{p,average} \times \Delta T \times M}{E} \tag{17}$$

where F was the fraction of energy stored in that phase, $C_{p\ average}$ was the average specific heat of the melt for the temperature range, M was mass of storage melt, ΔT was the temperature difference for that phase, and E was the total energy stored in the melt over all three phases. Eq. 18 was modified for latent heat storage:

$$F = \frac{h_{fusion} \times M}{E} \tag{18}$$

where h_{fusion}, was the latent heat of fusion of the melt.

TES Tanks

The Al-Si(l) for TES was held in a cylindrical tank constructed from a castable cement that was chemically compatible with the Al-Si melt, helped insulate the melt from thermal loss, and decreased the temperature from 1,350°C to 450°C so steel could be

used as a mechanical support (Fig. 20) [74]. An alternate design was to use a brick and mortar structure instead of castable cement that consisted of a single layer of high alumina brick lining the inner wall of a mullite brick tank. The alumina bricks were non-reactive with the melt; however, they were prohibitively expensive to use throughout the entire tank. Therefore, mullite made up the bulk of the thickness of the wall not in contact with the melt while mortar between the alumina bricks was used to seal against Al-Si(l) penetration. No mortars were found that would bond the alumina bricks while also resisting chemical corrosion from the melt. Therefore, the tank analysis focused on using castable cement, which was an experimentally proven material for contact with Al(l).

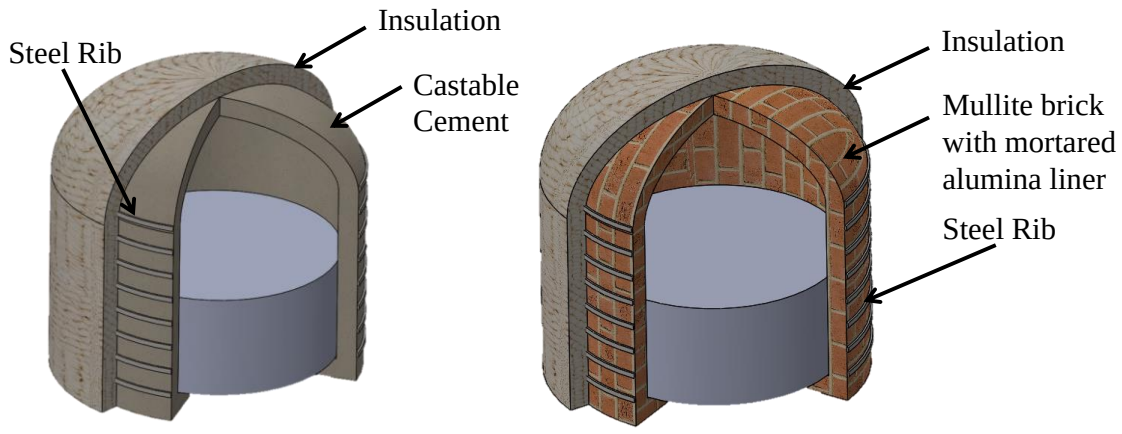

Fig. 20: Al-Si(l) storage tank options

The first step in modeling the cost of the Al-Si(l) storage tank was determining its size and the cement wall thickness for 9 hours of TES with a heat input to the turbines of 280 MW_t: 2,520 MWh_t. From Table 9, the Al-Si(l) melt had an energy density of 1,975 kJ/kg and mass density 2,433 kg/m^3. The energy density per unit mass was multiplied by the melt density, ρ=2,433 kg/m^3, to obtain a volumetric energy density of 4.8 GJ/m^3. The necessary volume was then calculated by dividing the total energy required by the melt volumetric energy density which yielded a tank volume of 2,083 m^3. By comparison, LS

had a volumetric energy density of 0.8 MJ/m^3 and required 12,860 m^3 to store the same amount of energy or 6 times the volume. The tank cylinder diameter and height were set equal to each other in order to minimize the surface area to volume ratio and thus reduce heat loss. Thus, in the case of the 2,083 m^3 LM tank, the diameter and height was only be 13.9 m. This factor of 6X increase in energy density was the primary reason the TES subsystem cost was lower for the LM-CSP plant vs. the LS-CSP plant.

The castable cement used for the tank wall was ALII from Westmoreland Advanced Materials, which was a calcium aluminate, designed for secondary Al processing to resist corundum growth and minimize kiln heat loss [74]. The cement properties are displayed in Table 12 and discussions with Westmoreland confirmed that 10 meter long steel walls with half meter thick cement liners have been commercially built with a cost of $5,950/$m^3$ [75]. Experimental tests were conducted by Westmoreland Inc., where they submerged ALII samples in Al(l) at 1,200°C for 800 hours and confirmed the cement's non-reactivity with Al(l) (Fig. 21). Additional tests with Al-Si at 1350°C were performed by collaborators at the Georgia Institute of Technology. The thickness of the sample was measured before and after contacting the melt for trials of 200 and 400 hours where thickness reduction indicated corrosion by the melt (Table 11).

Table 11: Castable cement samples in Al-Si melt

Cement	Test duration hr.	Coupon No.	Thickness, mm		Thickness loss µm
			Before test	After test	
AL II	200	1	2.959	2.956	3 ± 1
		2	3.073	3.068	5 ± 1
		3	3.202	3.198	4 ± 1
	400	4	3.065	3.059	6 ± 1
		5	2.867	2.858	9 ± 1
		6	2.753	2.749	4 ± 1

Extrapolating the worst corrosion scenario over the 30 year plant lifetime (9 micron thickness reduction over 400 hours), led to a worst case prediction that only ~ 6 mm of the liner would be corroded, which was an inconsequential amount.

Table 12: Westmoreland ALII castable cement properties

WAM AL II Cement	
Major Constituents	64.8 wt.% Al2O3, 24.3 wt.% CaO
Thermal Conductivity	0.7 W/m-K @1200°C
Cold Crushing Strength	4610 psi @1300°C
Permanent Linear Change	-0.3% @1300°C
Cost	$5950/m^3

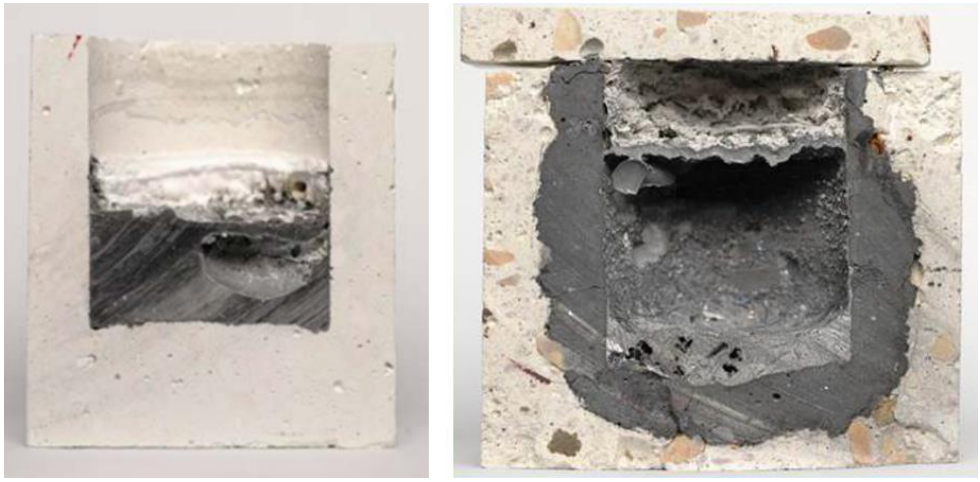

Fig. 21: Castable cement cup cross sections exposed to Al(l) at 1200°C for 120 hours. Left is WAM ALII, right is standard castable cement, WAM 45 SC. The ALII with <0.4% silica experienced no degradation. The 45 SC with 48% silica was penetrated. [75]

With the behavior of the cement experimentally verified, the required wall thickness of a storage tank and corresponding cost was calculated. A thicker wall led to less heat leakage; however, it was more expensive. The temperature boundary conditions for the cement wall were 1,350°C on the inside surface contacting the melt and 450°C on the outside surface where structural steel ribs were placed. To calculate the necessary wall thickness, the thermal resistance of a cylindrical shell was used:

$$q_r = \frac{2\pi Lk(T_{Al-Si} - T_{steel})}{\ln(r_i/r_o)} \quad (19)$$

where q_r was the heat loss through the cylindrical wall, L was the height of the tank, k was the cement thermal conductivity, $T_{Al\text{-}Si}$ was the temperature of the melt, T_{steel} was the temperature of the steel, r_i was the tank inner radius, and r_o was the tank outer radius. Heat loss through the cylindrical wall, q_r, was set to 1% of the thermal energy stored in the tanks per day, which was equivalent to1 MW_t continuous heat leakage. Solving for the outer liner radius, r_o = 7.35 m, which gave a tank wall thickness of 0.38 m and the total hot tank material had a cost \$1.38M or \$0.5/kWh_t.

The thickness of insulation surrounding the tank was also calculated using Eq. 19. Inexpensive fiberglass insulation was used because it had a maximum temperature limitation of 540°C, which was high enough to accommodate the 450°C temperatures present at the cement-steel interface. The fiberglass was \$52/m^3 and had a thermal conductivity of 0.2 W/m-K [76]. Solving Eq. 19 with constant temperature boundary conditions of 450°C and 25°C, the shell insulation layer was only 4 cm thick and was ~\$20,000 (\$0.008/kWh_t), a negligible cost in the thermal storage tank system.

Construction costs for the hot tank were estimated by scaling the base construction costs for LS-CSP tanks provided by an NREL report on two tank TES to the smaller volume of the LM-CSP tanks [66]. Base tank construction costs were \$2.62/kWh_t and the volume ratio exponent was 0.7 (11). Since the LM tank was 1/6 the volume of the LS tank, the construction costs were scaled by $(1/6)^{0.7}$ or 0.28, giving a construction cost of \$0.74/kWh_t. The construction cost was nearly the same as the material cost for the LM tank.

A second tank with the same volume was required to hold the frozen melt at 290°C. The same thermal analysis as the hot tank was performed to calculate costs. However, the allowable heat loss for the cold tank was reduced from 1% to 0.1% because the (s)Al-Si in the cold tank was 290°C instead of 1,380°C, and therefore a much smaller quantity of insulation was required to prohibit heat loss. Furthermore, the cold tank temperature was already below the steel tank support temperature limit so the castable cement lining prevented only chemical corrosion, and was not necessary to thermally insulate the steel supports like the 1380°C(l) Al-Si tank. These specifications required a thinner cement tank wall of 0.15 m and lower material cost of \$0.71M or \$0.3/kWh$_t$. Construction costs were estimated the same, \$0.74/kWh$_t$, for the cold tank as the hot tank since both were the same volume and design. Adding both tank costs together and normalizing with respect to thermal energy stored gave a cost of \$2.3/kWh$_t$. LS tanks made from stainless steel had a cost of \$6.7/kWh$_t$, which was 2.5X's as costly as their LM-CSP versions [10].

In reality, the tank cement liner may have to be thicker than calculated to provide a freeze plane for any leaks through cracks caused by thermal stress and fatigue. Eq. 20 provides a simplified estimation of the thermal conductivity of a cracked wall that is 0.25% Al by volume.

$$k_{cracked} = 0.0025 \times k_{Al} + 0.9975 \times k_{cement} \tag{20}$$

using an Al thermal conductivity of 200 W/m-K and cement thermal conductivity of 0.7 W/m-k, the estimated new wall thermal conductivity was 1 W/m-K, 42% more conductive than the unpenetrated wall. More significant cracking that led to Al

penetrating >0.25% of the tank volume would have had a more severe effect on tank wall thermal conductivity.

A greater effective tank wall thermal conductivity would have had a significant impact on tank performance. First of all, the heat leakage would be higher, decreasing the round trip efficiency of the storage tanks. Second, the cement insulation interface would have increased above the design point of 450°C and possibly higher than the Al-Si eutectic temperature, 577°C. If a crack penetrated the entire cement wall, penetrated Al would not freeze before exiting the cement wall and leak through the insulation as illustrated in Fig. 22. The tank on the left was the design presented in the economic analysis above where the cement-insulation layer was at 450°C, which put the freeze plane 85% of the way through the cement shell. The tank on the left was a more costly, but safer design, with a thicker cement layer that put the freeze plane only 60% of the way deep in the cement wall. If 0.25% of the cement wall volume was penetrated by Al(l), then the thin tank wall design would fail.

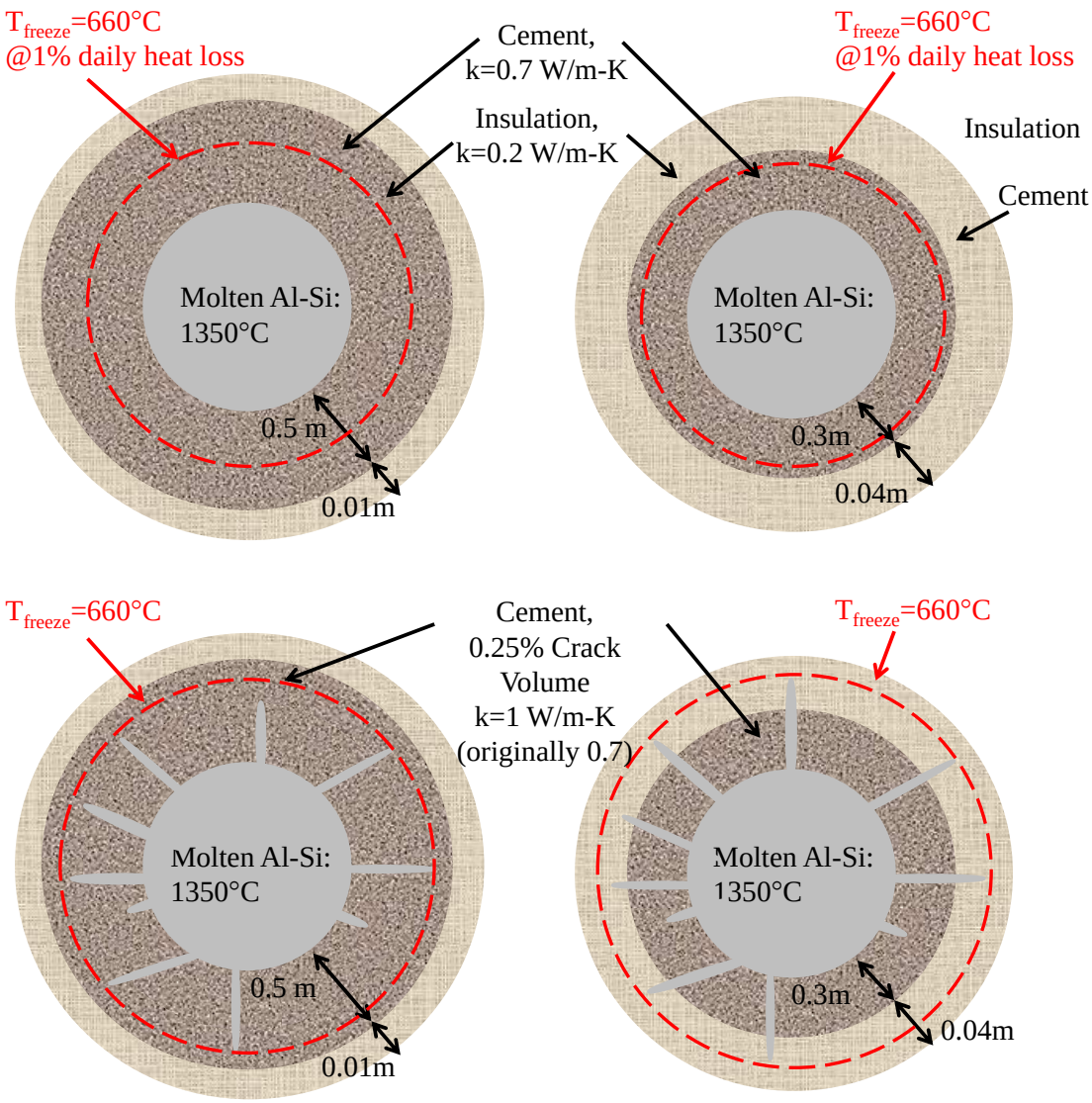

Fig. 22: Tank cross sections with different wall thickness. Top row is tank without cracks. Bottom row is if the wall cracks and 0.25% of wall volume is penetrated by Al(l).

Further prototype testing is needed to establish where the acceptable cost/risk tradeoff exists, based on testing the mechanical properties of the cement over long periods.

TES Pipes/Support Pumps

A cluster of mullite pipes carried Sn(l) from the tower to the TES heat exchanger situated by the storage tanks using LM pumps. These costs of the TES piping and support pumps were estimated using a 2.5X increased material factor calculated from costs of

similar size mullite and stainless steel pipes [61] [62]. The LS system pipes and support pumps were primarily stainless steel, thus a 2.5X cost factor was applied to the LS-CSP plant base cost given by Kolb [10]. Using this approach for the LM-CSP nominal design, the TES piping and support pumps were estimated to cost \$6.3M or \$2.5/kWh_t, which included construction costs since the base LS-CSP costs included construction costs. When normalized against LM-CSP electric output, the pipes and small pumps had a cost of \$39/kW_e, which was 56% more than the LS-CSP plant. These estimates were further justified by quotes obtained from vendors for modified versions of mechanical pumps that could be used to pump Sn(l) at $\leq$ 400C, and ceramic pumps used to pump LM at 1350C, which resulted in an approximately 2X increase in cost as compared to LS.

Nitrogen Containment Steel Conduit

The pipes carrying LM in the system required N_2 surrounding them in order to prevent oxidation. The primary cost of this nitrogen containment system was a 19" diameter steel pipe containment vessels that fit around the ceramic pipe bundles (Fig. 13). A steel tube 20' long and 24" in diameter was quoted at \$1,727/tube. It was estimated that 50 meters of pipe was needed to run to and from the TES system, in addition to 360 m of pipe to traverse the height of the tower for a combined total of 410 meters of steel containment pipe. This length gave a total cost of \$0.11M or \$0.05/kWh_t, which was a negligible cost in the system.

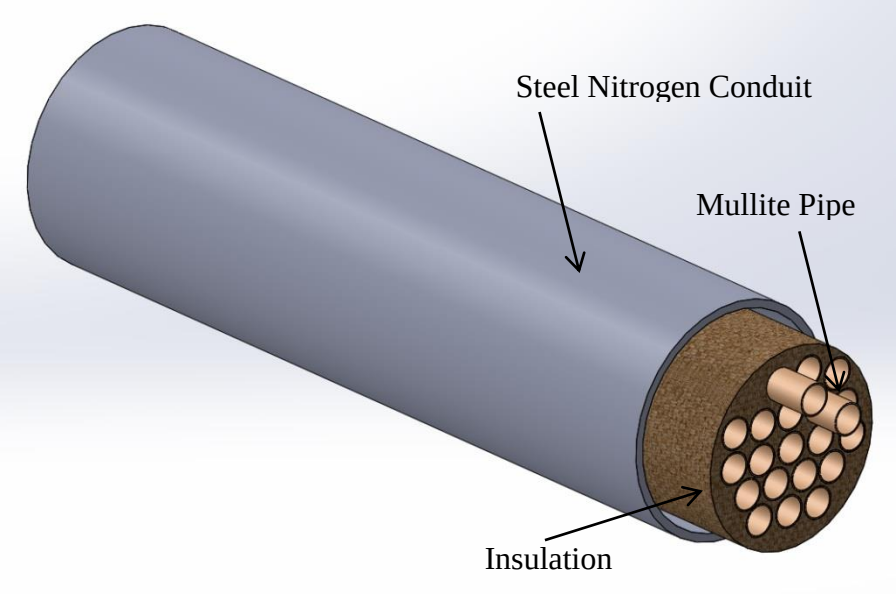

Fig. 23: Steel conduit nitrogen containment

Conclusion

Switching to LM storage led to significant cost reductions in the storage fluid and tanks category. For the same output electrical energy stored, the Al-Si(l) was 6X cheaper than LS and the tanks to contain it were 4X cheaper. The large temperature range and high latent heat capacity resulted in much smaller quantities of storage material required, thereby reducing tank size. This significant decrease in storage costs, drove the system optimization further towards the LM design.

The tradeoff associated with using lower cost Al-Si(l) was the need for a separate Sn(l) loop in the receiver. The additional heat exchangers were 20% of TES costs, and the Sn(l) cost was 7% of TES costs, which were two systems that were unnecessary in LS system where one fluid was used for both the storage and receiver. However, the combined cost ($16/kWh$_e$) of the storage fluid heat exchangers, fluid media, and receiver loop fluid still had a lower cost on a $/kWh$_e$ basis than LS ($34/kWh$_e$).

CHAPTER 6: HEAT EXCHANGERS

Charging the TES tanks required 4 different fluid phases: liquid tin (Sn), liquid Al-Si (Al-Si(l)), solid Al-Si (Al-Si(s)), and helium (He). Exchanging heat between all fluids required 3 different heat exchangers, which were envisioned as: 1) a liquid droplet heat exchanger (LDHX) between Al-Si(s) and He, 2) a LDHX between Sn(l) and Al-Si(l), 3) a shell and tube heat exchanger between Sn and He (Fig. 24). Discharging the TES tank heat to the power cycle required an additional 3 heat exchangers: 4) a shell and tube heat exchanger between Al-Si(l) and He, 5) a LDHX between (s) Al-Si and He, and 6) a printed circuit heat exchanger between He and SCO2 (Fig. 25). The shell and tube heat exchangers separated the two counter flowing fluids by pumping one fluid through the pipes and the other around the outside surfaces of the pipe array. They could handle high pressures and the solid wall of the pipe prevented fluid mixing or adverse reaction, provided the solid wall was simultaneously compatible with both fluids. The liquid droplet heat exchanger (LDHX) worked by showering a liquid or solid phase down a column while gas flowed upward, and exchanged heat via direct contact between the two immiscible fluid phases. LDHX required He gas since Al-Si(l) and Sn(l) would have reacted if mixed. Fig. 24 illustrates how the Al-Si TES tanks were thermally charged by Sn(l) from the receiver.

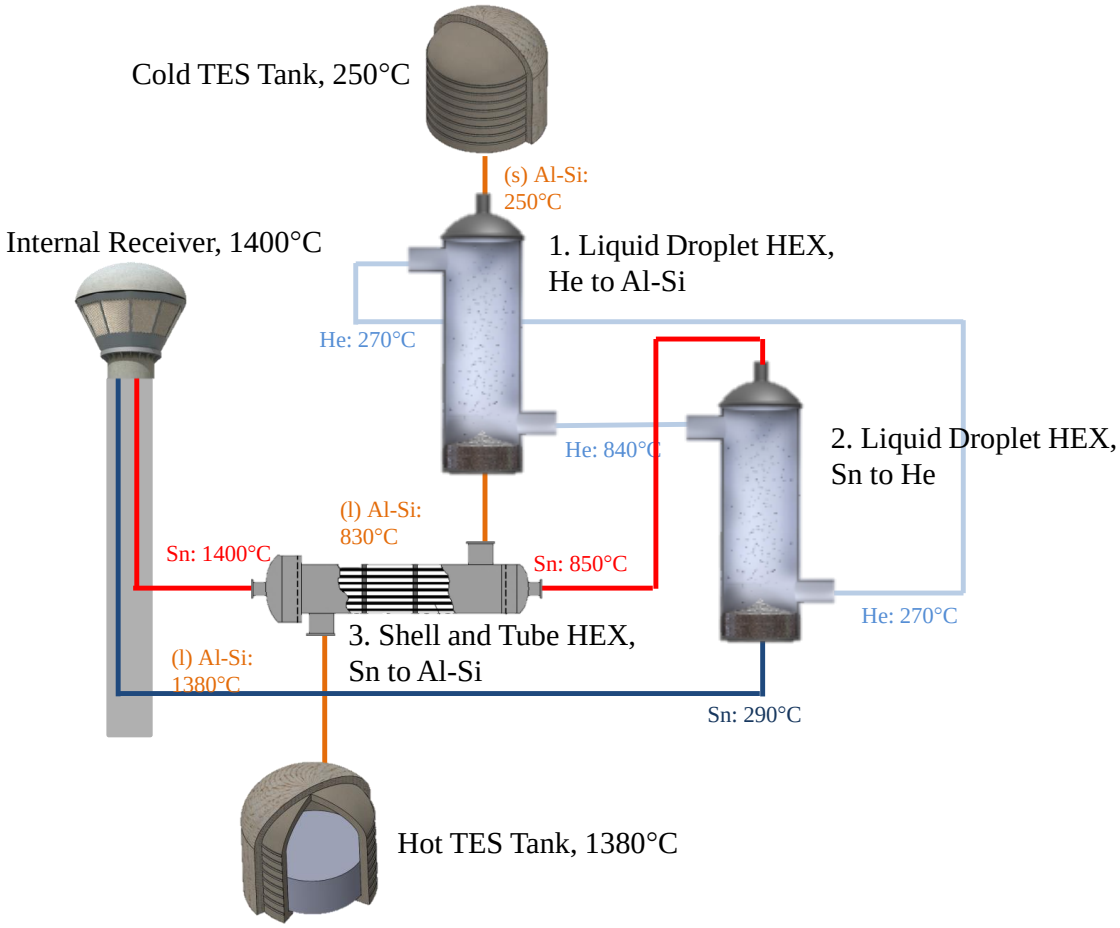

Fig. 24: Heat exchanger diagram for charging TES tanks

The envisioned power cycle was a combined cycle using a He Brayton cycle as the topping cycle and super critical CO_2 as the bottoming cycle. When electricity was required, Al-Si(l) at 1,380°C was pumped through the heat exchanger network to transfer heat to the combined cycle. Fig. 25 illustrates one proposed heat exchanger network to transfer heat to the power cycle. Printed circuit heat exchangers for super critical CO_2 cycles are being developed and their costs are generally included as part of the power cycle cost. Further thermodynamic analysis was necessary for the power cycle to reach or exceed an efficiency of 60% and that was beyond the scope of the present investigation. Nonetheless, the precedent set by the ability for natural gas combined

cycles to reach 60% efficiency was the rationale for assuming such a high efficiency may be possible for the LM-CSP system.

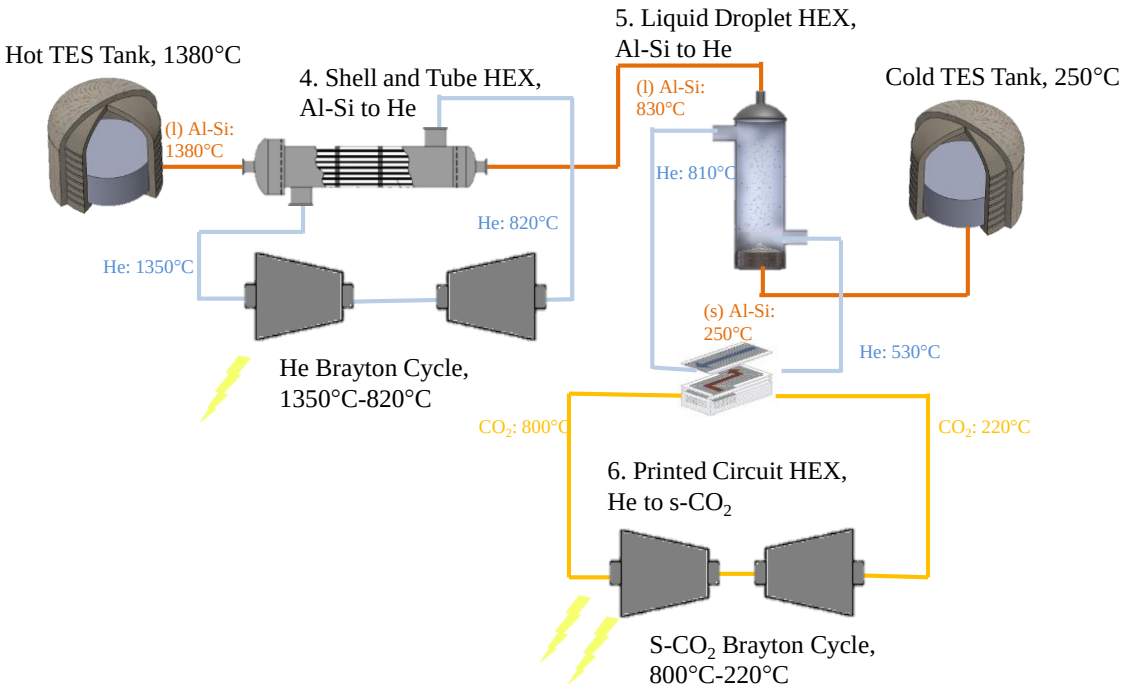

Fig. 25: Heat exchanger diagram for dis-charging TES tanks

All six heat exchangers were designed for the required power and their costs were modeled in detail. For charging the thermal storage tanks, the shell and tube heat exchanger was responsible for the sensible portion of the Al-Si(l) melt while the two LDHXs were responsible for the latent and sensible portion of the solidifying Al-Si. Therefore, the heat exchanger power was calculated by multiplying the maximum power input, 540 MW_t, by the proportion of power input each heat exchanger handled. Each fraction was determined by the proportion each Al-Si phase stored, tabulated in Table 13. For discharging, the power of each heat exchanger was a fraction of the peak power cycle thermal input: 280 MW_t. Again, each fraction was determined by the energy fraction stored in the Al-Si phases.

Table 13: Heat exchanger power and fluids

		Hot fluid (giving heat)				Cold Fluid (gaining heat)			
Heat Exchanger	Power (MW)	Media	Inlet Temp (°C)	Outlet Temp (°C)	Average Pressure (atm)	Media	Inlet Temp (°C)	Outlet Temp (°C)	Pressure (atm)
LDHX	382	He	840	270	1	(2 Phase) Al-Si	250	830	1
LDHX	382	Sn	850	290	40	He	270	840	1
Shell and Tube	158	Sn	1,400	850	50	(l) Al-Si	830	1,380	1
Shell and Tube	82	(l) Al-Si	1,380	830	1	He	820	1,350	10-30
LDHX	198	(2 Phase) Al-Si	830	250	1	He	240	810	1
Printed Circuit Board	198	He	810	240	1	S-CO_2	220	800	100

Shell and Tube Heat Exchanger Design

The cost of the shell and tube heat exchangers was determined by calculating the length of pipe necessary for a heat exchanger with a 95% effectiveness and then multiplying by the cost per unit length of that pipe. It was assumed that the two shell and tube heat exchangers would be made from Hexoloy SiC because SiC was chemically compatible with both Al-Si and Sn. In discussions with the manufacturer of Hexoloy SiC, Saint Gobain, SiC was currently used in high temperature heat exchangers and had a high thermal conductivity of 77 W/m-K at 400°C and 35 W/m-K at 1,200 °C which allows for efficient heat exchange [47]. Finally, SiC remains chemically stable above 1,350°C and has a similar CTE (4.0×10^{-6} K^{-1}) to the rest of the Sn compatible

infrastructure (i.e. mullite and graphite CTE ~ 6.0x 10^{-6} K^{-1}). Based on a quote obtained from Saint Gobain, a 14 mm OD SiC tube with 11 mm ID is $70/m [47].

The shell and tube heat exchanger analysis was conducted using the Effectiveness-NTU method and an iterative design approach to achieve the desired performance [77]. A heat exchanger configuration was assumed, detailing the number of pipes, sizes, baffles, etc. Then, the outlet temperatures and heat transfer rate were calculated for the assumed configuration and the configuration was adjusted until the resultant outlet temperatures and heat transfer rate matched the desired values presented in Table 13. The final cost was then estimated by multiplying the resultant total pipe length by the SiC pipe cost provided by Saint Gobain ($70/m).

The number of transfer units, or NTU was first calculated:

$$NTU = \frac{UA}{C_{\min}} \tag{21}$$

where U was the conductance between fluids, A was the pipe surface area for all tubes, and C_{min} was the lowest heat capacity rate of the two fluids. The heat capacity rate for a fluid was calculated by multiplying the flow rate, $\dot{m}$ by the heat capacity, C_p:

$$C = \dot{m}C_p \tag{22}$$

As a starting point for the design, the heat capacity rates for both fluids were set equal to each other, so that the results were consistent with the LM-CSP plant size being modeled. In all the shell and tube heat exchangers required, both fluids experienced the same heat transfer rate and identical temperature differences (Table 13). Setting ΔT and q equal for both fluids, it was apparent that C must be equal for both fluids, and the heat capacity rate ratio, C_r was equal to 1.

$$q_h = C_h \times \Delta T_h \tag{23}$$

$$q_c = C_c \times \Delta T_c \tag{24}$$

$$C_r = \frac{C_c}{C_h} \tag{25}$$

The next step in the analysis was calculating the heat exchanger effectiveness, ε, as a function of NTU and C_r. For C_r=1, ε is given by:

$$\varepsilon = \frac{NTU}{1 + NTU} \tag{26}$$

The heat transfer rate for the chosen exchanger configuration was then calculated:

$$q = \varepsilon C \left(T_{h,i} - T_{c,i} \right) \tag{27}$$

where $T_{h,i}$ and $T_{c,i}$ were the inlet temperatures for the hot fluid and cold fluid respectively. The heat exchanger geometry (i.e., number of tubes, length of tubes, baffles, and baffle spacing) was iteratively modified until the calculated q matched the desired heat transfer rate from Table 13.

The heat exchanger configuration and convective coefficients were calculated using the Kern method for shell and tube heat exchangers [78]. The shell side convection was a function of many parameters as detailed in Table 14 and illustrated in Fig. 26.

Table 14: Shell and tube heat EX configuration variables for Kern Method

Description	Variable	Units	Resultant Value for HX#3, Sn to Al-Si	Resultant Value for HX#4, Al-Si to He
Shell internal Diameter	D_s	m	0.54	1.27
Tube Outside Diameter	D_o	mm	14	14
Tube Pitch	P_T	mm	16	16
Number of tubes	N_T	-	1024	5776
Baffle Spacing	L_B	m	1	4
Pipe/shell Length	L_s	m	15	20
Baffle Thickness	t_b	mm	5	5
Number of Baffles	N_B		14	4
Cost		M$	1.07	8.09
Normalized Cost		$/kW$_e$	11.3	164

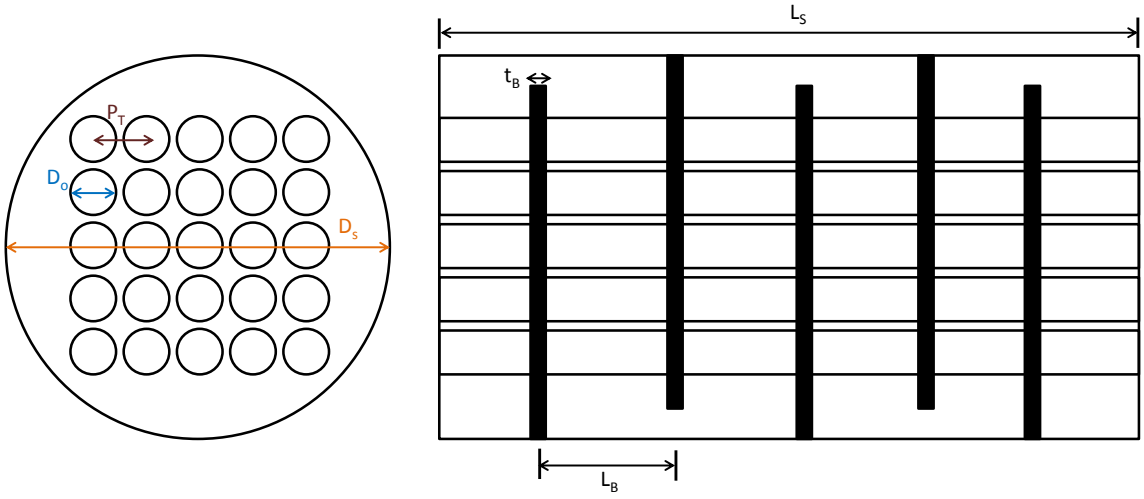

Fig. 26: Cross sectional front and side view of shell and tube heat exchanger.

Calculating the shell side fluid convection required calculating other constituent quantities first. First, the cross flow shell area, S_s, was calculated:

$$S_s = \frac{D_S \left(P_T - D_o\right) L_B}{P_T} \tag{28}$$

Then the effective flow diameter, D_e, was determined:

$$D_e = \frac{4\left(P_T^2 - \pi D_o^2/4\right)}{\pi D_o} \tag{29}$$

The mass flow rate per area, G_s, was given by:

$$G_s = \frac{\dot{m}}{S_s} \tag{30}$$

Then the Reynold's number was calculated using the fluid temperature average viscosity, μ_f:

$$\mathrm{Re} = \frac{D_e G_s}{\mu_f} \tag{31}$$

Finally, the shell side convection, h_{outer}, was calculated, using:

$$h_{outer} = 0.36\left(\frac{k}{D_e}\right)\mathrm{Re}^{0.55}\,\mathrm{Pr}^{0.33}\left(\frac{\mu_c}{\mu_h}\right)^{0.14} \tag{32}$$

where *Pr* was the Prandtl number, and μ_c and μ_h were the fluid cold side and hot side dynamic viscosities respectively.

The convection on the inside of the tube was a function of the Nusselt number and the Nusselt number for LM in smooth pipes with uniform heat flux was approximated by Skupinski [77] as:

$$Nu_D = 4.82 + 0.0185\left(\mathrm{Re}_D\,\mathrm{Pr}\right)^{0.827} \tag{33}$$

$$h_{inner} = \frac{Nu \times k}{D} \tag{34}$$

Conduction through the SiC pipe wall added thermal resistance to the system. This resistance was calculated using steady state conduction Eq. with cylindrical resistance:

$$R_{wall} = \frac{\ln\left(r_o / r_i\right)}{2\pi kL} \tag{35}$$

where r_o and r_i were the pipe outer and inner radii, respectively, L was pipe length and k was the thermal conductivity of the pipe. For Hexoloy SiC at 1,200°C, the thermal conductivity was k =36 W/m-k [47], which was much lower than the value at lower temperatures, thus leading to a conservative estimate (oversizing of the HXs). The conductance of the heat exchanger, U, was then calculated and the conductance between the fluids was found by summing three individual resistances in series: convection between the tube fluid, conduction through the SiC pipe wall, and convection between the shell fluids. Fig. 27 gives an example of these resistances for the Sn to Al-Si heat exchanger.

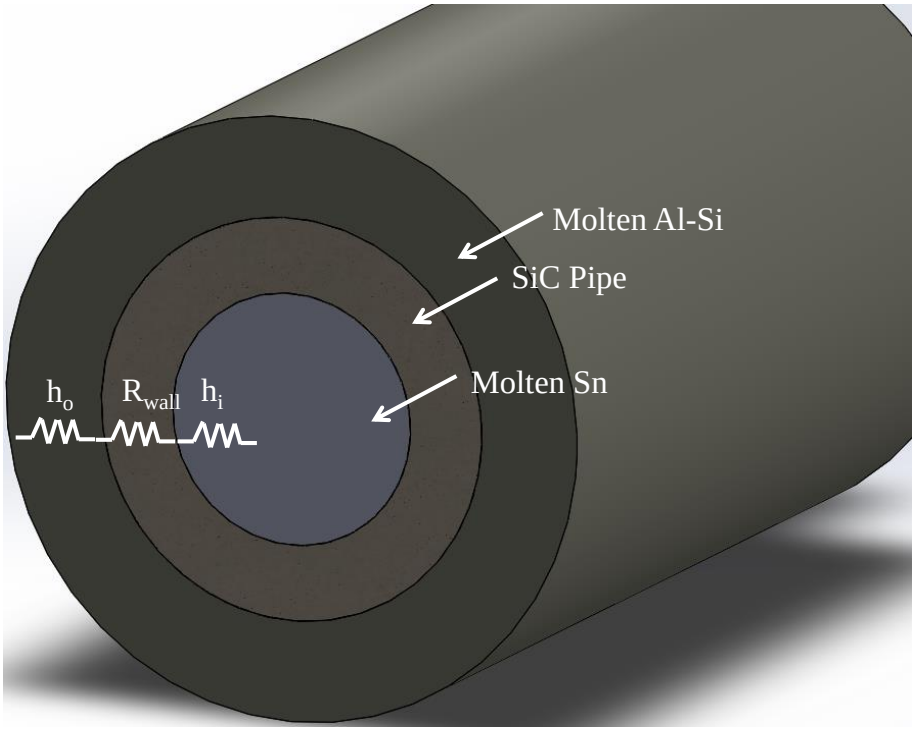

Fig. 27: Heat Exchanger Pipe

$$U = \frac{1}{\left(\frac{1}{h_{inner}} + R_{wall} + \frac{1}{h_{outer}} \right)} \tag{36}$$

The pressure drop across the heat exchanger tubes was calculated according to the following formula:

$$\Delta p = \frac{fLV^2}{2gD} \tag{37}$$

where f was the friction factor, L was the pipe length, V was the flow speed, g was the gravitational constant, and D was the inner diameter of the pipe. The pressure drop for the shell side was given by the following formula from the Kern Method [78]:

$$\Delta p_s = \frac{4 f G_s^2 D_s (N_B + 1)}{2 \rho D_e \left(\mu / \mu_w \right)^{0.14}} \tag{38}$$

where N_B was the number of baffles and ρ was the fluid density.

Shell and Tube Heat Exchanger Results

There were two shell and tube heat exchangers in the nominal design: one transfered heat from Sn at 1,400°C to Al-Si(l) at 830°C, charging the storage tanks, and the other transferred heat from Al-Si(l) at 1,350°C to He at 820°C, powering the topping cycle. The temperature averaged properties of the materials used in the shell and tube heat exchanger analysis are tabulated below:

Table 15: Shell and tube heat exchanger material properties[47, 79]

	Al-Si	Sn	He	SiC
Pressure (atm)	1	50	30	
Density (kg/m^3)	2433	7300	1.08	3100
Heat Capacity (J/kg-K)	1089	234	6225	670
Thermal Conductivity (W/m-K)	120	30	0.5	36
Viscosity (cP)	1.1	1.85	0.06	
Prandtl	0.01	0.01	0.75	

The results for each heat exchanger per the configuration tabulated in Table 14 are shown below:

Table 16: Thermal results for heat exchanger

	HX#3 Sn to Al-Si		HX#4 Al-Si to He	
	Shell	Tube	Shell	Tube
Fluid	Al-Si	Sn	He	Al-Si
Inlet Temperature (°C)	830	1,400	820	1,380
Outlet Temperature (°C)	1,380	850	1,350	830
Mass Flow rate (kg/s)	264	1,230	23.9	137
Volume Flow rate (m^3/s)	0.11	0.17	22	0.06
Heat Transfer Rate (MW)	158	158	82	82
Reynold's Number x 10^3	31	75	5.5	2.5
Nusselt Number		10.8		5.08
h (W/m-K)	25,300	29,500	1,820	55,463
Δp (kPa)	340	2.12	78.9	0.056

The shell and tube heat exchangers were cost estimated based on the length of SiC pipes required. Costs were normalized to electric output by dividing by the product of the heat transferred and power cycle efficiency (0.6) and the costs for both shell and tube heat exchangers are shown in the following table:

Table 17: Shell and tube heat exchanger pipe cost

	HX#3 Sn to Al-Si	HX#4 Al-Si to He
Pipe Length (m)	15,360	115,520
Total Cost (M$)	1.08	8.09
Normalized Thermal Cost ($/kW$_t$)	6.80	98.60
Normalized Electric Cost ($/kW$_e$)	11.34	164.36

Shell and Tube Heat Exchanger Conclusions

Heat exchange took place between two LMs with extremely high thermal conductivities as compared to non-metals, leading to high convective coefficients that

greatly minimized the required surface area, parasitic loss, and cost for the heat exchangers. Pressure losses through both heat exchangers were low: 3.3 atm for the Sn to Al-Si heat exchanger and 0.77 atm for the Al-Si to He heat exchanger. The pressure difference through the Sn to Al-Si heat exchanger was provided by a LM pump that used electricity from the gross plant output. Full analysis of this parasitic loss was presented in the parasitic loss section, and the result was 0.03 MW_e - a very small fraction (0.02%) of plant output (168 MW_e). The primary reason for low parasitic loss in this subsystem was the high heat exchanger conductance due to high LM convection, which resulted in low requisite LM flow rates as compared to a non-metal fluid such as LS.

The pressure loss through the Al-Si to He heat exchanger, 0.77 atm, was not provided via pump but rather the compressor on the topping Brayton cycle. Recalling Fig. 25, the He gas was compressed to 50 atm before entering the shell and tube heat exchanger. 0.77 atm was then lost through the heat exchanger so the He entered the turbine at a slightly lower pressure than it came out of the compressor.

The costs for the two shell and tube heat exchangers were added to their respective subsystems, 'TES' for heating the Al-Si and 'Power Cycle' for cooling the Al-Si. The LS-CSP plant required no TES heat exchanger since LS was used both as the HTF in the receiver and TES fluid. Therefore, the Sn to Al-Si heat exchangers were an added cost with no LS-CSP plant parallel. They were ~20% of total TES cost and not economically prohibitive for using two different LMs.

The second shell and tube heat exchanger, Al-Si to He, was a more costly system and was added to the power cycle costs. The LS-CSP power cycle used a stainless steel heat exchanger that exchanged heat between LS and steam for the power cycle. The LM

shell and tube heat exchanger was \$164/kW_e while the LS-CSP plant version was \$214/kW_e, which was a significant cost reduction.

The two shell and tube heat exchangers analyzed here did not transfer heat to solid particles. Instead, three LDHXs provided the necessary heat exchange between Al-Si(s) in the LM-CSP plant. In the LDHX analysis that follows, it is shown that these LDHXs were power dense and therefore inexpensive with regard to materials and parasitic loss.

Liquid Droplet Heat Exchanger (LDHX)

Examining the system configuration for charging and discharging the storage tanks (Fig. 24 and Fig. 25), anytime a heat exchange took place between He gas at atmospheric pressure and LM, a direct contact LDHX was used. The LDHX split the LM flow into small (<1 mm) droplets that fell down a tank, while a column of He gas flowed upward (Fig. 28). LDHXs have been explored before for space applications as well as inert gas Brayton cycles [80, 81].

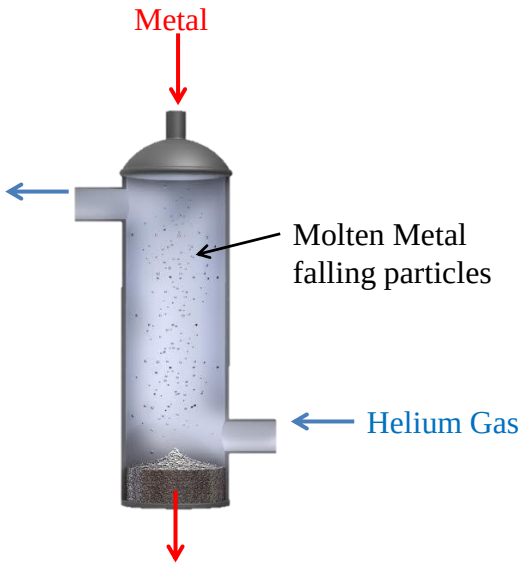

Fig. 28: LDHX configuration

Direct contact heat exchangers could only be used between constituents that were non-reactive and immiscible with each other. The advantage was that no separating barrier (i.e. SiC pipe) was required between the two fluids, which eliminated a major thermal resistance. More efficient heat transfer due to direct contact greatly increased the power density of the heat exchanger and the elimination of pipes drastically reduced the cost normalized to the heat transferred as compared to a shell and tube configuration. Another advantage to the LDHX [81] was that it allowed for a two phase storage fluid, which was especially useful since 40% of the energy stored in the melt was due to latent heat of fusion (e.g., Al-Si(l) solidification from 577-822°C). Al-Si(s) could not be pumped through the small diameter tubes in the shell and tube configuration, so instead, latent heat was transferred via LDHXs where the droplets could freeze or melt without physical constraint.

The nominal LDHX design was a hollow cement column with a cement disk at the top that had small holes drilled into it to act as nozzles for the metal drops. The cement was the same calcium aluminate engineered by Westmoreland Advanced Materials to resist corrosion from Al(l) used for the tank design [74]. Cost calculations for the cement were performed on a per volume basis, with Westmoreland quoting \$5950/m^3 for ALII castable cement.

LDHX Heat Transfer Analysis

Cost estimation of the LDHX was performed by calculating the column size necessary for the required heat transfer. The droplet diameter and heat exchanger diameter were the two design variables that were adjusted to reduce the heat exchanger costs. For all three LDHXs, the chosen droplet diameter was 0.5 mm. The shell diameter

varied for all three units but was ~10m. The LDHX was sized so that drops were separated by an average distance of 10 diameters to avoid coalescence. Additional research into drop coalescence was needed to determine the precise spacing needed, but nominally, 10 diameters was used in subsequent calculations because that was the pipe entrance length necessary before end effects do not affect flow [69]. Once the column dimensions were known for the required heat transfer, then the volume of concrete required to build the column was calculated for a half meter thick wall (recommended by Westmoreland Advanced Materials Inc.) along with the necessary insulation to limit heat leakage to 0.1% of the heat transferred. The castable cement cost factor and fiberglass insulation cost factor was applied to the calculated material volumes to get the final LDHX cost.

The first step in designing a liquid droplet exchanger was calculating the time required for each metal droplet, which was dragged upward against gravity by the He flow, to decrease its temperature from the inlet temperature to desired outlet temperature. Each metal droplet was approximated as a sphere with a specified droplet diameter. The diameter was adjusted later to balance terminal velocity against the number of total holes drilled, but eventually became equal to 0.5 mm in all heat exchangers. Next, the terminal velocity of the particle was calculated by equating the drag force to the weight. Equating these forces and algebraically solving for terminal velocity, v_t gave:

$$v_t = \sqrt{\frac{2mg}{\rho A C_D}} \tag{39}$$

where ρ was fluid density, m was the droplet mass, g was gravitational constant, A was cross sectional area of the drop, and C_D was the drag coefficient of a sphere, 0.49 [82].

Knowing the terminal velocity allowed the convection coefficient to be calculated. For convection over a sphere, Whitaker recommended [69]:

$$Nu_{sphere} = {hD}/{k} = 2 + \left[0.4\,\mathrm{Re}^{1/2} + 0.06\,\mathrm{Re}^{2/3} \right] \mathrm{Pr}^{0.4} \left(\mu_\infty / \mu_s \right)^{1/4} \tag{40}$$

where h was the convective coefficient, k was the thermal conductivity of the fluid, D was the diameter of the droplet, Pr was the Prandtl number of the fluid, μ_∞ was the dynamic viscosity at the free stream temperature and μ_s was the viscosity at the sphere temperature. Convective coefficients on the order of ~2,000 W/m^2-K were obtained and the LDHX was arranged so that there was only a ~10°C temperature difference between the fluid and the sphere. One result of this was that the two viscosities became approximately equal, due to the weak temperature dependence of viscosity on temperature. The Reynolds number, Re, was a function of the terminal velocity v_t:

$$\mathrm{Re} = \frac{\rho v_t D}{\mu_s} \tag{41}$$

the Reynold's number was low ~ 6, which was valid for the Whitaker correlation (3.5 < Re < 80,000).

With the droplet convection coefficient known, the heat transfer rate for each drop was calculated using the log mean temperature difference of the heat exchanger. With each LDHX design, the inlet temperature and outlet temperature was specified. The LMTD was calculated as follows:

$$\Delta T_{LM} = \frac{(T_{M,i} - T_{He,o}) - (T_{M,o} - T_{He,i})}{\ln\left(\dfrac{(T_{M,i} - T_{He,o})}{(T_{M,o} - T_{He,i})} \right)} \tag{42}$$

where *M* referred to metal, *He* referred to He, *i* referred to the inlet and *o* referred to the outlet. LMTD for this analysis was 14.4°C. The heat transfer rate for each drop, Q_d, was then calculated from:

$$Q_D = h \times A \times \Delta T_{lm} \tag{43}$$

where *A* was the surface area of a drop. This analysis considered the temperature throughout the droplet to be uniform via the lumped capacitance model and Q_D for these analyses was 0.021 W. The Biot number was calculated for the final heat exchanger design to test the validity of this assumption:

$$Bi = \frac{hV}{Ak} \tag{44}$$

A Biot number less than 0.1, implied that the temperature difference between the center of the droplet and its outer surface was less than 10% of the temperature difference between the outer surface and the surrounding (flowing) gas temperature. Under such conditions, the droplet was treated as essentially isothermal since the temperature difference due to conduction was negligible by comparison to the temperature difference driving the convection. In all three LDHXs modeled, the Biot number was < 0.005, which suggested the neglect of the droplet's internal temperature profile would lead to a negligible difference in the final analysis.

To estimate the time each drop must have spent falling at the terminal velocity, t_f, the enthalpy change for each droplet, Δh, was divided by the previously calculated Q_D.

$$t_f = \frac{\Delta h}{Q_D} \tag{45}$$

As an example, the time of flight, t_f, was 2.0 seconds for LDHX#1. The energy per drop was calculated from the known drop mass (m), specific heat (C_p), latent heat of fusion (h_f), and inlet/outlet temperatures:

$$\Delta h = \left(C_p\left(T_i - T_o\right) + h_f\right)m \tag{46}$$

and in the subsequent analysis, Δh, was on the order of ~ 0.1 Joules.

With the required flight time known, the column height was estimated by multiplying the particle velocity by the flight time. However, the terminal velocity with respect to the stationary ground, v_g was different from the relative velocity between the droplet and gas, v_t, because the gas was moving up the column at an appreciable speed. Thus, the particle velocity relative to the ground, v_g, was significantly lower than the relative velocity between the droplet and gas, which served to strongly increase the total time it took for a droplet to fully descend, thereby minimizing column height, C_h.

$$v_p = v_t - v_g \tag{47}$$

$$C_h = t_f \times v_p \tag{48}$$

Typical particle velocities were ~4 m/s yielding a column height ~10 m. Because the gas inlet temperatures and heat exchanger power were known, the gas flow rate was known and the volumetric flow rate was then calculated from the mass flow rate using the mean gas temperature and density. The gas velocity was then calculated by dividing the volumetric flow rate by the cross sectional area of the heat exchanger and the gas speed was ~9 m/s.

The droplet and heat exchanger diameters were the design parameters that could be altered within three physical constraints to reduce cost. The heat exchanger diameter

must have been large enough so the Reynold's number for gas flow was less than 10^5, reasonable for incompressible turbulent flows [69]. Much higher gas flows led to greater pressure losses and parasitic pumping loss. The second constraint was ensuring the droplets were large enough so the drag force did not exceed their weight and force the particles upward; however, if the particles were too large, they would need to be suspended in the flow for a longer period of time to transfer their energy.

The third and most expensive constraint when designing the LDHXs was ensuring the chosen heat exchanger diameter provided enough space so that the droplets did not coalesce. This issue was complex, because the droplets could actually break up into smaller droplets depending upon the surface tension. As an order of magnitude approximation, based on the typical length scales required for flows to return to uniformity, which would prevent a droplet in the wake of another droplet from experiencing a different trajectory, the spacing between droplets both vertically and horizontally was taken to be 10 times the droplet diameter [69]. Each hole then had a set time between drops, to allow the previous droplet enough time to fall 10 diameters away. The time between drops, or t_D, was calculated by:

$$t_D = \frac{10D}{v_p} \tag{49}$$

For the different LDHXs, t_D was typically ~ 1 ms, the enthalpy per drop, Δh, was calculated in Eq. 46, and dividing this by the time between drops gave the enthalpy flow through each hole as:

$$P_h = \frac{\Delta h}{t_D} \tag{50}$$

For the various LDHXs, P_H was typically ~ 88 W, which then allowed estimation of the total number of holes required, by dividing the total heat exchanger power by P_H which resulted in typically ~ 4 million holes. The effective area allocated for each droplet hole was then determined by forming a square around the hole 10 diameters wide (Fig. 29).

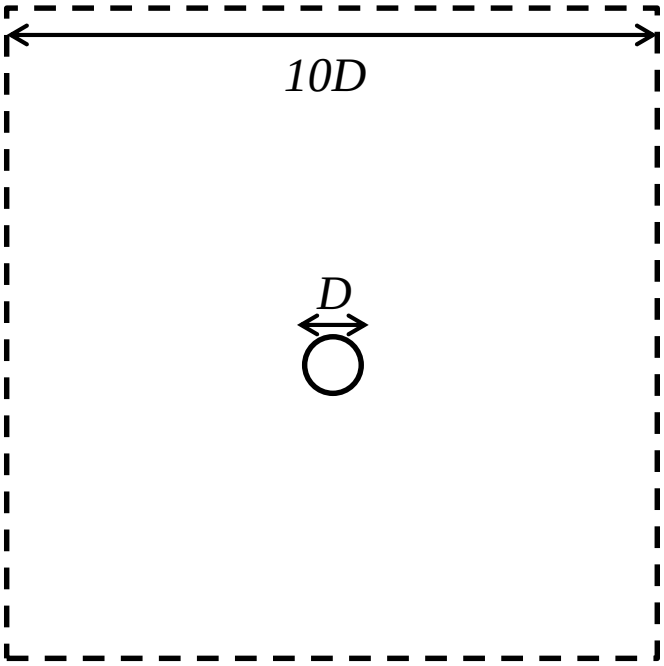

Fig. 29: Hole effective area

This area was then multiplied by the total number of holes and compared to the heat exchanger cross sectional area. The nominal design heat exchanger diameter was increased until the cross sectional area exceeded the required total hole allocation area.

LDHX Parasitic Losses

Parasitic losses in the LDHX could have potentially come from two sources: He flow and creating LM droplet surface area. The cross sectional area for the He flow was so large that pressure losses were less than 1 Pa for all three heat exchangers. The second loss came from dividing LM flow into millions of drops and increasing the metal's surface area. The experimentally measured surface energy was 0.7 J/m^2 for Sn(l) and 1.1

J/m^2 for Al-Si [83]. The parasitic energy loss required to form droplets, P_D was then estimated as:

$$P_D = \frac{\gamma \times A \times N}{t_D} \tag{51}$$

where A was the surface area of a drop, N was the total number of droplet holes, and t_D was the previously calculated time between drops.

LDHX Results

The preceding analysis was conducted for the three LDHXs as shown in Fig. 24 andFig. 25. The chosen design parameters, costs, and parasitic loss are given in Table 18.

Table 18: LDHX Results

	LDHX#1 He to Al-Si		LDHX#2 Sn to He		LDHX#5 Al-Si to He	
	Droplet	Gas	Droplet	Gas	Droplet	Gas
Fluid	Al-Si	He	Sn	He	Al-Si	He
Inlet Temperature (°C)	250	840	850	270	830	240
Outlet Temperature (°C)	830	270	290	840	250	810
Mass Flow rate (kg/s)	606	107	2915	107	314	55.8
Heat Transfer Rate (MW)	382		382		198	
Droplet Diameter (mm)	0.5		0.5		0.5	
Shell Diameter (m)	11		9		8	
Reynold's Number x 10^5	3.12		3.8		2.2	
Gas Speed, v_g (m/s)	19		28		18	
Terminal velocity, v_t (m/s)	23.3		40.3		23.3	
Particle Speed, v_p (m/s)	4.39		12.1		4.76	
Nusselt Number	3.93		4.58		3.93	
h (W/m^2-K)	2,360		2,750		2,360	
Time of Flight (s)	3.76		2.01		3.76	
Tower Height (m)	16.5		24.3		17.9	
Enthalpy per drop, Δh (J)	0.10		0.06		0.10	
Time between drops, t_D (ms)	1.14		0.5		1.05	
Power per droplet hole, P_H (W)	88		151		95.6	
Number of Holes, N (million)	4.34		2.52		2.07	
Gas flow Parasitic loss Δp (Pa)	0.01		1.3		0.46	
Liquid Metal Parasitic Loss, P_D (kW)	2.1		3.53		1.7	

A cement shell surrounded by insulation made up the inner flow column specified in Table 18 and the cement wall thickness was 0.5 m, which was the nominal cement thickness for Westmoreland designed Al holding vessels [74]. The top and bottom of each LDHX featured a castable cement disk 0.5 m thick where the castable cement was \$5,950/m^3. The bottom disk served as the base and top disk had holes drilled into it that served as the nozzle holes. The cement column was surrounded by rock wool insulation with a thermal conductivity of 0.2 W/m-K and cost \$1,300/m^3. The thickness of insulation was calculated to reduce heat leakage to 0.1% of heat flow through the heat exchanger.

Table 19: LDHX Costs

	LDHX#1 He to Al-Si	LDHX#2 Sn to He	LDHX#5 Al-Si to He
Cement Volume (m^3)	411	441	303
Cement Cost (M\$)	2.45	2.63	1.80
Insulation Thickness (cm)	23	26	33
Insulation Volume (m^3)	198	249	216
Insulation Cost (M\$)	0.26	0.32	0.28
Total Cost (M\$)	2.76	3.00	2.12
Normalized Thermal Cost (\$/kW_t)	7.22	7.86	10.7
Normalized Electric Cost (\$/kW_e)	12.0	13.1	17.8

The cost of the He to Al-Si heat exchanger and Sn to He heat exchanger were added to the TES heat exchanger cost in the TES subsystem, which also included the Sn to Al-Si shell and tube heat exchanger discussed previously. The Al-Si to He LDHX cost was added to the Power Cycle cost. The LDHX could have been made more power dense and cheaper if the distance between droplets was decreased from 10 diameters clearance. Thus, more experimental investigation was required to minimize spacing while preventing flow coalescence thus reducing heat exchanger costs, however, even without optimization the estimated costs resulted in minimal impact on the LCOE (e.g., < 10%).

CHAPTER 7: POWER CYCLE

The power block was the fourth and final subsystem whose cost was estimated. Its cost was normalized by the gross power output, i.e., by expressing all components in units of $/kW$_e$. The power block included the combined power cycle, heat exchangers to transfer heat from the TES fluid to the working fluid, hot LM pumps, spare parts, and auxiliary equipment.

The power cycle modeled was a combined cycle utilizing an inert gas working fluid, whereby inert He gas ran through a closed loop Brayton cycle that received heat from the sensible portion of the melt: 1,350°C to 820°C accounting for 28% of stored thermal energy (Table 10). The latent heat and solid sensible heat was then transferred into a SCO2 (SCO2) cycle that received 78% of total stored energy and operated between 800°C and 220°C. In this sense, the primary cycle was the SCO2 cycle, and the He Brayton cycle acted as a topping cycle to help boost the overall efficiency.

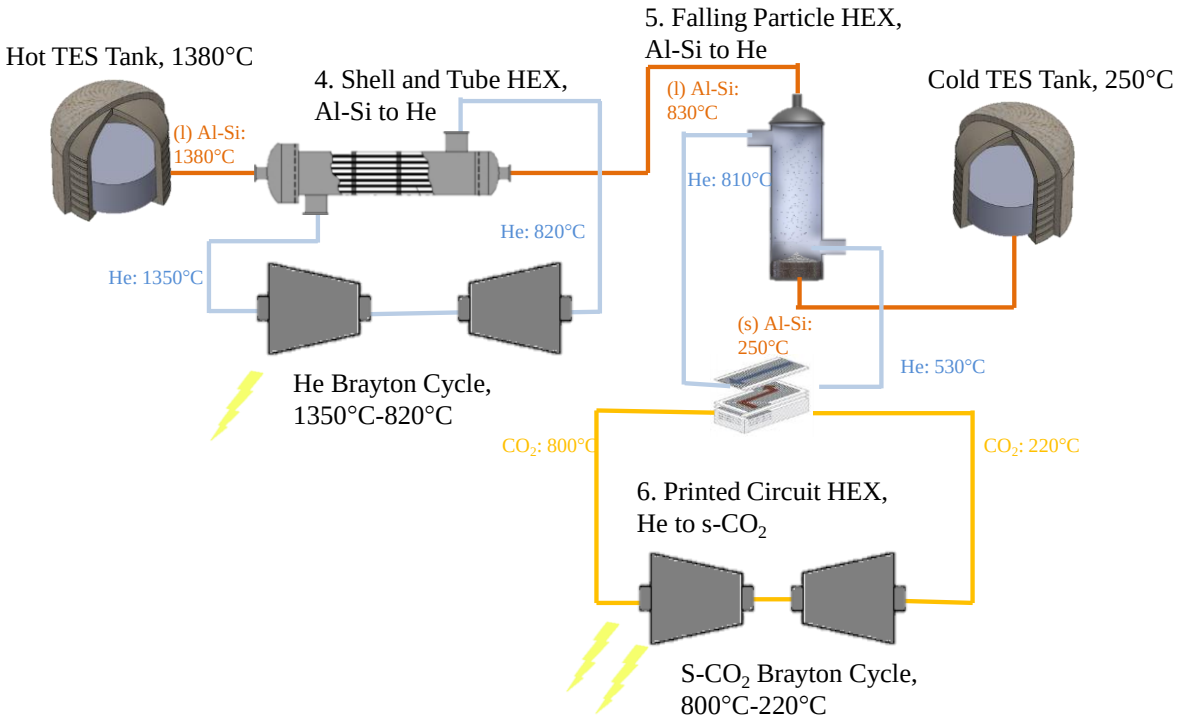

Fig. 30: Power Cycle Diagram

The cycle shown in Fig. 30 did not exist commercially, but there was a body of literature and experiments that support the notion that such a cycle could be built and potentially achieve 60% efficiency [79, 84, 85]. For example, Siemens had built commercial combined cycle plants that combust natural gas >1,200°C and power a Brayton cycle with heat rejected to a Rankine cycle for a combined efficiency of 60% [12]. The cycle envisioned for this CSP plant used He as a working fluid instead of air and required an additional heat exchanger to transfer heat from the LM to the working fluid. However, the key potential advantage of the cycle described in Fig. 30 was that it relied primarily on a more efficient SCO2 Brayton cycle, instead of a steam Rankine cycle. This suggested that there may exist a cycle configuration that could reach 60% efficiency or possibly higher. It is also important to note, however, that in current natural gas Brayton cycles, the additional heat exchange with the heat source was not required

because the natural gas was mixed with the air and ignited in the combustor. Therefore additional pressure losses were expected for the heat addition step that were not encountered in industrial scale gas turbines. Nonetheless, inert gas Brayton cycles, while not currently available commercially, are feasible to design and build [79, 86, 87].

The bottoming cycle was a SCO2 cycle that was used instead of a steam Rankine because of the higher temperature capabilities and higher power density [88]. The low volumetric flow rates required in a SCO2 cycle also reduced parasitic losses in the cycle and improved efficiency. Ultra-supercritical steam cycles with temperatures up to 760°C were also being developed and could be a second viable option for the bottoming cycle [89]. Leveraging cutting edge research in turbine technology that could enable 60% thermal to electric conversion, was essential to realizing the cost savings from the higher temperature LM-CSP plant.

Power Cycle Heat Exchangers

Fig. 30 shows that two heat exchangers were required to transfer heat from the storage fluid to the working fluid: shell and tube HX#4 and LDHX#5. Both these heat exchangers were described and cost modeled in Chapter 6. The shell and tube heat exchanger had a cost of $\$164/kW_e$ and provided 29% of thermal input to the working fluid while the LDHX was $\$25.2/kW_e$ and provided 71% of thermal input. This yielded a combined cost of $\$189.2/kW_e$, which was 12% lower than the cost of its LS-CSP plant equivalent which was $\$214/kW_e$. The third heat exchanger was a printed circuit board heat exchanger that transferred heat between He and SCO2. This heat exchanger was not cost modelled because its cost was included in literature provided cost estimates for SCO2 cycles [90]. There was no LS-CSP plant parallel because only one Rankine cycle

was used for that configuration. The cost of a combined cycle given by the US Energy Information Agency was \$917/kW_e vs. current LS-CSP power plants that used a Rankine cycle that was 41% efficient and was \$1,050/kW_e [48].

LM pump

The power block required a LM pump that could pump 1,350°C Sn through the power cycle heat exchangers. The development and demonstration of such a pump was ongoing at publication and its cost was comparable to similar options that could be used for LS. Therefore, as a more conservative assumption, its cost was estimated by applying a material cost factor of 2X to current LS pumps. LS pumps were made from stainless steel and for LS-CSP systems cost \$4/kW_t. For the 280 MW_t power cycle that was modeled here, a LS pump was \$1M. A possible ceramic material for a LM pump was AlN, which was twice as much as stainless steel [47]**.** Applying this 2X cost factor, a LM pump would cost \$2M, which was only \$12.4/kW_e. While using a material cost factor was a simplified alternative to designing the pump geometry, the pump was only 2% of power block costs and therefore even if the estimation was too low by a factor of 2-3, it would not have translated to a significant effect on the overall system LCOE. The cost of each power block component was estimated in Table 20, which provides a comparison between LS and LM.

Table 20: Power block cost comparison

Power Block				
	LS-CSP		LM-CSP	
	Total M$	$/kWe	Total (M$)	$/kWe
Working Fluid Heat exchanger	21.4	214.0	10.2	63.1
Structures/Foundations	0.1	1.0	0.1	0.6
Power Cycle	120.5	1050.0	154.1	917.0
Hot Salt Pumps	1.0	10.0	2.0	12.4
Auxiliary equipment	0.3	3.0	0.6	3.8
Spare Parts	0.1	1.0	0.2	1.3
Total Capital Cost	**143.4**	**1279.0**	**167.6**	**998.0**

Parasitic losses

The parasitic losses for a CSP plant came primarily from fluid flow losses and heliostat tracking. For a LS CSP plant that had a gross output of 115 MW_e, the parasitic loss was estimated at 15 MW_e for a net output of 100 MW_e [10]. On the other hand, the parasitic loss for a LM-CSP plant was calculated to be 6.2 MW_e for a net output 162 MW_e. One of the key advantages of using LM as a heat transfer fluid was that its high thermal conductivity resulted in much lower flow rate requirements to achieve the same convective coefficient and therefore low parasitic pumping loss. The disadvantage to the nominal LM-CSP design was that both Sn and Al-Si are used. These two different fluids required He gas as an intermediary heat transfer fluid when the Al-Si is freezing and could not be pumped though a Sn shell and tube heat exchanger. High gas flow rates were required leading to significant parasitic pumping losses in the system. Furthermore, using a 2 phase storage fluid required LDHXs that operated at atmospheric pressure since their large size (10m) would be expensive to engineer for higher pressures. Therefore, the Sn coming down from the tower experienced a pressure drop to atmospheric pressure

prior to entering the Sn(l)/He heat exchanger. This meant that the gravitational pressure, 12 MPa, required for pumping Sn up the 180 meter receiver tower was provided by the LM pump and not suction force from Sn flowing down the tower. Furthermore, the frictional pressure loss in the tubes going up the tower added an additional 5 MPa of pressure loss. The Sn flowrate used in the parasitic loss calculation was for 280 MW_t, not 540 MW_t which was the peak receiver output. The receiver output was dependent on the time of day and incident solar flux therefore these differences were accounted for by using the Sn flowrate that corresponded to the power cycle output, which ultimately parasitic losses were subtracted. With a Sn flow rate of 0.16 m^3/s, the Sn(l) pump required 2.7 MW and represented the largest parasitic load in the plant (Fig. 31).

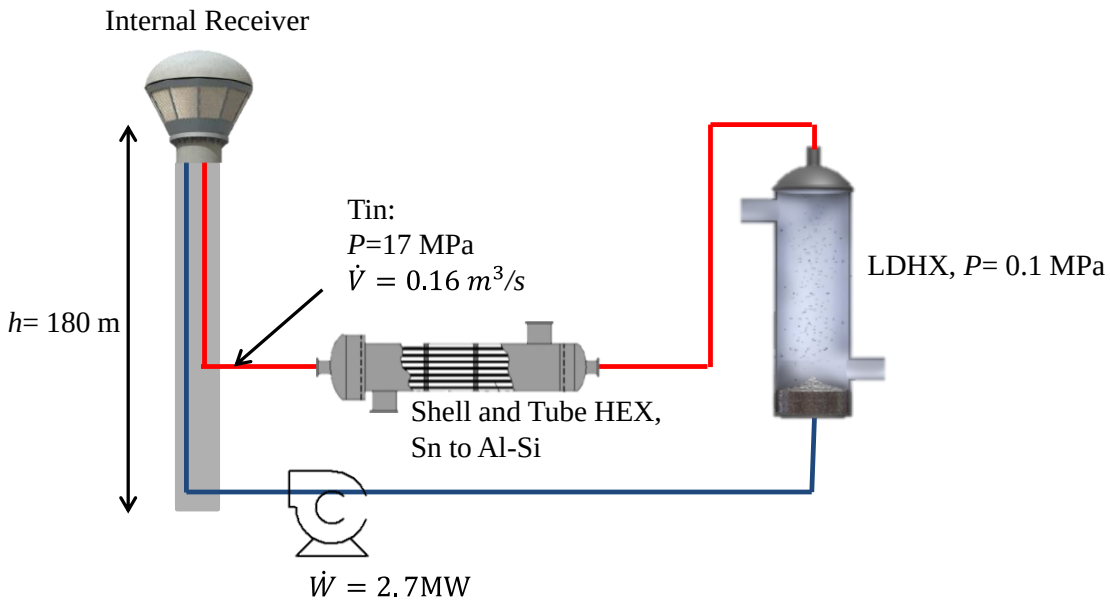

Fig. 31: Sn flow parasitic loss

Major Pumping Losses

Major pumping losses occurred in the receiver, tower piping, TES heat exchangers, and power cycle heat exchangers. The pressure losses for each subsystem

were calculated in previous sections. Each pressure loss was converted to pump work, W_{shaft}, by the following Eq.:

$$\dot{W}_{shaft} = \dot{V} \times \Delta p \tag{52}$$

where V was the volumetric flow rate in m^3/s and Δp was the pressure loss for that subsystem. The following tabulates the pressure loss, flow rate, and calculated pump power required for each subsystem:

Table 21: Major head loss

Component	Pressure Loss (Pa)	Volumetric Flow rate (m^3/s)	Parasitic Power (kW)
Receiver	12,000	0.16	2
TES Piping	16	0.16	0.003
TES Tower	17,000,000	0.16	2700
Shell and Tube Sn to Al-Si (Tube Side)	2125	0.17	0.36
Shell and Tube Sn to Al-Si (Shell Side)	350,000	0.11	38
Shell and Tube He to Al-Si (Tube Side)	59	0.06	0.0034
Shell and Tube He to Al-Si (Shell Side)	79,000	22	1700
Liquid droplet Al-Si to He (Gas)	0.02	930	0
Liquid droplet Al-Si to He (Particle)	N/A	N/A	N/A
Liquid droplet Sn to He (Gas)	0.26	1800	0
Liquid droplet Sn to He (Particle)	N/A	N/A	N/A
Liquid droplet He to Al-Si (Gas)	0.01	1800	0
Liquid droplet He to Al-Si (Particle)	N/A	N/A	N/A
Total			4500

In total, 4.5 MW of pumping power was required, most of which was pumping power required to push Sn up the tower and could be reduced by employing an expander

(i.e., a pump pushed by the LM to drive its shaft) at the base of the tower to feed the Sn pump with recovered shaft work prior to the LDHX. Only 1.8 MW was required for the rest of the heat exchangers and the majority was required to flow He through the shell side of the shell and tube heat exchanger (1.7 MW). In reality, the pressure drop (0.77 atm) would come at the expense of the compressor outlet pressure and decreased Brayton cycle turbine performance; however, it was included here as a pump parasitic power.

Kolb et al. also provided estimates for the parasitic losses associated with tracking motors in the heliostat field. Since the mirror field for the LM-CSP plant was identical to the LS plant, this parasitic loss was the same at 1.75 MW [10]. Adding the pumping parasitic loss with the heliostat field parasitic loss gave a total loss of 6.2 MW_e while the parasitic loss for the LS plant was 15 MW_e. These losses were very significant and their effect on plant output are shown in Table 22**:**

Table 22: Parasitic loss and plant output

	LS-CSP Plant	LM-CSP Plant
Parasitic Loss	15 MW	6.2MW
Gross Output	115 MW	168 MW
Gross Efficiency	0.4	0.6
Net Output	100	162 MW
Net Efficiency	0.36	0.58

CHAPTER 8: TEA CONCLUSION

The plant construction cost *K*, was the plant construction cost in dollars normalized by the net electric output of the plant in kW_e. *K* was the primary cost variable for CSP plants and was found using the results of the above analysis. Again, from Chapter 2, *K* was expressed as: $K = \frac{A}{E} + \left(\frac{B}{\eta_E}\right) \times F + \left(\frac{C}{\eta_E}\right) \times t + D$. There were four terms that each normalized the cost of a subsystem to $/kW_e$ for the four subsystems: heliostat field, receiver, TES, and power block. The values used in Eq. 2 are presented in Table 23 for both the LS-CSP plant and LM-CSP plant. The LS-CSP plant values came from Sandia's Power Tower Roadmap and the LM-CSP plant numbers were a result of the preceding cost analysis.

Table 23: Overnight capital cost plant comparison

Variable	Unit	LS-CSP	LM-CSP
Solar Energy Collection			
A, Solar energy collection	M$	188	188
F, Solar Multiple	-	1.94	1.94
E, Net Electricity Generation	MW	99.8	161.7
ηe net, power cycle efficiency	-	0.36	0.58
Solar Energy Collection, Capital Cost	$/kW	1,880	1,160
Solar Receiver			
B, Cost of Solar Receiver	$/kW-th	104	179
Solar Receiver, Capital Cost	$/kW	562	598
Thermal Storage			
C, Cost of Thermal Storage	$/kWh-th	21.2	15.2
t, number of hours of storage	hr.	9	9
Thermal Storage, Capital Cost	$/kW	535	236
Power Block			
D, Power Cycle, Capital Cost	$/kW	1,270	998
K	$/kW	4250	2990
Contingency			
K1, Contingency	$/kW	425	299
K2, Contingency	$/kW	795	559
K_{total}	$/kW	5470	3850

The LCOE calculation was more complex than the overnight capital cost because it factored in maintenance, fuel costs, and generation over the plant lifetime. These quantities, however, were the same for both the LS-CSP and LM-CSP plants, thus, they did not contribute to the differences in LCOE.

The LCOE was calculated according to Eq. 1, for three different plant types: LS-CSP, LM-CSP, and natural gas. All plants analyzed were calculated with 20 year lifespans, so n=20. The investment expenditure, I_t in eq. (1, was only calculated for the first year and was equivalent to the overnight capital cost of the plant, K in Eq. 2 The values used for K ($) was calculated for LS-CSP and LM-CSP according to the approach

discussed in Chapters 2-7 and are given in Table 23. For providing a comparison to natural gas plants, the overnight capital cost was taken from Energy Information Agency report [48] and K was converted to dollars by multiplying by the plant's given nameplate capacity (kW). For natural gas plants, M_t, was given as fixed O&M costs in \$/kW-yr and M_t was converted to dollars per year by multiplying it by the plant's nameplate capacity (kW). The O&M costs, M_t, for the LS-CSP plant were taken as \$65/kW_e-yr based on estimates provided by the US-DOE [1].

A LM-CSP plant was expected to have similar operation and maintenance costs despite the additional nitrogen containment, heat exchangers, and exotic materials. This was because the most significant portion of the O&M costs were associated with maintaining the heliostat field, most specifically maintaining the electronics in mirror tracking as well as cleaning mirrors, which were exposed to the environment. Since the LM-CSP plant had the same heliostat field as the LS-CSP plant, these costs were expected to be the same at \$6.5M per year or \$4/kW_e-yr [10].

One major result of the preceding analysis was that N2 containment did not significantly raise the capital cost or O&M costs of the plant. Current LS-CSP plants were shut down approximately once a year to perform maintenance. For a Sn(l) plant with nitrogen containment, conceptually the system would have been purged with air, and then refilled with nitrogen after maintenance was performed. The cost of nitrogen required by the plant was calculated by summing the volume of all containment vessels and multiplying by the nitrogen cost per cubic meter, obtained from vendor quotes. The total volume of the receiver, TES tank containment vessels and heat exchangers was 20,300 m^3 and vendor (Airgas Inc.) quotes for N2 were ~ \$5.88/m^3 when purchased in

quantities of at least 300 liters (0.3 m^3). Thus, it was \$0.1M to replace all the nitrogen in the LM-CSP plant once a year or \$0.64/kW_e-yr, which was small compared to the base maintenance cost of \$4/kW_e-yr.

To evaluate Eq. (1), the real discount rate, *r*, was taken as a weighted average of inflation (3%), the nominal interest rate (7%), the nominal rate of return on equity (15%), the debt fraction (60%), the federal tax rate (35%), and an assumed state tax rate of (5%), which were all taken from the Sunshot Vision Study [1].

The fuel cost, F_t, only applied to natural gas plants and was calculated by Eq. 53:

$$F_t = C_{gas} \times HR \times E_t \tag{53}$$

where C_{gas} was the cost of natural gas, *HR* was the natural gas heating rate, and E_t was the electricity produced per year. E_t was solved according to the following Eq.:

$$E_t = G \times C \tag{54}$$

where *G* was the peak electric output, and *C* was the capacity factor. The capacity factor was the ratio between actual yearly output of the plant vs. the associated plant output if it ran at peak nameplate capacity continuously. The SAM gave the capacity factor of the CSP plant, 43%, which was dependent on the solar resource (Tonopah, Nevada) as well as the number of hours of TES built in (9 hours) [60]. Natural gas capacity factor was given by EIA's Electric Power Annual 2009 report as 87% for combined cycle natural gas plants [42].

Using the aforementioned inputs, the LCOE was calculated for the LS-CSP plant, LM-CSP plant, and a conventional combined cycle natural gas plant. The LCOE inputs and results are tabulated in Table 24.

Table 24: LCOE comparison of different energy sources

Plant Type	LS-CSP	LM-CSP	Combined Cycle Natural Gas
Nominal Capacity, (MW)	97	162	620
Overnight Capital Cost, I_1, (M$)	546	622	917
O&M Cost, M_t (M$)	6.5	6.5	13.17
Natural Gas Cost, C_{gas} ($/MBTU)	0	0	4.39
Heat Rate, *HR* (BTU/kWh)	0	0	7,050
Fuel Cost per year, F_t (M$)	0	0	144
Discount Rate, *r*	0.055	0.055	0.055
Electricity Produced, E_t (GW-hr/yr)	360	601	2,260
LCOE (¢/kW-hr)	13.4	9.3	6.3

TEA Conclusion

A CSP plant using LM had the potential to reduce costs because it could reach higher (1400°C) temperatures and drive a more efficient (60%) power cycle than the current state of the art, LS-CSP, plants which were limited by nitrate salt chemistry to 565°C and a 40% efficient power cycle. However, using LM as a HTF required switching from a metal containment infrastructure to a ceramic containment infrastructure and additional systems to exchange heat between LMs as well as to protect LM from oxygen were required in the LM-CSP design. Furthermore, since the receiver was much hotter than LS receivers, (1400 °C vs 565 °C), it had to be substantially redesigned to limit its view factor to the surrounding room temperature environment and avoid losing a large proportion of incident energy via re-radiation.

In order to determine if switching from LS to LM could reduce CSP costs, a LM-CSP plant was designed with the same heliostat field and thermal input as a published LS-CSP plant design in order to make accurate side by side comparisons. Material cost factors were applied to the design geometries and construction costs were scaled from LS-CSP estimates to calculate the total LM-CSP cost. Whenever there were design

choices, the more conservative option was used to more confidently answer if switching from LS to LM would reduce CSP costs. Ultimately, the LM-CSP design featured a graphite, modular cavity receiver using Sn(l) as the HTF to transfer heat to a two phase, Al-Si alloy that was contained in calcium aluminate cement storage tanks. Energy stored at 1380°C in Al-Si(l) was transferred via shell and tube and LDHXs to helium and SCO_2 working fluids for a combined power cycle with a net output of 162 MW_e. The costs for all the LM-CSP systems were normalized by this output and resulted in a design that had a LCOE 30% lower than LS-CSP.

While the LM-CSP ceramic infrastructure was more expensive than its LS steel counterpart, the higher energy density of Al-Si minimized the quantity of storage fluid necessary as well as the size of ceramic containment components, which led to a 50% cost reduction in the TES subsystem. Ideally, the energy dense Al-Si would have been used everywhere; however, Al corroded the graphite necessary for an efficient receiver, which necessitated a separate, smaller Sn loop to transfer heat to the Al-Si through a series of extra HXs. The extra tin loop and HX network was cost modeled in detail and did not make up more than 20% of the LM TES system. The LM receiver was nearly twice as expensive as the LS receiver due to the more complex internal cavity design, high temperature insulation, and graphite material cost. However, when normalized with respect to the plant electric output, the LM receiver was only 6% more expensive than the LS receiver. One important conclusion from the LM-CSP design was that the nitrogen containment systems and secondary concentrators not necessary in the LS-CSP plant were a minor cost, and only accounted for <1% of total plant costs. The power cycles for both modeled plants were approximately equivalent on a $/W basis, but the LM-CSP

cycle had the capability to be 50% more efficient than the LS-CSP plant due to the higher temperature heat input (1350°C vs. 565°C) for the same heliostat field or collection infrastructure. After taking into account parasitic losses for both plants, the LM-CSP net efficiency was actually 60% higher than LS-CSP because the high thermal conductivity of LM over LS led to a major decrease in flow speeds for equivalent heat fluxes. The reduction in flow speed decreased pressure losses throughout the receiver and heat exchangers, thereby decreasing parasitic losses by 59% compared to LS-CSP. The LM-CSP higher electricity output decreased the normalized cost of every subsystem compared to LS-CSP except the receiver, despite the additional heat exchangers, inert containment, receiver loop fluids, and more expensive ceramic materials required for LM-CSP. Switching to LM therefore has the potential to reduce the LCOE of CSP by at least 30% therefore requiring only a 20% further reduction in cost to achieve parity with natural gas combined cycle power plants.

CHAPTER 9: LM RECEIVER LOOP EXPERIMENTAL DESIGN

According to the techno-economic analysis presented in Chapters 2-8, using LM can reduce LS-CSP costs by ~ 30% and therefore it is important to further consider its associated technical challenges. There are three broad technical challenges with LM-CSP: (1) achieving an efficient (>90%) high temperature solar receiver, (2) successful construction of a reliable ceramic infrastructure, and (3) implanting an inert gas containment system. Within these 3 categories there are a number of smaller challenges. All of the foreseen technical challenges associated with building a full scale LM-CSP plant are listed in Table 25 with the challenges discussed in this thesis highlighted in bold. Many of these LM-CSP challenges have been addressed with a small scale, experimental LM loop that fits inside a 4' x 4' x 5' steel nitrogen containment, but a few challenges remain.

Table 25: Technical challenges with LM-CSP

Problem
>80% efficient high temperature receiver
Inert gas containment
Air curtain for higher receiver efficiency
Secondary concentrator
High intensity light windows
Low temperature mechanical support
LM flow meter
Thermocouple placement
High temperature reaction bonds
Sn Minor Flow Losses
High temperature shell and tube heat exchanger
Liquid droplet heat exchanger
High temperature heat sink
>1000 sun heliostat field
Inert gas Brayton cycle
Printed circuit SCO2 heat exchanger
Sn compatible ceramic pipes
Al-Si compatible ceramic pipes
Graphite mechanical pipe joints
LM valves

The LM loop's primary purpose was to test a high temperature cavity receiver at 1,350°C, where radiative heat flux from the receiver to the environment was much higher than at the current LS-CSP peak temperature of 565°C. Higher temperatures required a new optical cavity receiver geometry that limited the view factor between the surrounding environment and 1350°C Sn. According to the Stefan Boltzman law, heat flux, *Q",* was proportional to the receiver temperature:

$$Q'' \sim \left(T_{rec}^4 - T_{surr}^4\right) \tag{55}$$

where T_{rec} was the receiver temperature, and T_{surr} was the surrounding temperature [77]. Interestingly, although increasing receiver temperature from 565°C to 1350°C was only a 2.4X increase in ΔT, there was a corresponding 14X increase in re-radiative heat loss.

Current external receivers had efficiencies of ~ 90% [91]. Increasing re-radiative losses by almost an order of magnitude would have led to an inefficient receiver that negated the improvements in power cycle efficiency, unless higher concentrations and an internal receiver were used.

Building a full scale internal receiver several meters in length and testing it in front of a heliostat field was prohibitively expensive. Instead, a scaled down internal receiver (Fig. 32) was built and, at the time of publication, was being tested in front of a solar simulator (Fig. 33) that simulates the concentrated sunlight intensity of a heliostat field on a laboratory scale [52].

Fig. 32: Experimental laboratory graphite internal receiver. Keyboard in background for size reference.

Fig. 33: Solar simulator

In support of the internal receiver was a pump to flow Sn through the receiver, a heat sink system to remove the solar simulator heat input, and a flow meter to measure the Sn flow rate. These components were arranged in a loop, shown schematically below:

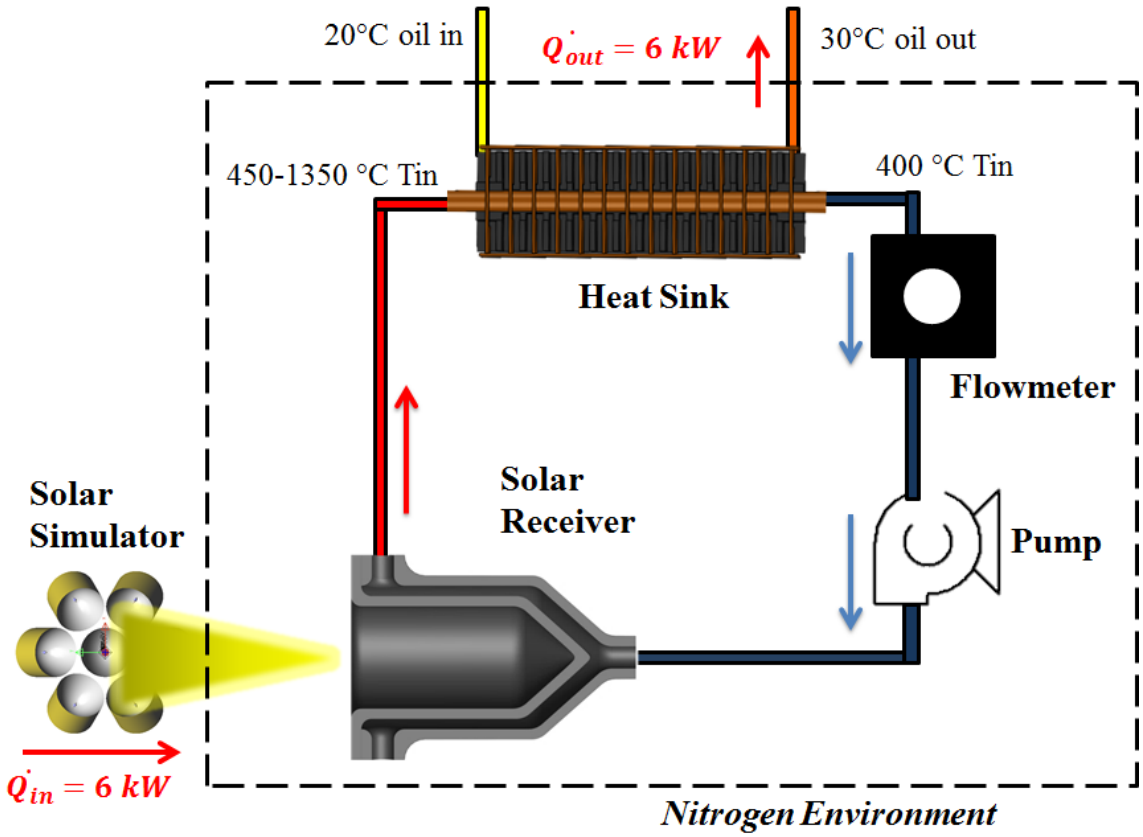

Fig. 34: Solar receiver experimental loop

LM and graphite would have oxidized rapidly at temperatures above 400°C limiting operation to only a few hours, therefore the entire experiment was assembled inside a sealed steel box into which nitrogen continuously flowed to drive out oxygen associated with any leaks (Fig. 35).

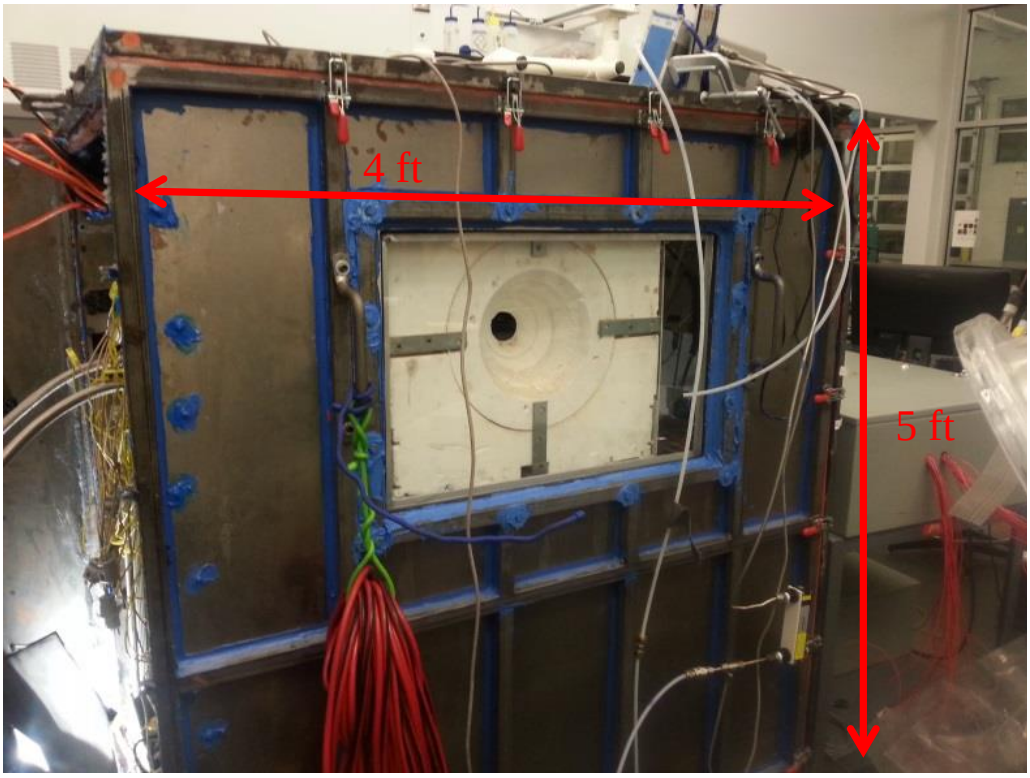

Fig. 35: LM receiver test loop inside steel nitrogen containment

Pipe Materials for Sn(l)

Stainless steel was the primary pipe and containment material for liquid nitrate salts in CSP plants, which limited the maximum temperature for LS-CSP designs to 565°C. Stainless steel could not be used for Sn(l), even at cooler temperatures (232°C) because Sn formed intermetallic compounds with the iron and chromium in steel [46]. Over relatively short time periods, Sn would corrode steel, effectively dissolving it away (Fig. 36).

Fig. 36: Two originally identical stainless steel gears. The right gear was corroded by Sn(l) after < 24 hrs. of operation. One steel gear was treated with a ceramic coating, while the other was not, which led to a major difference in corrosion.

As a result, ceramic pipes were necessary to contain Sn(l) due to their higher temperature limitations and chemical compatibility with Sn(l).

Possible pipe materials identified were mullite, graphite, and alumina because they were non-corrosive and non-wetting to Sn(l) [92]. For the experimental loop built, graphite pipes were chosen due to their low cost, thermal shock resistance, and high thermal conductivity [55].

Fig. 37: Graphite pipes used in experimental loops. Pipe on the right had OD: 0.5" and ID: 0.3125". Pipe on the left had OD: 0.875" and ID: 0.5"

To experimentally verify graphite's non-reactivity with molten Sn, G347 graphite tubes from Tokai Carbon were weighed and then immersed in 1,100°C Sn for 100 hours. After cooling, the graphite tubes were immersed in HCl to dissolve any solidified Sn that had adhered on or within the tube walls. The tube weight was measured again to determine a weight difference, which in turn would indicate whether any Sn had reacted with the graphite. The measured weights of the graphite tubes, before and after Sn immersion, are presented in Table 26.

Table 26: Weight loss measurements of graphite tubes in Sn(l)

Tube No., Purity	Tube Surface Area, cm2; Wall Volume, cm3; Wall Density, g/cm3	Tube Mass (g)		Tube Mass Loss/Area	Calculated Wall Thickness Reduction	
		Before Immersion	After Immersion	g/cm2	mm	Rel % Change
1 (99.5%)	42.74; 5.077; 1.740	8.8348	8.8343	1.170×10^{-5}	6.722×10^{-5}	0.00672
2 (99.5%)	42.55; 4.995; 1.735	8.6667	8.6662	1.175×10^{-5}	6.774×10^{-5}	0.00677
3 (99.5%)	43.50; 5.136; 1.696	8.7112	8.7106	1.386×10^{-5}	8.171×10^{-5}	0.00817
4 (99.5%)	41.63; 4.901; 1.682	8.2453	8.2448	1.201×10^{-5}	7.139×10^{-5}	0.00714

Based on the low change in weight (~0.006%), it was confirmed that the graphite pipes were non-reactive with Sn(l), even at 1,350°C.

The extent to which Sn(l) wets graphite was evaluated using electron microscopy. A G347 graphite tube that was sealed at one end to contain Sn was immersed in 1,100°C Sn(l) for 100 hours. After draining the Sn from the tube and cooling it, the graphite tube was filled with epoxy which maintained interface integrity as the tube was cut into rectangular pieces containing the epoxy/graphite interface. The sample was magnified under a scanning electron microscope (Fig. 38) and showed spherical solidified Sn phases at the interface indicating that the Sn did not wet and penetrate the graphite wall.

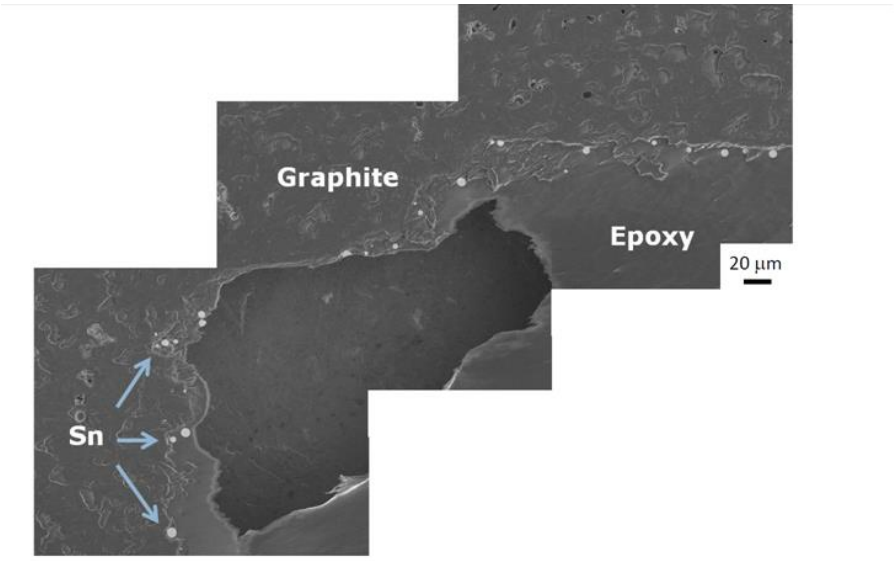

Fig. 38: SE images of the epoxy-graphite interface at the bottom of the one-end-closed graphite tube

These experiments showed that graphite was a viable pipe option for Sn(l) flow at 1100°C; however, for lower temperature circulation loops (<500°C), glass-lined stainless steel could be used. Coating the inside of a stainless steel with borosilicate glass protected stainless steel from Sn corrosion [93]. The advantage of glass-lined stainless steel over graphite was that typical stainless steel compression Swagelok fittings could be used for joints due to the higher ductility and strength. Glass-lined stainless steel pipes have been used in some experimental loops to test the LM pump and flow meter, but must did not exceed 500°C to avoid cracking and delamination of the glass lining.

Fig. 39: Sn filled section of glass-lined stainless steel tubing

The problem with glass-lined stainless steel was the delicate nature of the glass. Mishandling or cutting the tubes improperly caused the glass to shatter, creating cracks that allowed Sn(l) to reach the stainless steel. Furthermore, glass shards could break free and clog tube passages, the pump, or valves. For these reasons, glass-lined stainless steel was discontinued for Sn(l) loops, even for pipe sections that never exceeded 400°C.

Another option for stainless steel was coating it with titanium nitride (TiN), often used as a coating for steel tools to increase their hardness [94]. TiN was expected to be inert with respect to Sn(l) and was experimentally shown to protect stainless steel from Sn(l) corrosion up to 450°C, beyond which the differences in thermal expansion would cause the coating to delaminate from the steel [95]. Stainless steel swage compression fittings (unions, elbows, T-joints), were coated with TiN and used successfully with both

graphite and glass-lined stainless steel pipes in low temperature (<400°C) sections of LM loops (Fig. 40).

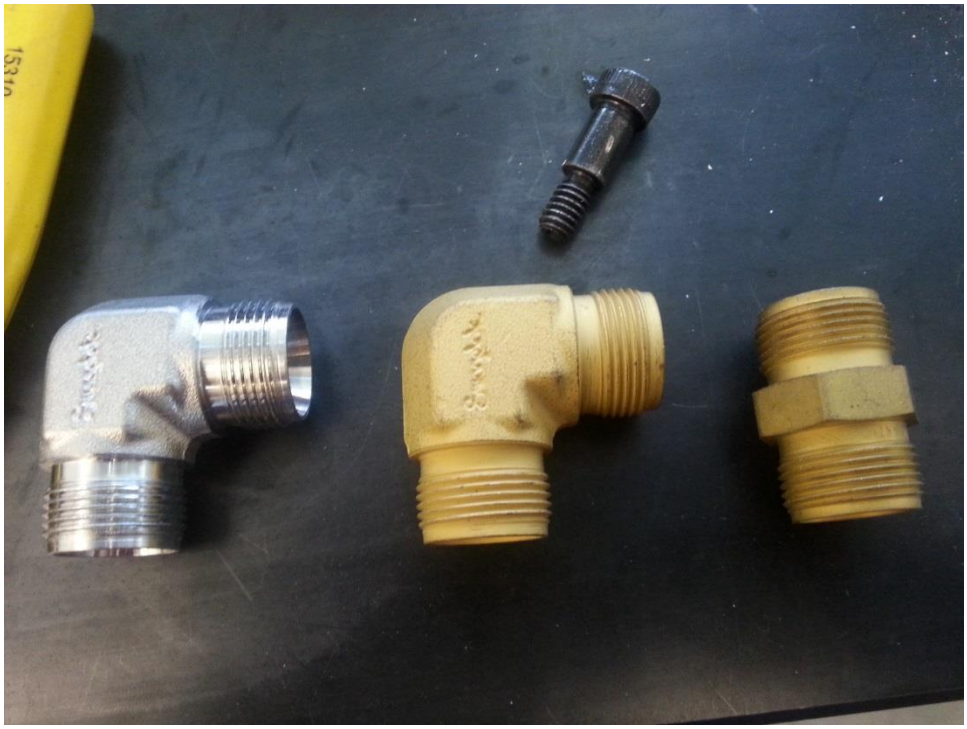

Fig. 40: TiN coated stainless steel fittings. Left most elbow was uncoated.

Pipe Connections

Joining graphite pipes and parts together with leak proof joints was more challenging than stainless steels. The strength of steel as well as its ductility allowed for easily connected pipes that could support their own weight. Switching to ceramic piping allowed higher temperatures, but at the expense of easily engineered connections and seals. For graphite pipe connections in these LM loops, there were two options: reaction bonds and mechanical compression fittings, both of which were demonstrated to work reliably, but required additional considerations as compared to metal based joints.

Reaction Bonds

Graphite cements needed to withstand a temperature range of 22°C to 1350°C, prevent pipe disconnections, and prevent tin leaks. When choosing reaction bond agents, it was important to choose a ceramic bond that bonded carbon to carbon and had a similar coefficient of thermal expansion (CTE) to graphite. If the CTE between the bond and pipe was significantly different, they would expand when heated at different rates, creating stresses that could potentially break the cement bond.

The first reaction agent tried was Ceramabond 669 by Aremco (Fig. 41). The cement bonded graphite to graphite and was relatively viscous compared to other graphite bond agents such as Contronics 931 and had a consistency similar to Elmer's glue (e.g., a viscosity on the order of 1,000 Pa*s, similar to honey). The initial thought was that the relatively low viscosity would help fill voids in graphite pipe joints and prevent Sn leaks; however, in practice the resulting bonds often failed when cycled to higher temperatures. As a result, the Ceramabond cement was abandoned in favor of the Cotronics graphite cement.

Fig. 41: Aremco Ceramabond 669

The second reaction bond agent, Cotronics formula 931, was a two part formula consisting of >99% graphite powder and a reaction binder [96]. The powder and binder were mixed together with 26% binder to 74% powder by weight producing a final cement composition that was 99% graphite after curing, which could bond graphite components together up to 3,000°C.

Fig. 42: Cotronics 931 graphite cement. 2 component mixture consisted of binder and powder.

Cotronics 931 had a consistency closer to a paste and a more granular, irregular surface quality. The cure procedure required the bond to set at 100°C for 4 hours and cure at 130°C for 20 hours.

Many graphite joints using 931 were made and initially many leaked water and even Sn(l), even though the bonds between test samples held when cycled from room temperature to 1350C several times. However, the recurring issues with leaks led to a refined bonding procedure to limit the leak frequency and severity. The first improvement was to modify the composition from the recommended 35 part binder to 100 part powder. Using 30 to 33 parts binder instead of 35 was found to produce more

reliable seals, with the ultimate composition decision made based on the consistency of the cement, which was generally a function of lab humidity levels. Less binder ensured the cement was dryer, limiting the amount of excess water that could then boil out and create voids in the cement creating a leak path.

Once the two parts were added to a weigh boat, it was very important to thoroughly mix the two parts, folding the mixture over itself so that it had uniform consistency. Kneading the paste like bread instead of stirring it prevented air bubbles that increased the porosity of the paste.

Fig. 43: Cotronics 931 cement. Left picture is unmixed, right picture is thoroughly mixed.

Applying the graphite cement to the two bonded pieces was done in two stages. First, a thin layer was pressed firmly and uniformly to the entirety of both graphite bond faces using a spatula. This thin layer filled the porosity of the graphite and minimized the surface energy the cement had to overcome during the cure. Following the thin layer, a second thick (>200 mils) cement layer was lavishly applied to both parts that would fill any gaps between the two pieces being bonded.

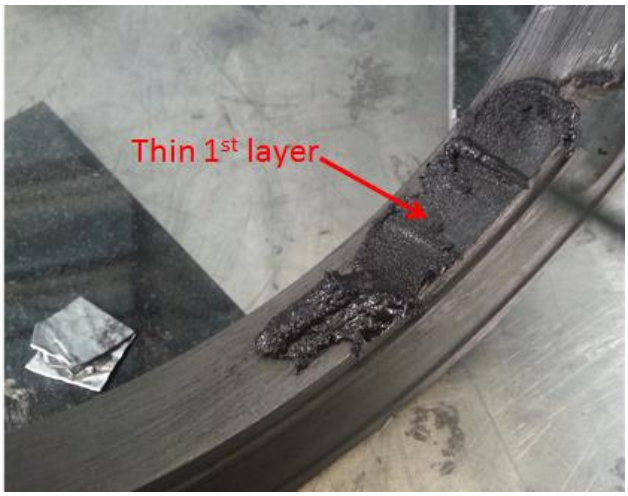

Fig. 44: Graphite cement application

Next, the two parts to be bonded were firmly pressed together, applying force to squeeze excess cement from the joint. If significant quantities of cement did not ooze from the entire joint perimeter, then additional cement was re-applied to the two parts ensuring cement filled all gaps. If the two parts being cemented together had the opportunity to easily shift out of position, then a jig was needed to physically constrain the two parts so that they were bonded in the correct position and the jig could be removed.

Fig. 45: Graphite 2 component cement bond. Excess cement squeezed from joint is smoothed into a beveled surface

For joints with internal Sn passages, after pressing two parts together, cement could ooze into passages and, once cured, it could completely block the passage preventing LM flow. To eliminate these blockages, plugs were made from melting and solidifying Sn(l), which was then inserted into the passage before cement application. This ensured that the passage would remain open since a solid plug of Sn was used to preserve a passage for later Sn flow. This approach worked, because the entire cement curing procedure occurred below the melting point of Sn and thus the Sn plug remained solid during the curing procedure, thereby preventing a blockage from developing. Upon subsequent heating of the system, the Sn plugs simply melted and flowed with the rest of the Sn(l) being pumped. The plugs were formed by melting Sn with an induction furnace and pouring the melt into a mold that modeled the passage to be plugged, often a section of graphite tube that had the same diameter of the passage being protected. The tube was placed upright on a ceramic brick and Sn(l) was poured into the top. This graphite tube

was then quenched in a pot of water to rapidly solidify the Sn. The Sn had a larger volume contraction than the graphite upon solidification, therefore upon cooling, it shrunk slightly and easily fell out of the graphite tube mold. Formed plugs were then cut to the correct size and inserted into the part passage to be cemented.

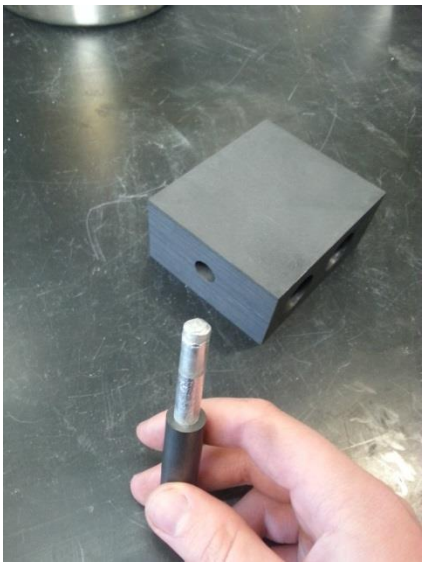

Fig. 46: Sn plug is inserted into tube. Cement is then applied on outer surface and the part to which the tube is being cemented. The tube is then inserted in to be cured.

More complicated passages could be protected with solid Sn by pouring Sn(l) into the part itself. One passage end was plugged loosely with a graphite rod and Sn(l) poured into the passage from the other end. Once solidified, the plug rod was pulled away and Sn that leaked past the unsealed rod to the cement surface was removed via sand paper, a dental pick, or a heat gun.

The final cement curing step was the heating procedure, with Cotronics recommending 4 hours at 100°C and 20 hours at 130°C. The 100°C step slowly boiled water out of the mixture and if the temperature was increased above 100°C before all the water escaped, then water could boil rapidly, forcing steam through the joint, in turn creating voids for tin to leak through. Initially, parts were heated by wrapping them in

heat tape, surrounding the part with insulation, and monitoring the air temperature close to the joint with a thermocouple. The heat tape was cycled on and off based on the surrounding air temperature, but a significant temperature difference existed between the air and the part, thus it was likely the curing joint became significantly hotter than the 100°C air temperature monitored inches away. As a result, many joints heated in this fashion leaked Sn after the full cure procedure.

To address this issue, ovens were built where the heat was delivered to the joint via convection of the air, rather than direct heating of the graphite, as this ensured the graphite bond itself stayed below 100C. The downside to this method was that large graphite parts with a large heat capacity could take longer to cure since the boundary layer now ensured the graphite part was a lower temperature than the atmosphere heating the joint. For large parts and large joints, heat time was doubled (8 hours at 100°C and 40 hours at 130°C) to ensure a complete cure. Given the size of parts needed for the prototype experimental loop, an oven was constructed from a steel box wrapped in insulation with heat tape lining the walls controlled by a thermocouple controller that cycled on and off to maintain the set temperature.

After the part finished curing, it was leak tested by pouring water into the passageway and watching for leaks. Severe leaks revealed water immediately, which typically flowing as a steady stream, while less severe leaks could take 20 minutes or more before water worked its way through the joint and formed drops slowly growing from the cemented joint (Fig. 48).

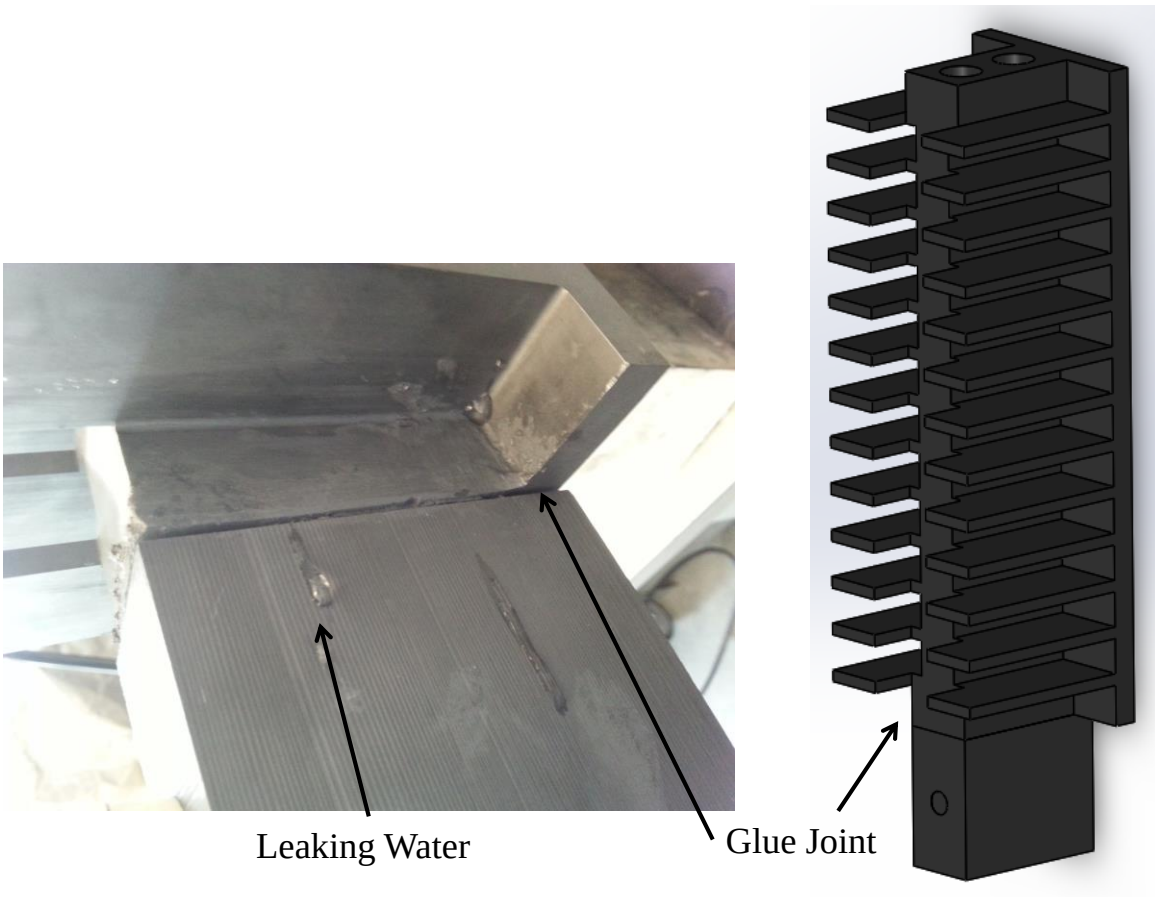

Fig. 47: Cement face joint leaking water. The CAD model for the part shown on the left is shown on the right for reference.

If the leak was not severe, a 5 mm channel was picked in the leaking joint section and new cement was pressed into the channel for re-gluing and re-testing.

Fig. 48: Pick and cement procedure for leaking part.

For large leaks, custom graphite plugs or fillers were sanded from graphite scraps to make approximate patches for the picked groove and reaction bonded into place.

Once the part was proven leak proof against water, it was tested with tin by heating it in an oven to 300°C, and pouring Sn(l) into the passages. Sometimes, cemented joints would leak Sn even if they didn't leak water, even though water wetted graphite while Sn did not. Sn should have required larger leak path cross sections than water to overcome the greater surface tension. However, Sn was more than 7 times as dense as water, so the pressure forcing Sn through a potential leak path was 7 times larger than the pressure from water. Experiments showed that the best way to prevent leaks was by designing joints with minimal bond surface, internal corners to pack cement, and making the joints accessible to picking/repacking once the parts were mated. (Fig. 49 and Fig. 50).

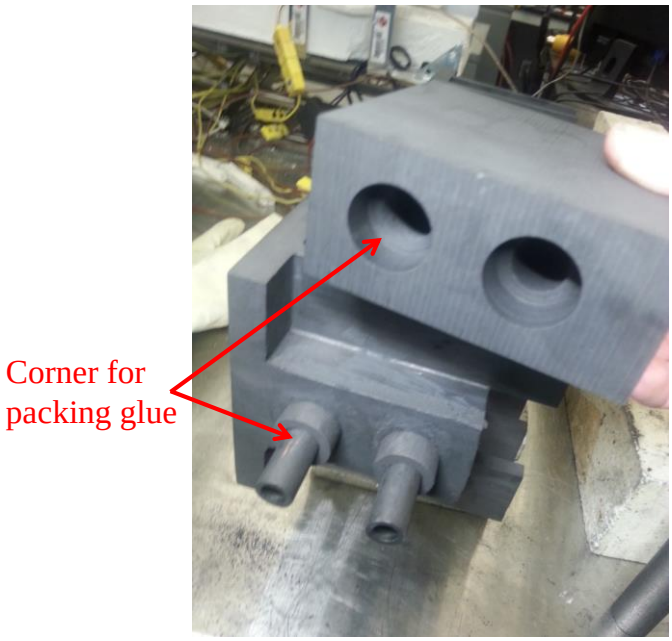

Fig. 49: Example of more reliable geometry for forming a successful cement bond

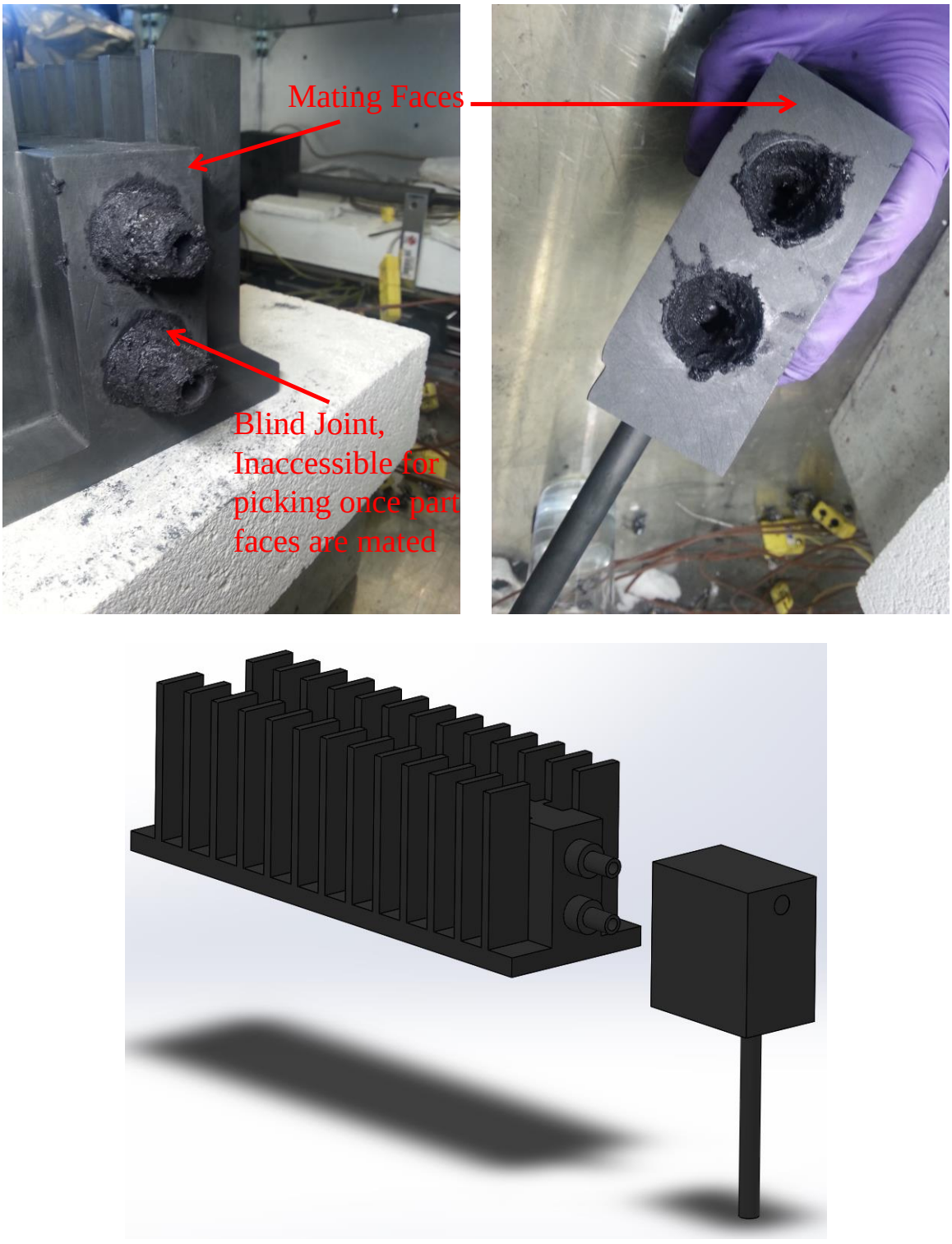

Fig. 50: Example of a cemented joint that is inaccessible to repacking. The CAD representation of the two cemented geometries is shown in the bottom image

Mechanical Sealing

Compression fittings using a graphite ferrule as a mechanical joint were the most advantageous alternative to reaction bonded joints and experiments showed that such joints sealed much more reliably than cemented joints. As shown in Fig. 51, the conical ferrule slipped over the connecting tube and was then inserted into a fitting (either a corner, a union, or a T-joint) that had a female conical hole. A threaded nut then fit over the ferrule and screwed into male threads on the fitting. The nut pressed the ferrule into the conical hole, forcing the graphite ferrule to deform slightly and grip the tube, creating a seal (Fig. 51).

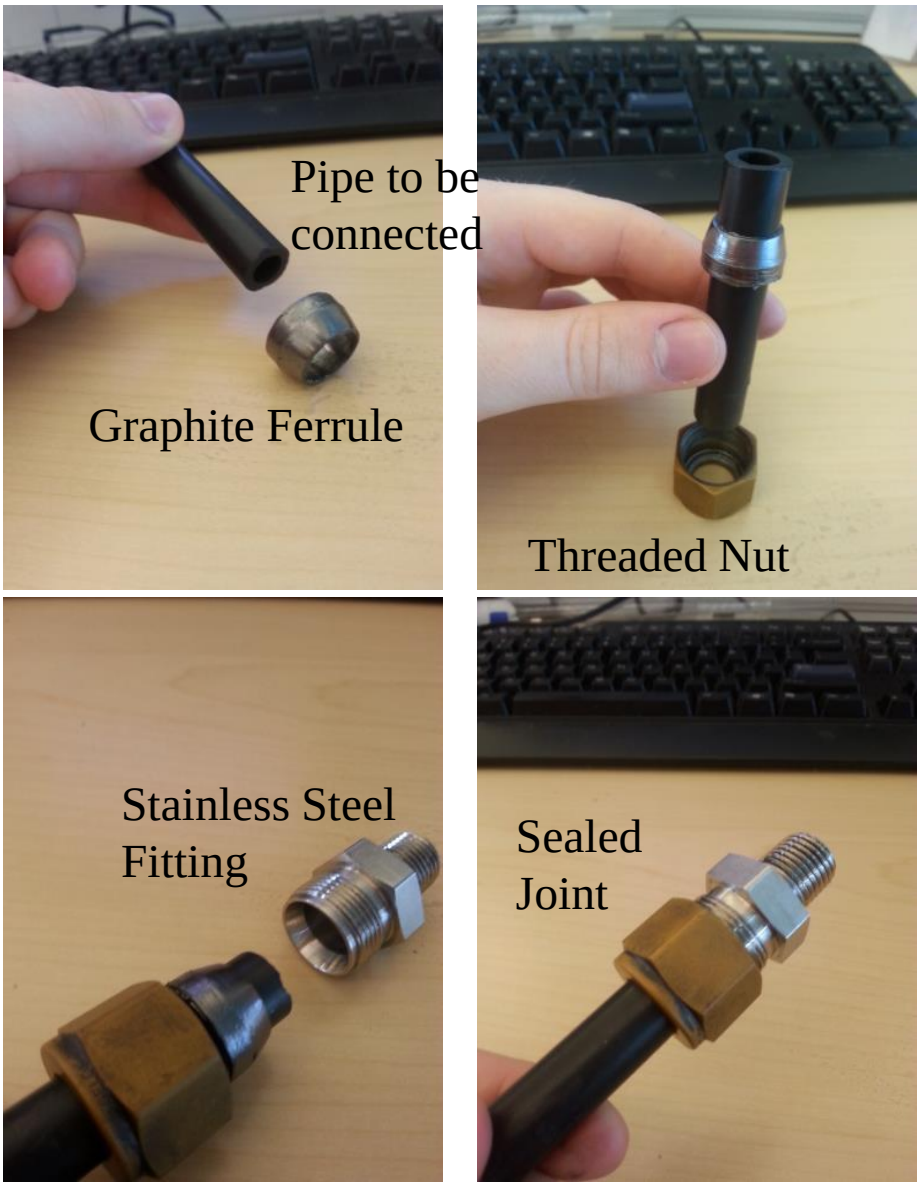

Fig. 51: Graphite ferrule joint

For joints that would operate at 400°C or below, the fittings and nut were typically made from stainless steel and then coated with TiN, so that they were not corroded by Sn(l) at temperatures up to 450°C. For joints that needed to operate above 400C, this stainless steel Swagelok design was replicated using only graphite components to make a mechanical seal at 1,350°C. The same graphite ferrule was used along with the same size graphite tube, 0.5" OD. However, the nut and fittings were made significantly

larger (approximately 1” OD), since the graphite was weaker as the larger diameter limited the shear stresses on the nut when it was torqued onto the threads. Furthermore, the nut and fitting were made larger to accommodate coarser threads with a greater pitch than their stainless steel counterparts (Fig. 52). These all-graphite compression fittings were leak tested with Sn(l) at 400°C and were reliably leak proof after the graphite nut was tightened to a torque of $\geq$ 14 in-lbs.

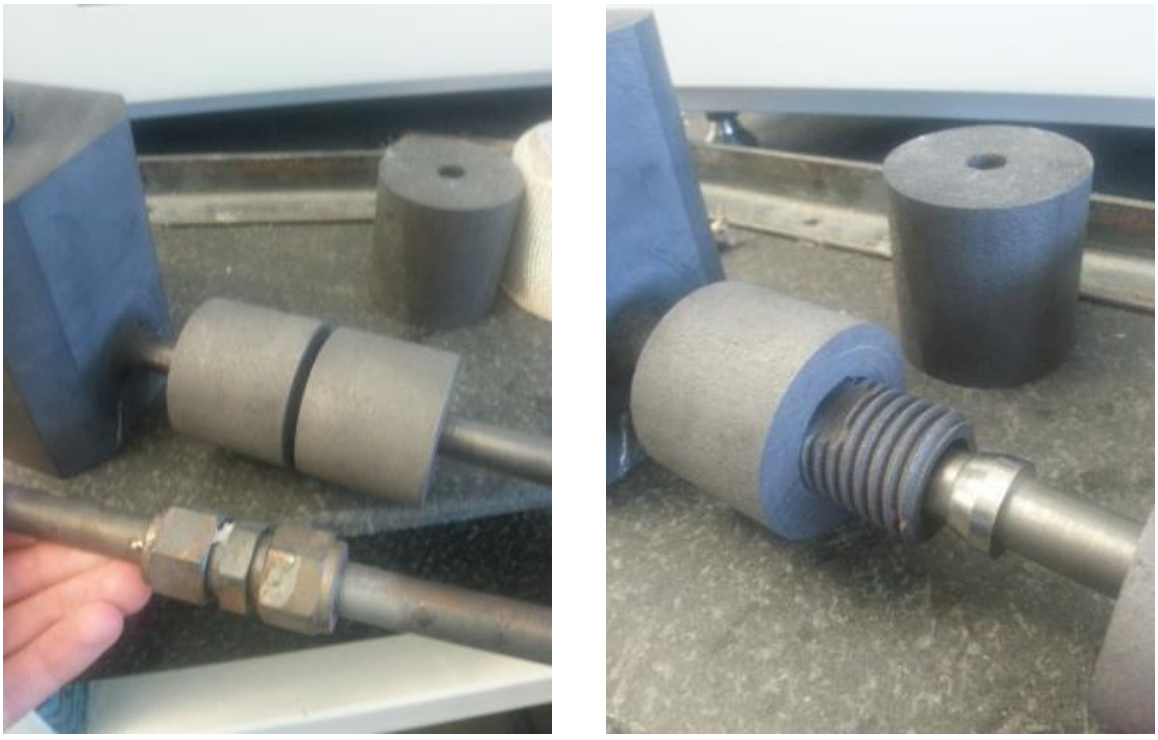

Fig. 52: All graphite compression joint. Picture on left shows completed graphite union joint above completed stainless steel joint for size comparison. The picture on the right shows the coarse threads in a graphite union joint.

LM Valves

Another challenge with LM-CSP was engineering valves that seal and operate at 1,350°C. In a full scale system, valves controlled the flow of Sn to different receiver modules and to the heat exchangers. An experimental attempt was made at using alumina ball valves at 400°C that was partially successful. As a result of lessons learned

from these alumina valves test at 400°C, an all graphite valve was constructed to be tested in a 1,350°C LM pump loop. For the lower temperature valves, a commercial ball valve was purchased from Fujikin. The Fujikin ball valve was made with a stainless steel housing, alumina ball, and polymer seals. The polymer seals were replaced with graphite foil, enabling the valve to operate at 400°C.

Fig. 53: Fujikin ball valve assembly exploded view

Table 27: Part identifier

Number	Manufacturer Description	Replaced?
1	Stainless Steel Coupling	No
2	Stainless Steel Mounting Pad	No
3	Hastelloy-C Stem	No
4	Carbon-Filled Teflon	Yes
5	Stainless Steel Housing	No
6	PTFE Gaskets, cushions ceramic against stainless steel	Yes
7-8	Solid Ceramic Body	No
9-10	Solid Ceramic Ball	No
11	Serial number	
12	Ceramic Socket	
13	Stainless Steel Flange	

Item 6, the PTFE ring designed to cushion the ceramic body inside the stainless steel housing, was replaced with a soft graphite packing ring that had a much higher temperature limitation and compatibility with Sn(l). The packing ring was graphite rope, shown below, cut and formed into the same donut shape as the PTFE ring. Item 4, the carbon filled Teflon, was also replaced with graphite rope packing.

Fig. 54: Graphite rope packing that replaced PTFE and teflon seals

Alumina tubes were reaction bonded onto each side of the ceramic valve (Fig. 55) and connected to the graphite pipe loop using compression fittings. Electronic actuators were used to turn the valve stems and turn the ball valve, opening and closing the valve. Since the valves were at 400°C, these actuators were mechanically connected to the valve via a thermally insulating (2.2 W/m-K) zirconia shaft. Furthermore, Al cooling blocks were bolted underneath the actuators and cooling water pumped through to ensure the actuator electronics stayed cool (Fig. 55).

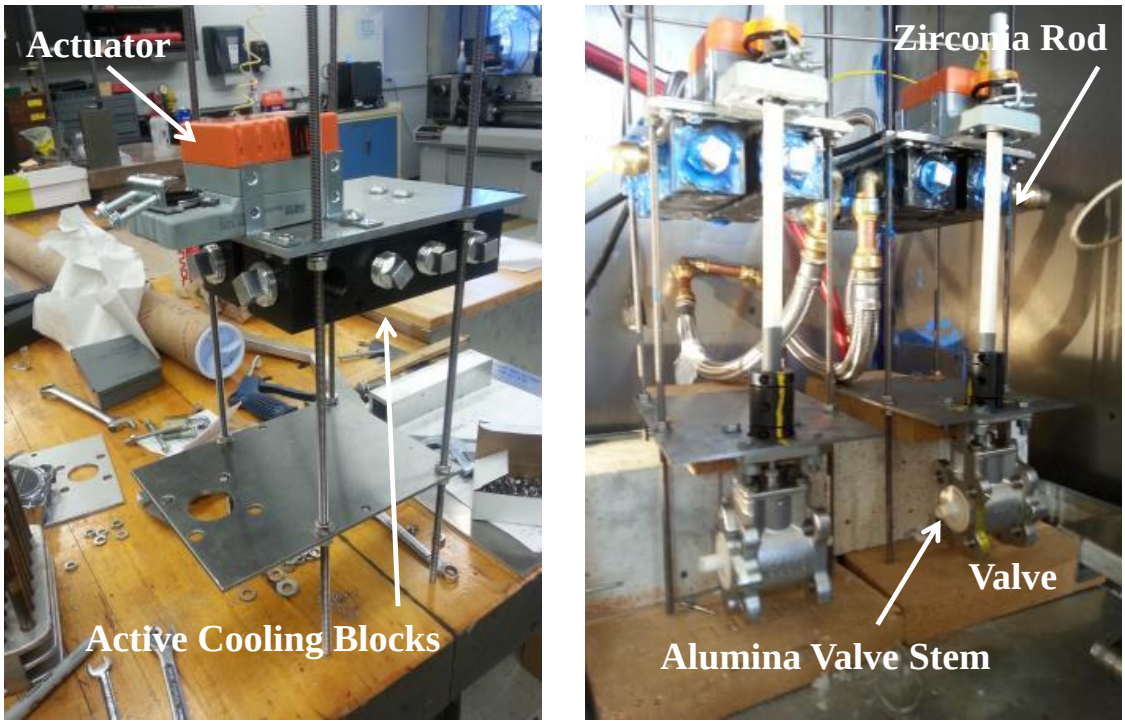

Fig. 55: Valve and actuator holder

In practice, the alumina ball sealed against the ceramic socket by being pressed into the socket due to fluid pressure. The pressure available in the prototype experiments was insufficient to meet this condition and as a result, the valve sealing was unreliable at such low pressures.

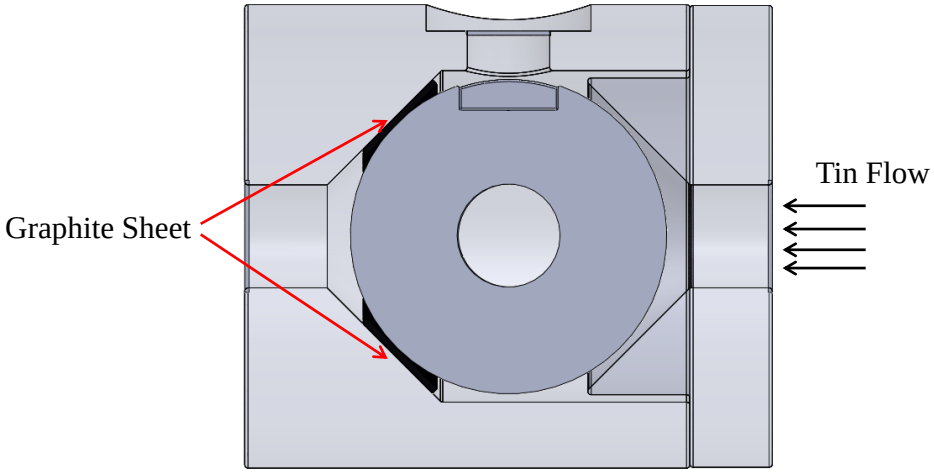

Fig. 56: Top down view of ball valve. Graphite sheet was placed between alumina ball and housing to stem tin flow

The inner ceramic socket was lined with graphite sheet designed to contact the alumina ball and prevent Sn(l) from leaking past it. The valve held back about 75% of the flow when in the off position compared to the flow seen when the valve was opened. However, this reduction in flow occurred at a relatively low pressure; at higher Sn pressures, this graphite sheet seal would almost certainly fail until the pressure was high enough to seat the alumina ball against the socket. These sealing failures motivated a different valve design, made from all graphite to withstand 1,350°C.

With the lessons learned from the alumina ball valve seal, a new, custom, full port plug valve was designed. The plug valve sealed by driving a conical shaft into a conical hole with graphite packing. The new valve was also made entirely from graphite so that it could be tested at 1,350°C. A cross section of the valve is shown here:

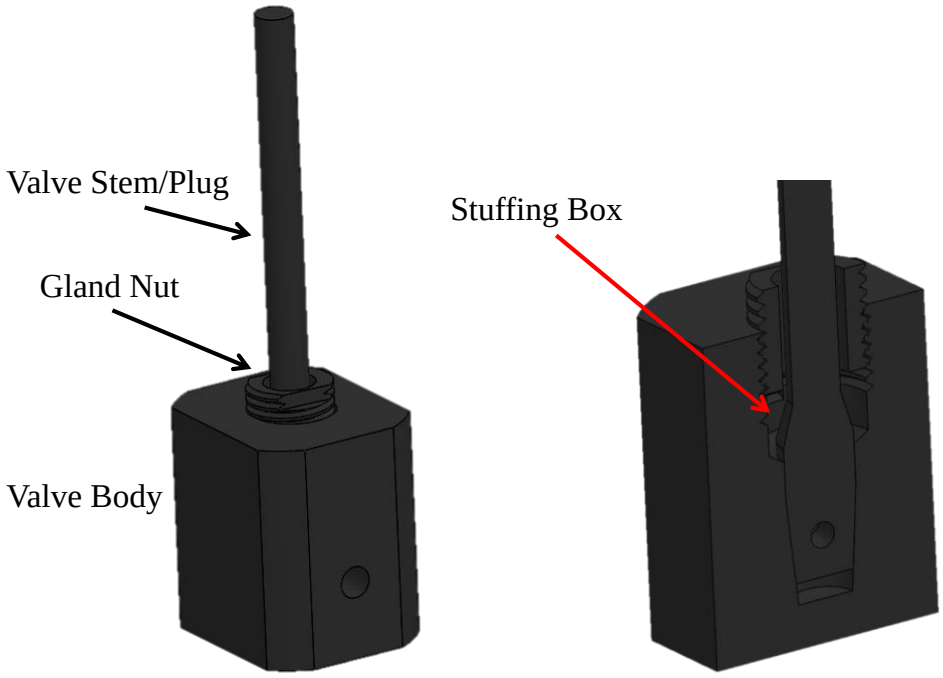

Fig. 57: Graphite plug valve. Image on the right is a cross section view.

The valve consisted of 3 parts: the valve stem, the stem plug, and the valve body. The valve body had a hole that passed through the entire valve, acting as a channel for Sn(l). The valve stem fit in the valve body and had a corresponding through hole that lined up with the valve body passage when the valve was open and blocked flow when the valve stem was turned 90°. The valve stem/plug and valve body were both tapered so that when the stem sat against the body, they formed a tight seal. The gland nut was threaded and screwed into the body forcing graphite rope packing into the cavity between the gland nut, valve stem/plug, and valve body. As the gland nut was screwed tight, this packing was compressed, forcing the tapered plug down into the valve body, forming a seal. This valve was machined and a Sn(l) loop that could be heated to 1,350°C was being designed at publication of this thesis.

Graphite 90° Elbow Minor Losses

In the LM loop designed to test the receiver, the pressure drop through the system was estimated to determine pump pressure requirements. The Reynolds number of the Sn(l) flowing in the loop was extremely low (<10) and therefore major losses through pipe sections were calculated using the laminar flow section of a Moody diagram [67]. However, there was no existing experimental data for minor loss through the specific graphite elbow geometry used, therefore a simple flow experiment was set up to estimate the minor loss through graphite elbows (Fig. 59).

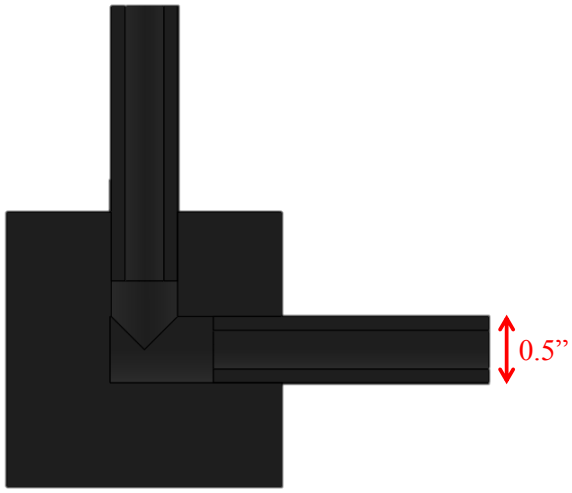

Fig. 58: Graphite elbow cross section

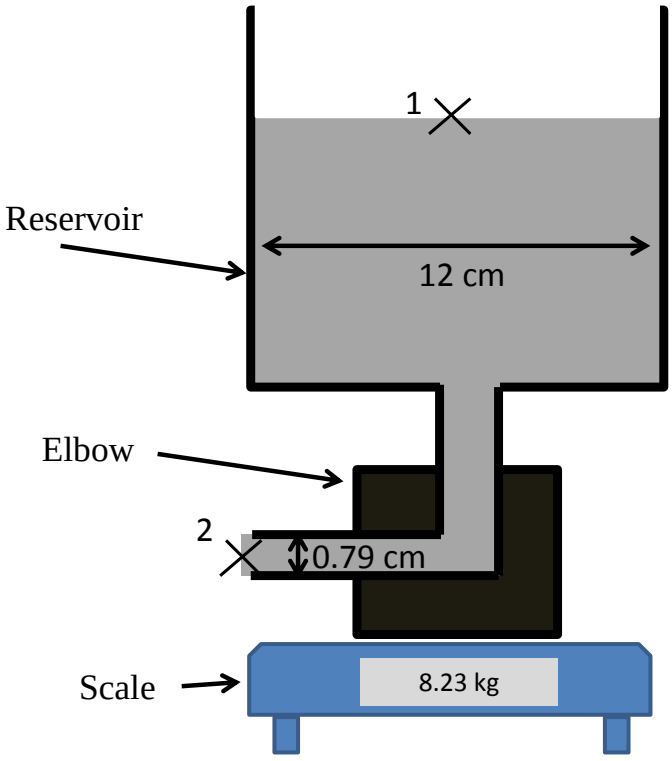

Fig. 59: Elbow minor loss experiment

A graphite elbow was connected to the bottom of a Sn reservoir and the reservoir/elbow assembly was then placed on a scale. The reservoir was initially empty and once Sn(l) was poured into the top of the reservoir it then drained through the elbow

into another receptacle (Fig. 60). The Bernoulli Eq. was used to estimate the transient flow rate as a function of the head loss through the elbow and the corresponding loss coefficient. The two points of a single stream line were the tank free surface (1) and the elbow outlet (2) from Fig. 60. The Bernoulli Eq. for this stream line was as follows:

$$\frac{p_1}{\gamma}+\frac{V_1^2}{2g}+z_1=\frac{p_2}{\gamma}+\frac{V_2^2}{2g}+z_2+h_{\mathrm{min}or} \tag{56}$$

where p was the gauge pressure, V was fluid velocity, z was relative height, and h_{minor} was the minor head loss in the elbow. p_1 and p_2 were both zero because they were free surfaces; z_1 was also zero because it was taken as the reference height. Rearranging Eq. 56 with th0se assumptions in place:

$$h_{\mathrm{min}or}=\frac{V_1^2}{2g}-\frac{V_2^2}{2g}+z_1 \tag{57}$$

The remaining unknowns were the flow velocities at points 1 and 2 as well as the relative height of the fluid in the tank. These values were obtained from the mass vs. time data obtained by pouring Sn(l) into the reservoir.

Fig. 60: Sn elbow minor loss test pour procedure

A mass measurement was sampled every second as the reservoir drained, producing a "drain curve". The scale was continuously running and 7 Sn(l) pours were performed, producing 7 drain curves with the raw data shown below:

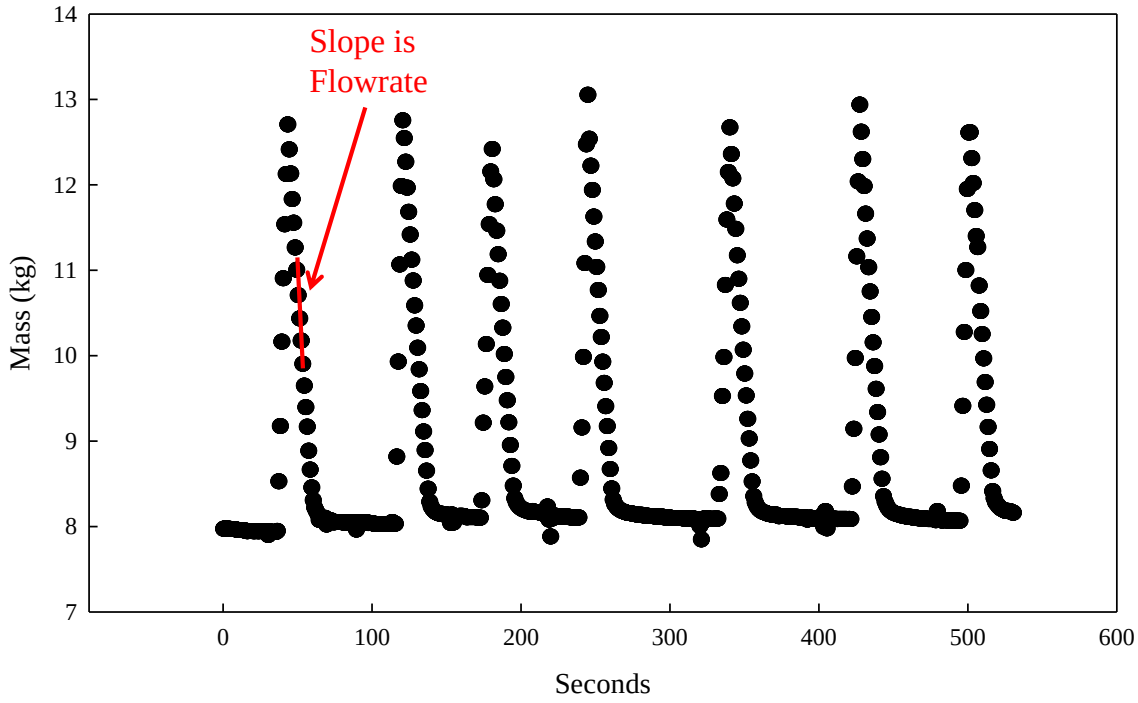

Fig. 61: Elbow drain curve data

Fig. 61 shows 7 distinct peaks indicating 7 separate drain events and an intermediate time period where the flow rate was approximately constant. The relevant data is for negative slopes of measured mass vs. time after the Sn(l) had been poured into the reservoir and the elbow drained with two free surfaces. From each drain curve, the instantaneous slope was calculated to obtain the mass flow rate vs. time and then converted to volumetric flow rate by dividing by the Sn density. The reservoir diameter and pipe outlet diameter were known, so the flow speed was obtained by dividing the volumetric flow rate by the cross sectional area. The height was obtained by subtracting the empty weight of the reservoir (8.0 kg) from the measured weight and using the Sn density and reservoir dimensions to calculate height. The velocities and Sn height were then used to calculate the loss coefficient K_L at each measured time during the drain curve:

$$K_L = \frac{h_{\min or} \times 2g}{V_2^2} \tag{58}$$

A different K_L value was calculated for each time step during a drain, making it difficult to pick a consistent loss coefficient for a drain curve; however, in the middle part of each drain curve, the *k* value varied very little (±7%) allowing a consistent loss coefficient measurement. The reason for larger discrepancies in *k* at the start of each drain curve was due to the Sn being poured into the reservoir, which invalidated the Bernoulli stream line analysis. At the end of each drain curve, Sn slowly dribbled out of the elbow and did not fill the entire tube cross section, also invalidating the Bernoulli stream line analysis. The *k* value for each drain and the total average was tabulated:

Table 28: K values for drain trials

Drain Trial	K
1	2.9
2	3.1
3	2.6
4	2.8
5	2.7
6	2.5
7	2.5
Average	2.7
Std. Deviation	0.2

For the graphite elbow geometry tested, the minor loss coefficient was 2.7. This was significantly higher but not unreasonable compared to loss coefficients for threaded plumbing pipe elbows: 1.5 [67]. Furthermore, the Sn drained from a reservoir into a smooth tube that was positioned between the reservoir and elbow. This was considered a 'reentrant loss', introducing another minor loss coefficient for the system, which was not isolated in the experiment. The reference minor loss obtained for an experiment with a reservoir draining directly into a catch pan was 0.8 [67]. Subtracting 0.8 from the

experimental minor loss coefficient for the reservoir elbow system gave 1.9, which was much closer to the established 1.5 for threaded plumbing elbows. The abrupt change in diameter between the cemented nub and corner block likely led to the greater loss coefficient which could be decreased by counter-boring the cemented nubs so that there is a smooth transition in diameter. However, this is not necessary for the LM loop experiment because the flowrates are low and parasitic pressure losses minor.

Knowing the minor loss coefficient, the total head loss for the receiver experimental loop was estimated. There were 14 elbows in series and 3.3 m of graphite pipe with a 0.0127 m diameter. The flow rate for the loop at a receiver outlet temperature of 1,350°C was 0.026 kg/s and with 0.0127 m diameter pipes and Sn density 6,800 kg/m^3, this gave a flow speed of 0.03 m/s. Major head loss was calculated as:

$$h_{L,major} = f \frac{l}{D} \times \frac{V^2}{2g} \tag{59}$$

where l was pipe length, D was pipe diameter, V was Sn velocity, and g was the gravitational constant. The friction factor f was calculated for laminar flow as:

$$f = \frac{64}{\mathrm{Re}} \tag{60}$$

The major head loss was 0.005 m, which was negligibly small, while the minor head loss was calculated according to Eq. 58 and multiplied by 14 elbows and was 0.0017 m.

The low head loss was primarily a result of the rather low linear velocity of Sn through the loop (3 cm/s), which was needed for the LM to be cycled through such a large temperature difference, 1350°C to 400°C. Low flow rates were required to allow the Sn enough residence time in the receiver and heat sinks to heat and cool sufficiently. For most heat transfer fluids, these slow, laminar flows would significantly inhibit heat

transfer and require long pipe networks for greater surface area; however, because Sn(l) had such high thermal conductivity, 30 W/m-K, high heat transfer coefficients were obtained even with laminar flows.

CHAPTER 10: CONCLUSION

For continued economic growth, the world requires electricity generation that is low-cost and occurs without greenhouse gas emissions. Solar energy is an obvious choice because sunlight is free, plentiful, and clean. However, solar energy is dilute, requiring a costly infrastructure to collect and convert it to electricity. Furthermore, energy storage is required to compensate for the intermittency of solar supply and the varying demand.

Current LS-CSP TES can deliver clean dispatchable electricity with an LCOE of 13-15 ¢/kWh, 2.5 times that of fossil fuel generation[10]. Lower costs are necessary to see significant market penetration by CSP plants. One way to lower costs is by increasing the efficiency of CSP and converting more of the captured sunlight to electricity. Higher efficiency requires higher temperatures, and current liquid nitrate salts are limited to 600°C [43]. Using LMs instead enables higher operating temperatures that can be used to heat a working fluid in a combined power cycle with 60% conversion efficiency as compared to current efficiencies of 40%.

To estimate the costs, a full scale plant was designed to transfer sunlight to LM at 1350°C. Two different LMs were used in this nominal plant design: Al-Si(l) in the TES tanks because it was inexpensive and Sn(l) in the receiver because Al corroded graphite. All subsystems using LM were contained in an inert atmosphere to prevent oxidation. The receiver, heat exchangers, storage tanks, ceramic piping, and nitrogen containment were all modeled using basic heat transfer and thermodynamic relations. Systems costs were estimated based on the design of the different components and material cost factors. Construction costs were taken from published estimates for a LS-CSP plant with the same thermal input and scaled to the LM-CSP geometry.

The complexity of the CSP plant was increased significantly, due to the use of two different LMs, a phase change storage material, an internal receiver geometry, and inert containment. Furthermore, ceramic materials were required for a LM-CSP plant, instead of traditional stainless and carbon steels. Greater complexity and material costs increased the overall component costs. However, when normalized to electricity produced, the LM-CSP plant modeled here was 30% less expensive at 9.3 ¢/kWh, compared to 13.4 ¢/kWh for the published LS-CSP plant.

There were three primary reasons for cost savings: higher efficiency, higher energy density TES, and lower pumping parasitic losses. Since the sunlight was collected and stored at 1350°C instead of 565°C, a heat engine with 60% conversion efficiency could be used instead of 40%. This led to a 50% increase in electricity generation for the same collector field and a corresponding reduction in all normalized costs. The large temperature difference for the LM and enormous energy density of phase change Al-Si meant the TES system components decreased in size, leading to further cost reductions. Finally, LMs had thermal conductivities 1 to 2 orders of magnitude higher than LS, so a high rate of heat transfer was achieved with low flows, decreasing the parasitic pump losses for the power plant.

Additional thermodynamic analysis are necessary for a closed-loop He Brayton cycle that rejected heat to a SCO2 bottoming cycle to better estimate cycle efficiency, especially because the cost savings realized by switching to LM were a strong function of power cycle efficiency. In this model, the 60% conversion efficiency was assigned nominally since current natural gas combined cycles operating at ~ 1400°C had 60%

conversion efficiency; but, a detailed thermodynamic analysis for the proposed power cycle was needed to determine a more accurate cycle efficiency.

There still remained significant technical challenges before the LM-CSP plant modeled in this report could be built. Many of these challenges had or were currently being addressed by constructing a graphite based LM circulation loop. Graphite was established as an inert, refractory, and conductive containment material for Sn(l). With regards to a graphite pipe network, both chemical and mechanical seals have been successfully demonstrated between graphite pipes and plenums operating at 400°C. Furthermore, the pressure drop across these reaction-bonded joint geometries was characterized, and was effectively negligible due to the low flow rate of the LM. Finally, an all graphite valve was successfully built that could seal against Sn(l) at 400°C and was soon t0 be tested in a pumped loop at 1,350°C.

The two most immediate unsolved technical challenges were demonstrating an internal optical cavity receiver geometry that could convert sunlight to thermal energy with efficiency in excess of 80%, and operating a pump and valve loop at 1350°C. Significant progress toward these experimental setups was made and tests were ongoing. Further research was required to fully design LM SiC shell and tube heat exchangers, LDHXs, a SCO2 Brayton cycle, a closed loop He Brayton cycle, a secondary concentrator, and Al-Si storage tanks.

The remaining technical challenges to successfully design and construct LM-CSP plant were numerous and substantial. However, the challenges posed by greenhouse gas emissions and subsequent climate change necessitated drastically improved solutions. The results of the research presented herein demonstrated there was significant potential

for LM-CSP to compete with natural gas and the technical progress that was made thus far on the systems designed was encouraging.

REFERENCES

1. DOE, *Sunshot Vision Study.*, Washington, DC, 2012.
2. Sioshansi, R. and P. Denholm, *The value of concentrating solar power and thermal energy storage.* Sustainable Energy, IEEE Transactions on, 2010. **1**(3): p. 173-183.
3. Denholm, P., et al., *The value of energy storage for grid applications.* Contract, 2013. **303**: p. 275-3000.
4. Luo, X., et al., *Overview of current development in electrical energy storage technologies and the application potential in power system operation.* Applied Energy, 2015. **137**: p. 511-536.
5. Yang, C.-J., *Pumped hydroelectric storage.* Durham, North Carolina, USA, 2012.
6. Dunn, B., H. Kamath, and J.-M. Tarascon, *Electrical energy storage for the grid: a battery of choices.* Science, 2011. **334**(6058): p. 928-935.
7. Rastler, D., *Electricity energy storage technology options: a white paper primer on applications, costs and benefits*. 2010: Electric Power Research Institute.
8. Chen, H., et al., *Progress in electrical energy storage system: A critical review.* Progress in Natural Science, 2009. **19**(3): p. 291-312.
9. Albright, G., J. Edie, and S. Al-Hallaj, *A comparison of lead acid to lithium-ion in stationary storage applications.* Alternative Energy eMagazine Industry [online serial](April 12), 2012.
10. Kolb, G.J., et al., *Power tower technology roadmap and cost reduction plan.* SAND2011-2419, Sandia National Laboratories, Albuquerque, NM, 2011.
11. Medrano, M., et al., *State of the art on high-temperature thermal energy storage for power generation. Part 2—Case studies.* Renewable and Sustainable Energy Reviews, 2010. **14**(1): p. 56-72.
12. Martin, S. *Fired up about Efficiency*. 2013.
13. Kehlhofer, R., et al., *Combined-cycle gas & steam turbine power plants*. 2009: Pennwell Books.
14. Barlev, D., R. Vidu, and P. Stroeve, *Innovation in concentrated solar power.* Solar Energy Materials and Solar Cells, 2011. **95**(10): p. 2703-2725.
15. Denholm, P. and M. Mehos, *Enabling greater penetration of solar power via the use of CSP with thermal energy storage.* Solar Energy: Application, Economics, and Public Perception, 2014: p. 99.
16. Romero, M., R. Buck, and J.E. Pacheco, *An update on solar central receiver systems, projects, and technologies.* Journal of solar energy engineering, 2002. **124**(2): p. 98-108.
17. Lata, J.s.M., M. RodrÃguez, and M.n.Ã. lvarez de Lara, *High flux central receivers of molten salts for the new generation of commercial stand-alone solar power plants.* Journal of Solar Energy Engineering, 2008. **130**(2): p. 021002.
18. Ho, C.K., et al. *Reduction of radiative heat losses for solar thermal receivers*. in *SPIE Solar Energy+ Technology*. 2014. International Society for Optics and Photonics.
19. Gallego, B., *The History of American CSP, A Timeline.* CSP Today USA 2012, 2012.
20. Lab, S. *Solar Two Demonstrates Clean Power for the Future*. Sun Lab Snapshot, 2000.

21. Chhabara, R., *Towers versus troughs?* CSP Today, 2009.
22. Martínez-Duart, J.M. and J. Hernández-Moro, *Commentary: Photovoltaics firmly moving to the terawatt scale.* Journal of Nanophotonics, 2013. **7**(1): p. 078599-078599.
23. Hernández-Moro, J. and J. Martínez-Duart, *Analytical model for solar PV and CSP electricity costs: Present LCOE values and their future evolution.* Renewable and Sustainable Energy Reviews, 2013. **20**: p. 119-132.
24. Bazilian, M., et al., *Re-considering the economics of photovoltaic power.* Renewable Energy, 2013. **53**: p. 329-338.
25. Skumanich, A., *CSP at a crossroads: The first solar electric power plants are still proving their worth after three decades, so why aren't we seeing more CSP reach the development stage?* Renewable energy focus, 2011. **12**(1): p. 52-55.
26. NREL, *Ivanpah Solar Electric Generating System*. Concentrating Solar Power Projects, 2014.
27. Bolinger, M., *Utility-Scale Solar 2012: An Empirical Analysis of Project Cost, Performance, and Pricing Trends in the United States.* 2014.
28. Turchi, C., et al. *Current and future costs for parabolic trough and power tower systems in the US market*. in *Proceedings of the 16th SolarPACES Conference, Perpignan, France*. 2010.
29. NREL, *Concentrating Solar Power Projects.* 2015.
30. Baharoon, D.A., et al., *Historical development of concentrating solar power technologies to generate clean electricity efficiently–A review.* Renewable and Sustainable Energy Reviews, 2015. **41**: p. 996-1027.
31. Brooks, F.J., *GE gas turbine performance characteristics.* GE Power Systems, Schenectady, NY, 2000.
32. Kearney, D., et al., *Engineering aspects of a molten salt heat transfer fluid in a trough solar field.* Energy, 2004. **29**(5): p. 861-870.
33. Fernández, A.G., M.I. Lasanta, and F.J. Pérez, *Molten Salt Corrosion of Stainless Steels and Low-Cr Steel in CSP Plants.* Oxidation of Metals, 2012. **78**(5-6): p. 329-348.
34. Kruizenga, A. and D. Gill, *Corrosion of Iron Stainless Steels in Molten Nitrate Salt.* Energy Procedia, 2014. **49**(0): p. 878-887.
35. Goods, S. and R.W. Bradshaw, *Corrosion of stainless steels and carbon steel by molten mixtures of commercial nitrate salts.* Journal of materials engineering and performance, 2004. **13**(1): p. 78-87.
36. Li, C.-J., et al., *Survey of Properties of Key Single and Mixture Halide Salts for Potential Application as High Temperature Heat Transfer Fluids for Concentrated Solar Thermal Power Systems.* AIMS Energy, 2014. **2**(2): p. 133-157.
37. Olson, L.C., et al., *Materials corrosion in molten LiF–NaF–KF salt.* Journal of Fluorine Chemistry, 2009. **130**(1): p. 67-73.
38. Williams, D., *Assessment of candidate molten salt coolants for the NGNP/NHI Heat-Transfer Loop.* ORNL/TM-2006/69, Oak Ridge National Laboratory, Oak Ridge, Tennessee, 2006.
39. Pacio, J. and T. Wetzel, *Assessment of liquid metal technology status and research paths for their use as efficient heat transfer fluids in solar central receiver systems.* Solar Energy, 2013. **93**(0): p. 11-22.

40. Ho, C., et al., *Technology Advancements for Next Generation Falling Particle Receivers.* Energy Procedia, 2014. **49**: p. 398-407.
41. Lai, G.Y., *High temperature corrosion of engineering alloys.* 1990.
42. DOE, *Electric Power Annual 2009.* Energy Information Administration, 2009.
43. Cable, R., et al., *Overview on use of a Molten Salt HTF in a Trough Solar Field.*
44. Ghoiem, S.S.a.N., *Summary of Thermo-Physical Properties of Sn and Compounds of Sn-H, Sn-O, Sn-C, Sn-Li, and Sn-Si.* APEX Study, 2000.
45. Gale, W.F. and T.C. Totemeier, *Smithells metals reference book*. 2003: Butterworth-Heinemann.
46. Zhao, Y., et al., *Interaction of liquid tin and zinc with AISI 304 stainless steel after passivation in air and nitric acid.* Materials Characterization, 2013. **77**: p. 1-9.
47. Saint-Gobain, *Hexoloy SA Silicon Carbide Wear Resistant Parts for the Mining Industry.* 2015.
48. U.S.E.I., *Updated Capital Cost Estimates for utility Scale Electricity Generating Plants.* Independent Statistics and Analysis, 2013.
49. Wagner, M.J., S.A. Klein, and D.T. Reindl. *Simulation of Utility-Scale Central Receiver System Power Plants*. in *ASME 2009 3rd International Conference on Energy Sustainability collocated with the Heat Transfer and InterPACK09 Conferences*. 2009. American Society of Mechanical Engineers.
50. *MetalPrices.com*. 2015 Available from: http://www.metalprices.com/p/metal_index.
51. Makhlouf, M. and H. Guthy, *The aluminum–silicon eutectic reaction: mechanisms and crystallography.* Journal of light metals, 2001. **1**(4): p. 199-218.
52. DeAngelis, F., *Analysis and Design of a High-Temperature Liquid Metal Solar Thermal Receiver.* Georgia Institute of Technology Masters Thesis, 2015.
53. Kingery, W., *Thermal Conductivity: XII, Temperature Dependence of Conductivity for Single-Phase Ceramics.* Journal of the American Ceramic Society, 1955. **38**(7): p. 251-255.
54. Wotari, K., *High Thermal Conductivity Non-Oxide Ceramics.* Journal of the Ceramic Society of Japan, 2001. **109**(1265): p. S7-S16.
55. U.S.E.I. *Electric Power Monthly.* Independent Statistics & Analysis, 2015.
56. Kreiss, K., et al., *Risks of beryllium disease related to work processes at a metal, alloy, and oxide production plant.* Occupational and environmental medicine, 1997. **54**(8): p. 605-612.
57. Henry, A. and R. Prasher, *The Prospect of High Temperature Solid State Energy Conversion to Reduce the Cost of Concentrated Solar Power.* Energy Environ. Sci., 2014.
58. Martin, S., *Fired up about Efficiency*. 2013, Siemens AG.
59. Ortega, J.I., J.I. Burgaleta, and F.M. Téllez, *Central Receiver System Solar Power Plant Using Molten Salt as Heat Transfer Fluid.* Journal of Solar Energy Engineering, 2008. **130**(2): p. 024501-024501.
60. Gilman, P. and A. Dobos, *System Advisor Model, SAM 2011.12. 2: General Description*. 2012, National Renewable Energy Laboratory (NREL), Golden, CO.
61. MTI Corporation *Mullite Tube*. Furnace Accessories 2014 Available from: http://www.mtixtl.com/mullitetube4od100mmx40l1000mm.aspx.

62. Grainger. *Stainless Steel Tubing*. 2014 Available from: http://www.grainger.com/category/stainless-steel-tubing/pipe-and-tubing/plumbing/ecatalog/N-aae#nav=%2Fcategory%2Fstainless-steel-tubing%2Fpipe-and-tubing%2Fplumbing%2Fecatalog%2FN-aaeZ1z0nx0nZ1z0nym3%3F_%3D1395355488485.
63. Winston, R., J.C. Miñano, and P.G. Benitez, *Nonimaging optics*. 2005: Academic Press.
64. Kolb, G.J., et al. *Heliostat cost reduction*. in *ASME 2007 Energy Sustainability Conference*. 2007. American Society of Mechanical Engineers.
65. Zircar Ceramics, *Alumina Mat*. Available from: http://www.zircarceramics.com/pages/flexible/specs/almat.htm.
66. Glatzmaier, G., *Developing a Cost Model and Methodology to Estimate Capital Costs for Thermal Energy Storage*. 2011, National Renewable Energy Laboratory (NREL), Golden, CO.
67. Okiishi, M.Y., B. Munson, and D. Young, *Fundamentals of Fluid Mechanics.* John Wiley & Sons, Inc, 2006.
68. Warburton, C., *Surface roughness of graphite and its effect on friction factor.* Proceedings of the Institution of Mechanical Engineers, 1974. **188**(1): p. 457-460.
69. Ghiaasiaan, S.M., *Convective heat and mass transfer*. 2011: Cambridge University Press.
70. Sobolev, V., *Database of thermophysical properties of liquid metal coolants for GEN-IV.* SCK-CEN, Scientific Report BLG-1069, 2010.
71. Elkin, B., et al., *Molten Oxide Glass Materials for Thermal Energy Storage.* Energy Procedia, 2014. **49**(0): p. 772-779.
72. Tuček, K., J. Carlsson, and H. Wider, *Comparison of sodium and lead-cooled fast reactors regarding reactor physics aspects, severe safety and economical issues.* Nuclear Engineering and Design, 2006. **236**(14): p. 1589-1598.
73. Murray, J. and A. McAlister, *The Al-Si (aluminum-silicon) system.* Bulletin of Alloy Phase Diagrams, 1984. **5**(1): p. 74-84.
74. McGowan, K., *Comparative Strengths of Refractories versus Corundum in Furnace Linings.* Westmoreland Advanced Materials, 2008.
75. M., H., *Refractory materials for Aleris reverb furnaces: test results and evaluation.* Corus Research, Development & Technology, 2008.
76. Depot, H., *R-19 Kraft FAced Insulation Roll*. 2015.
77. Bergman, T.L., F.P. Incropera, and A.S. Lavine, *Fundamentals of heat and mass transfer*. 2011: John Wiley & Sons.
78. Hewitt, G.F., G.L. Shires, and T.R. Bott, *Process heat transfer*. Vol. 113. 1994: CRC press Boca Raton, FL.
79. Tournier, J.-M.P. and M.S. El-Genk, *Properties of noble gases and binary mixtures for closed Brayton Cycle applications.* Energy Conversion and Management, 2008. **49**(3): p. 469-492.
80. Bruckner, A. and A. Shariatmadar. *Heat transfer and flow studies of the liquid droplet heat exchanger*. in *Space Nuclear Power Systems 1985*. 1987.
81. Brewster, M., *High-Temperature Solids-Gas Interactions*, in *Direct-Contact Heat Transfer*. 1988, Springer. p. 167-195.

82. Flemmer, R. and C. Banks, *On the drag coefficient of a sphere*. Powder Technology, 1986. **48**(3): p. 217-221.
83. Vitos, L., et al., *The surface energy of metals.* Surface Science, 1998. **411**(1): p. 186-202.
84. Dostal, V., et al. *A supercritical CO2 gas turbine power cycle for next-generation nuclear reactors*. in *10th International Conference on Nuclear Engineering*. 2002. American Society of Mechanical Engineers.
85. El-Genk, M.S. and J.-M. Tournier, *Noble-gas binary mixtures for closed-Brayton-cycle space reactor power systems.* Journal of propulsion and power, 2007. **23**(4): p. 863-873.
86. Stewart, W.L., A.J. Glassman, and R.P. Krebs, *The Brayton cycle for space power*. 1963, SAE Technical Paper.
87. Shaltens, R.K. and L.S. Mason. *800 Hours of Operational Experience from a 2 kW~ e Solar Dynamic System*. in *AIP CONFERENCE PROCEEDINGS*. 1999. IOP INSTITUTE OF PHYSICS PUBLISHING LTD.
88. Wright, S.A., et al., *Operation and analysis of a supercritical CO2 brayton cycle*. Sandia Report, No. SAND2010-0171, 2010.
89. Weitzel, P.S., J. Tanzosh, and B. Boring, *Advanced Ultra-Supercritical Power Plant (700 to 760C) Design for Indian Coal*. 2012.
90. Dostal, V., P. Hejzlar, and M.J. Driscoll, *The supercritical carbon dioxide power cycle: comparison to other advanced power cycles.* Nuclear technology, 2006. **154**(3): p. 283-301.
91. Litwin, R.Z., *Receiver system: lessons learned from solar two.* Sandia National Laboratories, Report No. SAND2002-0084, 2002.
92. Pacio, J., et al., *Liquid Metals as Efficient Coolants for High-intensity Point-focus Receivers: Implications to the Design and Performance of Next-generation CSP Systems.* Energy Procedia, 2014. **49**: p. 647-655.
93. *Glass Lined Tubing.* SGE Analytical Science.
94. Navinšek, B., P. Panjan, and I. Milošev, *Industrial applications of CrN (PVD) coatings, deposited at high and low temperatures.* Surface and Coatings Technology, 1997. **97**(1): p. 182-191.
95. Kurata, Y. and M. Futakawa, *Corrosion of CrN-coated steels in liquid Pb-Bi.* Materials transactions, 2007. **48**(3): p. 519-525.
96. Cotronics, *Resbond 931 Graphite Adhesive.* 2015.